UNIVERSITY OF CALIFORNIA

Santa Barbara

Sub-Hz Fundamental Linewidth Silicon Nitride Integrated Brillouin Lasers and Their Applications

A dissertation submitted in partial satisfaction of the

requirements for the degree Doctor of Philosophy

in Electrical and Computer Engineering

by

Sarat Chandra Gundavarapu

Committee in charge:

Professor Daniel J. Blumenthal, Chair

Professor John E. Bowers

Professor Larry A. Coldren

Professor Nadir Dagli

December 2018

The dissertation of Sarat Chandra Gundavarapu is approved.

_____

Professor John E. Bowers

_____

Professor Larry A. Coldren

_____

Professor Nadir Dagli

_____

Professor Daniel Blumenthal, Committee Chair

December 2018

Sub-Hz Fundamental Linewidth Silicon Nitride Integrated Brillouin Lasers and Their Applications

by

Sarat Chandra Gundavarapu

ACKNOWLEDGEMENTS

ఎందరో మహానుభావులు, అందరికీ వందనములు

While this dissertation happens to bear my name, I sincerely believe that the journey to the point of writing this up is a result of the invaluable contributions, both professional and personal, made by a lot of people. This section is just an attempt to acknowledge their contributions.

Firstly, I thank Professor Blumenthal for accepting me in to his group, standing by me through these years, guiding and motivating me to work on cutting-edge research. His passion for science, smart and competitive research methodology, and persistence for high quality work have shaped my outlook, problem-solving and management capabilities that I believe are crucial not just as a researcher but as an individual too. I thank him for his belief in me, his continuous support through my years at UCSB with his technical advice and state of the art research lab equipment, and helping me gain exposure to the broader research community through multiple conference travels and numerous collaborations with different research groups. Along with Dan, I would like to thank Professor John Bowers for his support, technical advice, and encouragement throughout my time at UCSB, especially during the years of iWOG project. His scientific intuition and excellent management skills have been inspirational to me. I would also like to thank Professor Dagli and Professor Coldren for their courses that have helped me gain an understanding of electromagnetics and lasers and also for their constant support.

Collaborations with multiple research groups have played a central role in shaping my research at UCSB. I thank Ryan Behunin for his invaluable contribution to this thesis work and numerous, extremely helpful discussions on Brillouin lasers I had with him over the past years. His patient advice and excellent understanding of Brillouin physics along with very helpful insights from Professor Peter T. Rakich and Nils Otterstrom at Yale have played a pivotal role in my graduate research and this dissertation. I must thank Matthew Puckett, Jianfeng Wu, Karl Nelson, Jim Nohava, Mary Salit, and others at Honeywell for their help and advice through insightful weekly meetings.

While at UCSB, I was fortunate enough to meet and work with a pool of brilliant researchers and good people. I thank Renan Moreira for his patient and helpful advice with whom I shared the office when joined the group and I am sharing the office when I am about to leave the group. Discussions and working with Michael Belt were fun and extremely fruitful through the iWOG and Brillouin laser projects. His depth of knowledge, truly professional, and friendly nature are a perfect combination to make an inspiringly researcher and an excellent manager. I thank Taran Huffman for the helpful discussions and his excellent work in fabricating nearly all the devices in this thesis, and Phillip Skahan for the brief collaboration I had with him on the coherent receiver project. I especially thank Grant Brodnik for his invaluable help with the Brillouin measurements which form a central part of this dissertation. Our all-nighters, costco pizzas, free-birds burritos, and ample amount of coffee resulted in the noise measurements of Brillouin laser and I thank him for that. I thank Debapam Bose for helping in the fabrication of Brillouin laser resonators, and Nitesh Chauhan, Zhenlin Su, Jiawei Wang, and Mark Harrington for their help in the Brillouin laser project. I must thank Tin Komljenovic and Minh Tran from Bowers group for their continued collaboration, excellent advice, helpful discussions, and sharing their knowledge. I thank Paolo Pintus for the friendly times and helpful discussions. Also, I thank Demis John, Sudarshanan Srinivasan, Michael Davenport, Geza Kurczveil, Chong Zhang, Aaron Bluestone, Eric Stanton, Lin Chang, Aditya Jain, Warren Jin, Tony Huang, Yichen Shen, Sangtao Liu, Shamsul Arafin, and numerous other researchers on campus for their help and for making UCSB a better place to work.

Transitioning from an undergrad in electronics engineering to a software professional, then in to a photonics researcher at UCSB has been a rollercoaster of a ride and I cherish every bit of it. I especially thank my teachers Raghu Ram, Eeshwar, Murthy, and Vamsi Krishna for their encouragement. I thank Thirupathi Namani, Vamsi Patnam, Vijay Kalidindi, and Anil Wali from Broadridge for their friendship, support, and encouragement. I must thank Henrik Poulsen Dave Kinghorn, Holger Klein, and Duncan Mcmillan for all the good times and learnings I had at Packet Photonics. I must thank Vishnuvardhan Reddy, Ajay Raman, Karthik Krishnaswamy, Sathiish Kumar, Madhukar Kedlaya, Pragya Singh, Gaurav Malik, Arjun Muralidharan, Saandeep Depatla, and a lot of other friends for making my time in Santa Barbara worth remembering.

Family has been the central part of my personal life and has been instrumental in all the decisions I have made my life so far. I would like to thank my grandparents Narasamma, and Sambasiva Rao for their inspirational life, who starting off from a modest farming background and worked hard to make my father a post graduate. I must thank my uncle J.V.S. Mohan whose love for all personality and scientific temperament continue to inspire me.

Lastly, I am eternally indebted to my parents and my brother for being a constant pillar of support in my life. It is impossible for me to acknowledge their contribution in words, but I make a humble attempt to do so by dedicating this dissertation to them. I extend my thanks to my sister-in-law, Arti and my little nephew, Sooryansh for their support and the happiness they brought into our family.

Dedicated to my parents Bapeswara Sarma, Usha Rani, and my brother Chaitanya

VITA OF SARAT CHANDRA GUNDAVARAPU

December 2018

EDUCATION

Doctor of Philosophy in Electrical and Computer Engineering — *Dec'18*
University of California Santa Barbara, CA, 93106, U.S.A.

Master of Science in Electrical and Computer Engineering — *Sep'14*
University of California Santa Barbara, CA, 93106, U.S.A.

Bachelor of Technology in Electronics and Communication Engineering — *Apr'07*
Jawaharlal Nehru Technological University, Hyderabad, India

PROFESSIONAL EMPLOYMENT

Graduate Student Researcher — *Jan'14 – Sep'18*
Department of Electrical and Computer Engineering, UCSB

Optical Chip Test Intern — *Jun'13 – Sep'14*
Packet Photonics, Santa Barbara, CA, USA

Grader — *Sep'13 – Dec'13*
Department of Electrical and Computer Engineering, UCSB

Teaching Assistant — *Apr'13 – Jun'13*
Department of Physics, UCSB

Member Technical — *Oct'07 – Sep'11*
Broadridge Financial Solutions, Hyderabad, India

PUBLICATIONS

[1] T. A. Huffman, G. M. Brodnik, C. Pinho, ***S. Gundavarapu***, D. Baney, and D. J. Blumenthal, "Integrated Resonators in Ultra-Low Loss Si_3N_4/SiO_2 for Multifunction Applications," IEEE J. Sel. Top. Quantum Electron., no. c, 2018.

[2] ***S. Gundavarapu*** et al., "Sub-Hz Linewidth Photonic-Integrated Brillouin Laser," arXiv:1802.10020, pp. 1–11, Feb. 2018.

[3] ***S. Gundavarapu*** et al., "Interferometric Optical Gyroscope Based on an Integrated Si_3N_4 Low-Loss Waveguide Coil," J. Light. Technol., vol. 36, no. 4, pp. 1185–1191, 2018.

[4] R. Behunin, N. T. Otterstrom, P. T. Rakich, ***S. Gundavarapu***, and D. J. Blumenthal, "Fundamental noise dynamics in cascaded-order Brillouin lasers," arXiv:1802.03894, Feb. 2018.

[5] D. J. Blumenthal, ***S. Gundavarapu***, D. Bose, G. Brodnik, T. Huffman, R. Behunin, and P.T. Rakich "Integrated Low Linewidth Brillouin Lasers in Ultra Low Loss Si_3N_4 Waveguide Platform," in Conference on Lasers and Electro-Optics, 2018, p. FW3E.3.

[6] D. J. Blumenthal, T. Huffman, M. Belt, and ***S. Gundavarapu***, "Ultra-Low Loss Si3N4 Planar Waveguide Platform and Applications," in 2017 European Conference on Optical Communication (ECOC), 2017, pp. 1–3.

[7] ***S. Gundavarapu*** et al., "Integrated Waveguide Brillouin Laser," arXiv:1709.04512, pp. 1–15, Sep. 2017.

[8] ***S. Gundavarapu*** et al., "Integrated Sagnac optical gyroscope sensor using ultra-low loss high aspect ratio silicon nitride waveguide coil," vol. 10323, p. 103231A, 2017.

[9] ***S. Gundavarapu***, T. Komljenovic, M. A. Tran, M. Belt, J. E. Bowers, and D. J. Blumenthal, "Effect of direct PRBS modulation on laser driven fiber optic gyroscope," 4th IEEE Int. Symp. Inert. Sensors Syst. Inert. 2017 - Proc., vol. 1, pp. 1–3, 2017.

[10] ***S. Gundavarapu***, T. Huffman, R. Moreira, M. Belt, J. E. Bowers, and J. Daniel, "Integrated Ultra-Low-Loss Silicon Nitride Waveguide Coil for Optical Gyroscopes," Opt. Fiber Commun. Conf. 2016, vol. 1, pp. 4–6, 2016.

[11] R. Moreira, ***S. Gundavarapu***, and D. J. Blumenthal, "Programmable eye-opener lattice filter for multi-channel dispersion compensation using an integrated compact low-loss silicon nitride platform," Opt. Express, vol. 24, no. 15, p. 16732, 2016.

[12] M. A. Tran, ***S. Gundavarapu***, M. Belt, T. Komljenovic, D. J. Blumenthal, and J. E. Bowers, "Frequency Modulated Laser Based Interferometric Optical Gyroscope," CLEO Appl. Technol., p. JTu5A.140, 2016.

[13] T. Komljenovic, M. A. Tran, M. Belt, ***S. Gundavarapu***, D. J. Blumenthal, and J. E. Bowers, "Frequency modulated lasers for interferometric optical gyroscopes," Opt. Lett., vol. 41, no. 8, p. 1773, 2016.

[14] R. Moreira, ***S. Gundavarapu***, and D. Blumenthal, "Compact Programmable Monolithically Integrated 10-Stage Multi-Channel WDM Dispersion Equalizer on Low-Loss Silicon Nitride Planar Waveguide Platform," Opt. Fiber Commun. Conf. 2015, pp. 10–12, 2015.

[15] P. J. Skahan, ***S. Gundavarapu***, K. N. Nguyen, D. M. Baney, and D. J. Blumenthal, "Monolithically integrated dual-channel coherent receiver with widely tunable local oscillator for 100 Gbps dual-polarization quadrature phase shift keying applications," Opt. Lett., vol. 40, no. 18, p. 4313, Sep. 2015.

PATENTS

Blumenthal, Daniel, Holger Klein, Chad Althouse, Todd Chicci, Patrick Bybee, Henrik Poulsen, and ***Sarat Chandra Gundavarapu***. "Fast calibration and programming optical components." U.S. Patent 9,543,737, issued January 10, 2017.

BOOK CHAPTERS

Demis D. John, Grant Brodnik, ***Sarat Gundavarapu***, Renan L. Moreira, Michael Belt, Taran Huffman and Daniel J. Blumenthal, Chapter 11 "Low-Loss Photonic Integration: Applications in Datacenters" in "Datacenter Connectivity Technologies: Principles and Practice", River Publishers, 2018.

HONORS

1. Best Student Paper Award in honor of *"Shaoul Ezekiel"* at "The 25th International Conference on Optical Fiber Sensors", Jeju, South Korea, April 2017
2. Doctoral Student Travel Grant, Academic Senate, University of California Santa Barbara, April 2017

Abstract

Sub-Hz Fundamental Linewidth Silicon Nitride Integrated Brillouin Lasers and Their Applications

The growing demand for high-performance system-on-chip photonic solutions is pushing for rapid performance advancements in photonic integrated circuits (PICs) and more specifically, spectrally pure chip-scale lasers. The creation of laser sources with low frequency and amplitude noise is critical for the wide range of future on-chip applications that will span operating ranges from the visible to infrared wavelengths, including coherent optical communications, microwave photonics, metrology, sensing, and spectroscopy. Brillouin lasers offer unprecedented sub-Hz linewidth performance with the ability to operate across this wide wavelength range, yet today these lasers are built with fiber-based or micro-optic discrete components. The important next step of realizing these lasers that are compatible for integration with other optical components and wafer-scale processing has remained elusive.

This thesis describes the first demonstration of foundry compatible, sub-Hz (~0.7 Hz) fundamental linewidth photonic-integrated all-waveguide Brillouin laser. The laser comprises a high Q bus-ring resonator fabricated on the ultra-low loss (< 0.5 dB/m) Si_3N_4 waveguide platform that supports operation from 405 nm to 2350 nm and can be readily integrated with a wide array of other photonic components. The design overcomes issues with other approaches related to phonon confinement, optical cavity losses, storage of a large number of single polarization photons, sensitivity to environmental conditions and compatibility with large scale monolithic photonic integration.

The development of the integrated silicon nitride waveguide Brillouin laser has yielded three major research outcomes that form the contents of this thesis: (1) Observation of significant Brillouin gain in an integrated low optical loss waveguide that is devoid of acoustic guiding with a measured peak Brillouin gain coefficient of ~ 0.1 $m^{-1}W^{-1}$ and a gain bandwidth of 153 MHz (2) Development of a new theory for power and noise dynamics of single and cascaded order Brillouin lasers and phase noise dynamics of beat notes between cascaded Stokes orders (3) Experimental demonstration of cascaded order Brillouin lasing up to 10 Stokes orders and sub-Hz fundamental linewidth emission in an integrated waveguide laser resonator with a measured loaded Q of ~30 million.

Applications that greatly benefit from the low phase noise properties of the laser include RF (microwave and mm-wave) signal synthesis and optical gyroscopes. This thesis discusses the demonstration of a low phase noise photonic RF oscillator at a frequency of 21.8 GHz realized by photo-mixing the first and third Stokes orders of cascaded order Brillouin laser. The measured phase noise was as low as -84 dBc/Hz at 10 kHz frequency offset. This high spectral purity of the Brillouin laser and generated beat note signal indicates potential for realizing integrated laser gyroscopes. Brillouin laser based optical gyroscopes are theoretically predicted to offer higher sensitivity compared to their interferometric counterparts in a relatively smaller form factor. A qualitative performance comparison of these two gyroscope variants is presented and an interferometric integrated optical gyroscope that uses a 3 m waveguide coil is demonstrated. The results of the interferometric gyroscope indicate a rate grade performance with sensitivity of 8.52 deg/√hr and bias drift of 58.6 deg/hr.

Table of Contents

List of Figures

References

1. Poli, N., Oates, C. W., Gill, P. & Tino, G. M. Optical atomic clocks. *Riv. del Nuovo Cim.* **36,** 555–624 (2013).

2. Nicholson, T. L. *et al.* Systematic evaluation of an atomic clock at 2 × 10−18 total uncertainty. *Nat. Commun.* **6,** 6896 (2015).

3. Ye, J., Cundiff & ST. *Femtosecond optical frequency comb technology: Principle and operation and application*. *Springer* (2005).

4. Cygan, A. *et al.* Cavity mode-width spectroscopy with widely tunable ultra narrow laser. *Opt. Express* **21,** 29744 (2013).

5. Udem, T., Holzwarth, R. & Hänsch, T. W. Optical frequency metrology. *Nature* **416,** 233–237 (2002).

6. Christoforos Kachris, Bergman, K. & Ioannis Tomkos. *Optical Interconnects for Future Data Center Networks*. *Springer* (Springer New York, 2013). doi:10.1007/978-1-4614-4630-9

7. Kikuchi, K., Nakazawa, M. & Miyazaki, T. *High Spectral Density Optical Communication Technologies*. (2010). doi:10.1007/978-3-642-10419-0

8. Kakkar, A. *et al.* Laser Frequency Noise in Coherent Optical Systems: Spectral Regimes and Impairments. *Sci. Rep.* **7,** 844 (2017).

9. Pfeifle, J. *et al.* Coherent terabit communications with microresonator Kerr frequency combs. *Nat. Photonics* **8,** 375–380 (2014).

10. Li, J., Suh, M.-G. & Vahala, K. Microresonator Brillouin gyroscope. *Optica* **4,** 346 (2017).

11. Li, J., Suh, M. G. & Vahala, K. Stimulated Brillouin laser microcavity gyroscope. *2016 IEEE Photonics Conf. IPC 2016* **1,** 345–346 (2016).

12. Kadiwar, R. K. & Giles, I. Optical Fibre Brillouin Ring Laser Gyroscope. *Electron. Lett.* **25,** 1729–1731 (1989).

13. B. C. Young W. M. Itano, F. C. C. & Bergquist, J. C. Visible Lasers with Sub Hertz Linewidths. *Phys. Rev. Lett.* **82, 3799,** N--N (1999).

14. Smith, S. P., Zarinetchi, F. & Ezekiel, S. Narrow-linewidth stimulated Brillouin fiber laser and applications. *Opt. Lett.* **16,** 393 (1991).

15. Li, J., Lee, H., Chen, T. & Vahala, K. J. Characterization of a high coherence, Brillouin microcavity laser on silicon. *Opt. Express* **20,** 20170 (2012).

16. Grudinin, I. S., Matsko, A. B. & Maleki, L. Brillouin lasing with a CaF2 whispering gallery mode resonator. *Phys. Rev. Lett.* **102,** 1–4 (2009).

17. Loh, W., Papp, S. B. & Diddams, S. A. Noise and dynamics of stimulated-Brillouin-scattering microresonator lasers. *Phys. Rev. A - At. Mol. Opt. Phys.* **91,** 1–17 (2015).

18. Debut, A., Randoux, S. & Zemmouri, J. Linewidth narrowing in Brillouin lasers: Theoretical analysis. *Phys. Rev. A - At. Mol. Opt. Phys.* **62,** 1–4 (2000).

19. Behunin, R., Otterstrom, N. T., Rakich, P. T., Gundavarapu, S. & Blumenthal, D. J. Fundamental noise dynamics in cascaded-order Brillouin lasers. **023832,** 1–17 (2018).

20. Corbett, J. C. *et al.* Spanner: Google's globally distributed database. *Google's Glob. Distrib. Database* **31,** 1–22 (2013).

21. Cisco Visual Networking Index: Forecast and methodology, 2016-2021, White paper. (2016).

22. Cisco Global Cloud Index: Forecast and methodology, 2016-2021, White paper. (2017).

23. Pfau, T., Hoffmann, S. & Noé, R. Hardware-efficient coherent digital receiver concept with feedforward carrier recovery for M-QAM constellations. *J. Light. Technol.* **27,** 989–999 (2009).

24. Iglesias Olmedo, M. *et al.* Effective Linewidth of Semiconductor Lasers for Coherent Optical Data Links. *Photonics* **3,** 39 (2016).

25. Olsson, S. L. I. *et al.* Probabilistically shaped PDM 4096-QAM transmission over up to 200 km of fiber using standard intradyne detection. *Opt. Express* **26,** 4522 (2018).

26. Kessler, T. *et al.* A sub-40-mHz-linewidth laser based on a silicon single-crystal optical cavity. *Nat. Photonics* **6,** 687–692 (2012).

27. Matei, D. G. *et al.* 1.5 μ m Lasers with Sub-10 mHz Linewidth. *Phys. Rev. Lett.* **118,** 1–6 (2017).

28. IEEE/ASTM Standard for Use of the International System of Units (SI): The Modern Metric System. *IEEE/ASTM SI 10-2002 (Revision IEEE/ASTM SI 10-1997)* 0_1-62 (2002). doi:10.1109/IEEESTD.2002.94225

29. Pfeiffer, M. H. P. *et al.* Octave-spanning dissipative Kerr soliton frequency combs in Si_3N_4 microresonators. **4,** (2017).

30. Marin-Palomo, P. *et al.* Microresonator-based solitons for massively parallel coherent optical communications. *Nature* **546,** 274–279 (2017).

31. Liang, W. *et al.* High spectral purity Kerr frequency comb radio frequency photonic oscillator. *Nat. Commun.* **6,** 7957 (2015).

32. ABao, C. *et al.* Dependence of a microresonator Kerr frequency comb on the pump linewidth. *Opt. Lett.* **42,** 779 (2017).

33. Mooradian, A. Laser Linewidth. *Phys. Today* **38,** 42–48 (1985).

34. Vig, J. R. *(IEEE Standard 1139-1999) IEEE Standard Definitions of Physical Quantities for Fundamental Frequency and Time Metrology - Random Instabilities. IEEE Standard 1139* (1999). doi:10.1109/IEEESTD.1999.90575

35. Di Domenico, G., Schilt, S. & Thomann, P. Simple approach to the relation between laser frequency noise and laser line shape. *Appl. Opt.* **49,** 4801 (2010).

36. Halford, D., Shoaf, J. H. & Risley, A. S. Spectral Density Analysis: Frequency Domain Specification and Measurement of Signal Stability. in *27th Annual Symposium on Frequency Control* 421–431 (IEEE, 1973). doi:10.1109/FREQ.1973.199988

37. Salomon, C., Hils, D. & Hall, J. L. Laser stabilization at the millihertz level. *J. Opt. Soc. Am. B* **5,** 1576 (1988).

38. Hjelme, D. R., Mickelson, A. R. & Beausoleil, R. G. Semiconductor Laser Stabilization By External Optical Feedback. *IEEE J. Quantum Electron.* **27,** 352–372 (1991).

39. Liang, W. *et al.* Whispering gallery mode resonator based ultra-narrow linewidth external cavity semiconductor laser. *Opt. Lett.* **35,** 2822–2824 (2010).

40. Suh, M.-G., Yang, Q.-F. & Vahala, K. J. Phonon-Limited-Linewidth of Brillouin Lasers at Cryogenic Temperatures. *Phys. Rev. Lett.* **119,** 143901 (2017).

41. Spencer, D. T., Bauters, J. F., Heck, M. J. R. & Bowers, J. E. Integrated waveguide coupled Si_3N_4 resonators in the ultrahigh-Q regime. *Optica* **1,** 153 (2014).

42. Santis, C., Vilenchik, Y., Yariv, A., Satyan, N. & Rakuljic, G. Sub-kHz Quantum Linewidth Semiconductor Laser On Silicon Chip. in *CLEO: 2015 Postdeadline Paper Digest* **1,** JTh5A.7 (OSA, 2015).

43. Liang, W. *et al.* Ultralow noise miniature external cavity semiconductor laser. *Nat. Commun.* **6,** 7371 (2015).

44. Kippenberg, T. J., Spillane, S. M., Min, B. & Vahala, K. J. Theoretical and experimental study of stimulated and cascaded Raman scattering in ultrahigh-Q optical microcavities. *IEEE J. Sel. Top. Quantum Electron.* **10,** 1219–1228 (2004).

45. Geng, J. *et al.* Highly stable low-noise brillouin fiber laser with ultranarrow spectral linewidth. *IEEE Photonics Technol. Lett.* **18,** 1813–1815 (2006).

46. Lee, H. *et al.* Chemically etched ultrahigh-Q wedge-resonator on a silicon chip. *Nat. Photonics* **6,** 369–373 (2012).

47. Kabakova, I. V. *et al.* Narrow linewidth Brillouin laser based on chalcogenide photonic chip. *Opt. Lett.* **38,** 3208 (2013).

48. Otterstrom, N. T., Behunin, R. O., Kittlaus, E. A., Wang, Z. & Rakich, P. T. A silicon Brillouin laser. *Science (80-.).* **360,** 1113–1116 (2018).

49. Qiu, W. *et al.* Stimulated Brillouin scattering in nanoscale silicon step-index waveguides: a general framework of selection rules and calculating SBS gain. *Opt. Express* **21,** 31402 (2013).

50. Rakich, P. T., Reinke, C., Camacho, R., Davids, P. & Wang, Z. Giant enhancement of stimulated Brillouin scattering in the subwavelength limit. *Phys. Rev. X* **2,** 1–15 (2012).

51. Gundavarapu, S. *et al.* Integrated Waveguide Brillouin Laser. *arXiv:1709.04512* 1–15 (2017).

52. Gundavarapu, S. *et al.* Sub-Hz Linewidth Photonic-Integrated Brillouin Laser.

arXiv:1802.10020 1–11 (2018).

53. Brillouin, L. Diffusion de la lumière et des rayons X par un corps transparent homogène-Influence de l'agitation thermique. in *Annales de physique* **9,** 88–122 (1922).

54. Mandelstam, L. I. Light scattering by inhomogeneous media. *Zh. Russ. Fiz-Khim. Ova* **58,** 381 (1926).

55. Chiao, R. Y., Townes, C. H. & Stoicheff, B. P. Stimulated brillouin scattering and coherent generation of intense hypersonic waves. *Phys. Rev. Lett.* **12,** 592–595 (1964).

56. Maiman, T. H. Stimulated optical radiation in Ruby. *Nature* **187,** 493–494 (1960).

57. Ippen, E. P. & Stolen, R. H. Stimulated Brillouin scattering in optical fibers. *Appl. Phys. Lett.* **21,** 539–541 (1972).

58. Hill, K. O., Kawasaki, B. S. & Johnson, D. C. cw Brillouin laser. *Appl. Phys. Lett.* **28,** 608–609 (1976).

59. Pant, R. *et al.* On-chip stimulated Brillouin scattering. *Opt. Express* **19,** 8285 (2011).

60. Vernooy, D. W., Ilchenko, V. S., Mabuchi, H., Streed, E. W. & Kimble, H. J. High-Q measurements of fused-silica microspheres in the near infrared. *Opt. Lett.* **23,** 247 (1998).

61. Lu, T., Yang, L., Carmon, T. & Min, B. A Narrow-Linewidth On-Chip Toroid Raman Laser. *IEEE J. Quantum Electron.* **47,** 320–326 (2011).

62. Armani, D. K., Kippenberg, T. J., Spillane, S. M. & Vahala, K. J. Ultra-high-Q toroid microcavity on a chip. *Nature* **421,** 925–928 (2003).

63. Loh, W. *et al.* A microrod-resonator Brillouin laser with 240 Hz absolute linewidth. *New J. Phys.* **18,** (2016).

64. Shin, H. *et al.* Tailorable stimulated Brillouin scattering in nanoscale silicon waveguides. *Nat. Commun.* **4,** 1944 (2013).

65. Gundavarapu, S. *et al.* Sub-Hz Linewidth Photonic-Integrated Brillouin Laser. 1–11 (2018).

66. Huffman, T. A. *et al.* Integrated Resonators in Ultra-Low Loss Si3N4/SiO2 for Multifunction Applications. *IEEE J. Sel. Top. Quantum Electron.* (2018). doi:10.1109/JSTQE.2018.2818459

67. Blumenthal, D. J., Heideman, R., Geuzebroek, D., Leinse, A. & Roeloffzen, C. Silicon Nitride in Silicon Photonics. *Proc. IEEE* **106,** 2209–2231 (2018).

68. Pierson, H. O. *Handbook of chemical vapor deposition (CVD) - principles, technology, and applications*. *Advanced Materials* **5,** (1999).

69. Foggiato, J. Chemical Vapor Deposition of Silicon Dioxide Films. in *Thin-Film Deposition Processes and Technologies* 111–150 (2012). doi:http://dx.doi.org/10.1016/B978-081551442-8.50008-0

70. Poulton, C. G., Pant, R. & Eggleton, B. J. Acoustic confinement and stimulated Brillouin scattering in integrated optical waveguides. *J. Opt. Soc. Am. B* **30,** 2657 (2013).

71. Pant, R. *et al.* On-chip stimulated brillouin scattering for microwave signal processing and generation. *Laser Photonics Rev.* **8,** 653–666 (2014).

72. Le Floch, S. & Cambon, P. Theoretical evaluation of the Brillouin threshold and the steady-state Brillouin equations in standard single-mode optical fibers. *J. Opt. Soc. Am. A* **20,** 1132 (2003).

73. Li, J., Lee, H., Yang, K. Y. & Vahala, K. J. Sideband spectroscopy and dispersion measurement in microcavities. *Opt. Express* **20,** 26337 (2012).

74. Bogaerts, W. *et al.* Silicon microring resonators. *Laser Photonics Rev.* **6,** 47–73 (2012).

75. Vahala, K. J. Back-action limit of linewidth in an optomechanical oscillator. *Phys. Rev. A - At. Mol. Opt. Phys.* **78,** 1–4 (2008).

76. Matsko, A. B., Savchenkov, A. A. & Maleki, L. Stability of resonant opto-mechanical oscillators. *Opt. Express* **20,** 16234 (2012).

77. Küng, A. *L'émission laser par diffusion Brillouin stimulée dans les fibres optiques*. (1997).

78. Eggleton, B. J., Poulton, C. G. & Pant, R. Inducing and harnessing stimulated Brillouin scattering in photonic integrated circuits. *Adv. Opt. Photonics* **5,** 536 (2013).

79. Drever, R. W. P. *et al.* Laser phase and frequency stabilization using an optical resonator. *Appl. Phys. B Photophysics Laser Chem.* **31,** 97–105 (1983).

80. Büttner, T. F. S. *et al.* Phase-locking and Pulse Generation in Multi-Frequency Brillouin Oscillator via Four Wave Mixing. *Sci. Rep.* **4,** 16–17 (2014).

81. Morrison, B. *et al.* Compact Brillouin devices through hybrid integration on Silicon. *Optica* **4,** 847 (2017).

82. Dennis Derickson. Fiber Optic Test and Measurement. in *Fiber optic test and measurement edited by Dennis Derickson. Upper Saddle River, NJ: Prentice Hall, c1998.* (1997).

83. Lim, J. *et al.* Chasing the thermodynamical noise limit in whispering-gallery-mode resonators for ultrastable laser frequency stabilization. *Nat. Commun.* **8,** 8 (2017).

84. Spencer, D. T., Davenport, M. L., Komljenovic, T., Srinivasan, S. & Bowers, J. E. Stabilization of heterogeneous silicon lasers using Pound-Drever-Hall locking to Si_3N_4 ring resonators. *Opt. Express* **24,** 13511 (2016).

85. Matsko, A. B., Savchenkov, A. A., Yu, N. & Maleki, L. references . I . Fundamental limitations. **24,** 1324–1335 (2007).

86. Epping, J. P. *et al.* Ultra-low-power stress-optics modulator for microwave photonics. *Proc. SPIE, Integr. Opt. Devices, Mater. Technol. XXI* **10106,** 101060F (2017).

87. Loh, W. *et al.* Dual-microcavity narrow-linewidth Brillouin laser. *Optica* **2,** 225 (2015).

88. Bucalovic, N. *et al.* Experimental validation of a simple approximation to determine the linewidth of a laser from its frequency noise spectrum. *Appl. Opt.* **51,** 4582 (2012).

89. Alavi, S. E. *et al.* Towards 5G: A Photonic Based Millimeter Wave Signal Generation for Applying in 5G Access Fronthaul. *Sci. Rep.* **6,** 1–11 (2016).

90. Merklein, M. *et al.* Widely tunable, low phase noise microwave source based on a photonic chip. *Opt. Lett.* **41,** 4633 (2016).

91. Li, J., Lee, H. & Vahala, K. J. Microwave synthesizer using an on-chip Brillouin oscillator. *Nat. Commun.* **4,** 2097 (2013).

92. Spencer, D. T. *et al.* An optical-frequency synthesizer using integrated photonics. *Nature* **557,** 81–85 (2018).

93. King, A. D. Inertial navigation - Forty years of evolution. *Gec Rev.* **13,** 140–149 (1998).

94. Barbour, N. Inertial navigation sensors. *NATO RTO Lect. Ser.* **116,** 1–24 (2004).

95. Gundavarapu, S. *et al.* Interferometric Optical Gyroscope Based on an Integrated Si3N4 Low-Loss Waveguide Coil. *J. Light. Technol.* **36,** 1185–1191 (2018).

96. Sanders, G. A. *et al.* Honeywell. **985207,** 985207 (2017).

97. Bayvel, P. & Giles, I. P. Evaluation of performance parameters of single-mode all-fiber Brillouin ring lasers. *Opt. Lett.* **14,** 581–3 (1989).

98. Nicati, P.-A., Toyama, K. & Shaw, H. J. Frequency stability of a Brillouin fiber ring laser. *J. Light. Technol.* **13,** 1445–1451 (1995).

99. Dell'Olio, F., Tatoli, T., Ciminelli, C. & Armenise, M. N. Recent advances in miniaturized optical gyroscopes. *J. Eur. Opt. Soc.* **9,** (2014).

100. Lefèvre, H. *The fiber-optic gyroscope*. (Artech house, 1993).

101. Bauters, J. F. *et al.* Planar waveguides with less than 01 dB/m propagation loss fabricated with wafer bonding. *Opt. Express* **19,** 24090 (2011).

102. Leinse, A., Shaoxian Zhang & Heideman, R. TriPleX: The versatile silicon nitride waveguide platform. *2016 Prog. Electromagn. Res. Symp.* 67–67 (2016). doi:10.1109/PIERS.2016.7734240

103. Bauters, J. F. *et al.* Ultralow-loss planar Si3N4 waveguide polarizers. *IEEE Photonics J.* **5,** 0–7 (2013).

104. Tien, M.-C., Bauters, J. F., Heck, M. J. R., Blumenthal, D. J. & Bowers, J. E. Ultra-low loss Si_3N_4 waveguides with low nonlinearity and high power handling capability. *Opt. Express* **18,** 23562 (2010).

105. Srinivasan, S., Moreira, R., Blumenthal, D. & Bowers, J. E. Design of integrated hybrid silicon waveguide optical gyroscope. *Opt. Express* **22,** 24988 (2014).

106. Tran, M. A. *et al.* Integrated optical driver for interferometric optical gyroscopes. *Opt. Express* **4,** 3826–3840 (2017).

107. Huffman, T., Davenport, M., Belt, M., Bowers, J. E. & Blumenthal, D. J. Ultra-low loss stitching for large-area waveguide based delay-line gyroscopes. in *2016 IEEE Photonics Conference (IPC)* 478–479 (IEEE, 2016). doi:10.1109/IPCon.2016.7831188

108. Huffman, T., Davenport, M., Belt, M., Bowers, J. E. & Blumenthal, D. J. Ultra-low loss large area waveguide coils for integrated optical gyroscopes. *IEEE Photonics Technol. Lett.* **29,** 185–188 (2017).

109. Gundavarapu, S. *et al.* Integrated Sagnac optical gyroscope sensor using ultra-low loss high aspect ratio silicon nitride waveguide coil. **10323,** 103231A (2017).

110. Gundavarapu, S. *et al.* Integrated Ultra-Low-Loss Silicon Nitride Waveguide Coil for Optical Gyroscopes. *Opt. Fiber Commun. Conf. 2016* **1,** 4–6 (2016).

111. Ieee. *IEEE Standard Specification Format Guide and Test Procedure for Single –Axis Interferometric Fiber Optic Gyros*. *IEEE Std 952-1997* **1997,** (1998).

112. Komljenovic, T. *et al.* Frequency modulated lasers for interferometric optical gyroscopes. *Opt. Lett.* **41,** 1773 (2016).

113. Gundavarapu, S. *et al.* Effect of direct PRBS modulation on laser driven fiber optic gyroscope. *4th IEEE Int. Symp. Inert. Sensors Syst. Inert. 2017 - Proc.* **1,** 1–3 (2017).

114. Tran, M. A. *et al.* Frequency Modulated Laser Based Interferometric Optical Gyroscope. *CLEO Appl. Technol.* JTu5A.140 (2016). doi:10.1364/CLEO_AT.2016.JTu5A.140

115. Tran, M. A. *et al.* Frequency Modulated Laser Based Interferometric Optical Gyroscope. in *CLEO: Applications and Technology* JTu5A.140 (2016). doi:10.1364/CLEO_AT.2016.JTu5A.140

116. Chamoun, J. & Digonnet, M. J. F. Aircraft-navigation-grade laser-driven FOG with Gaussian-noise phase modulation. *Opt. Lett.* **42,** 1600 (2017).

117. Digonnet, M. J. F. & Chamoun, J. N. Recent developments in laser-driven and hollow-core fiber optic gyroscopes. **9852,** 985204 (2016).

118. Papes, M. *et al.* Fiber-chip edge coupler with large mode size for silicon photonic wire waveguides. *Opt. Express* **24,** 5026 (2016).

119. Bauters, J. F. *et al.* Silicon on ultra-low-loss waveguide photonic integration platform. *Opt. Express* **21,** 544–555 (2013).

120. Puckett, M. W., Wu, J. & Nelson, K. D. Apparatus and method for a low loss, high q resonator. (2018).

121. Puckett, M. W. & Salit, M. K. Optical waveguide having a wide brillouin bandwidth. (2018).

122. Puckett, M. W. Double-layer high-confinement acousto-optic waveguide. (2018).

123. Puckett, M. W., Qiu, T., Salit, M. K. & Wu, J. Acoustic ridge or rib waveguides in low-loss integrated optical platforms. (2018).

Key Publications and Contributors

- "Sub-Hz Fundamental Linewidth Photonic-Integrated Brillouin Laser", Nature Photonics (Accepted, 2018)

  Authors: Sarat Gundavarapu (**S.G.**), Grant M. Brodnik (**G.B.**), Matthew Puckett (**M.P.**), Taran Huffman (**T.H.**), Debapam Bose (**D.B.**), Ryan Behunin (**R.B.**), Jianfeng Wu (**J.W.**), Tiequn Qiu (**T.Q.**), Cátia Pinho (**C.P.**), Nitesh Chauhan (**N.C.**), Jim Nohava (**J.N.**), Peter T. Rakich (**P.R.**), Karl D. Nelson (**K.N.**), Mary Salit (**M.S.**), Daniel J. Blumenthal (**D.J.B.**)

- "Fundamental noise dynamics in cascaded-order Brillouin lasers". **023832,** 1–17 (2018).

  Authors: Behunin, R. (**R.B.**), Otterstrom, N. T.(**N.O.**), Rakich, P. T. (**P.R.**), Gundavarapu, S. (**S.G.**) & Blumenthal, D. J. (**D.J.B.**)

- "Interferometric Optical Gyroscope Based on an Integrated Si_3N_4 Low-Loss Waveguide Coil," *J. Light. Technol.*, vol. 36, no. 4, pp. 1185–1191, 2018

  Authors: Gundavarapu, S. (**S.G.**), Belt, M. (**M.B.**), Huffman, T (**T.H.**)., Tran, M. A. (**M.T.**), Komljenovic, T. (**T.K.**), Bowers, J. E. (**J.B.**), & Blumenthal, D. J (**D.J.B.**)

The name abbreviations will be used in specifying the chapter contributions.

Chapter 1: Introduction

1.1 Abstract

High coherence, low phase noise lasers have been central to the technological advances of a variety of applications including atomic clocks[1–3], high precision spectroscopy[4], metrology[5], coherent communications[6–9], and sensing[10–12]. Over the past decades, remarkable progress has been made in reduction of laser phase noise to realize narrow linewidth, single frequency lasers that can operate from visible[13] to infrared[14–16] wavelengths. Traditional linewidth narrowing techniques such as extended cavity configuration and frequency stabilization of seed laser to bulky high-finesse cavities have demonstrated laser linewidths below 1 Hz, but come at the price of size, power, cost, and added system complexity. Moreover, limitations of the typically achievable locking bandwidth (< 1 MHz) prevent laser frequency stabilization beyond this range[17]. These issues combined with the more stringent noise requirements of future applications entail realization of intrinsically low phase noise integrated lasers[18,19]. Engineering such laser systems in a small form factor requires an understanding of the metrics and physical mechanisms responsible for deterioration of laser spectral purity. This chapter reviews the concepts and terminology of laser spectral noise, and common approaches for laser linewidth narrowing, and presents an overview of future applications that demand low phase noise integrated lasers with Hertz-level linewidths. Finally, this chapter presents the structure of the thesis.

1.2 Motivation for Integrated Narrow Linewidth Lasers

The growing demands of the rapidly increasing photonic system-on-chip applications entail lasers with higher spectral coherence in a smaller form factor and has propelled considerable

amount of research effort towards the realization of integrated ultra-narrow-linewidth lasers. Applications pushing for this transition (see Figure 1.1) span from the visible to infrared wavelengths and include ultra-high capacity coherent communications, atomic clocks, microwave photonics, optical gyroscopes, optical comb generation, and emerging cross-over applications such as atomic clock-based data center database synchronization like Google SPANNER[20] and TrueTime. This section reviews the phase noise requirements of two major future applications with a special focus on realization of integrated sub-Hz linewidth lasers for next generation photonic systems.

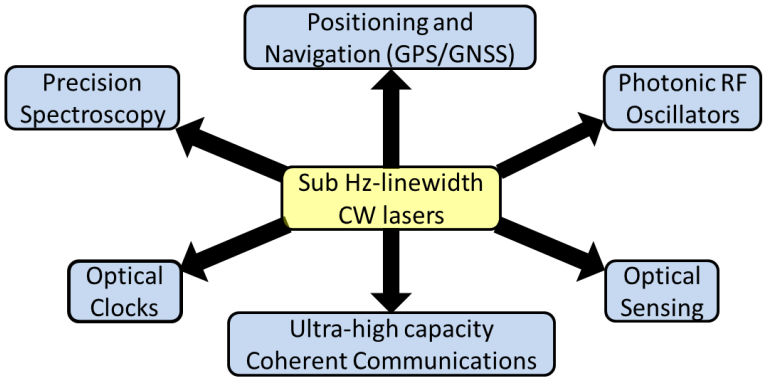

Figure 1.1. Key applications that benefit from sub-Hz linewidth CW lasers: *Development of sub-Hz linewidth lasers can enable a variety of future applications like long-haul high-bit rate coherent communications for energy-efficient optical data center interconnects, high performance laser optical gyroscopes for positioning and navigation, optical clocks (probe lasers locked to atomic/ionic references) with ultra-high frequency stability, and high spectral purity photonic microwave and mm-wave oscillators*

1.2.1 Coherent Communications and Data Center Interconnects

Many of the key advances in integrated photonics continue to stem from the need for improvements in the communications technology to handle the increasing internet data traffic. The annual run rate of global IP traffic was more than a zettabyte in 2016 and is projected to be grow threefold by 2021, indicating a compound annual growth rate (CAGR) of 24 %[21]. This exponential increase, primarily driven by high bandwidth video streaming content (e.g.

YouTube, Amazon, Netflix), cloud computing (e.g. Amazon, Yahoo, Facebook, Google, Microsoft), and internet of things (IoT), has necessitated more powerful warehouse data centers to mediate and administer the data transfer. With the inter-data center IP traffic surging at a CAGR of 32.7 % between 2016-2021[22], the next generation hyper-scale data centers are expected to be the most energy-intensive infrastructure, consuming more than a trillion kWh per year by 2020 and may amount to a staggering 18 %[6] of the information and communication technology (ICT) greenhouse gas emissions (GHG). This has raised serious concerns over economic and environmental impact of data centers and has drawn attention to the need to realize small-form-factor (SFF), high bandwidth, power-efficient *optical data center interconnects* (DCI) at a reduced cost. Consequently, development of high bit-rate integrated digital transceivers to be employed in coherent communication systems and metro, long haul DCIs has garnered interest of both commercial and scientific community. Specifically, coherent receivers employing quadrature amplitude modulation (QAM) scheme to transmit multiple (m) bits per symbol are widely employed in today's coherent communication systems to achieve high bit-rate and spectral efficiency. However, the size and power efficiency of these systems need to be improved to meet the exponential growth of global IP traffic. As a result, optical network architectures with chip-scale digital coherent receivers using higher-order (m) QAM (generally referred to as m-QAM) schemes are poised to be potential candidates for future communication and interconnect systems.

Low phase noise, chip-scale lasers form the backbone of these next generation, high-performance coherent systems. Optical sources with narrow linewidths and high frequency stability can dramatically enhance the achievable spectral efficiency of high capacity, long distance m-QAM systems[23]. Conversely, lasers with flicker noise dominated broad spectral

linewidths can significantly increase the overhead on the timing recovery and signal processing modules of the coherent receiver, limiting the overall system performance[8,24]. The linewidth tolerance of a coherent system worsens with the increasing order of QAM format, with even a moderately high order (256-QAM) 10 GBd system requiring a laser linewidth of < 80 kHz[23] at the receiver to realize a BER of 10^{-3}. While laser linewidths in this range (10s of kHz) may be beyond the achievable linewidths state-of-the art commercial DFB laser diodes (~100 kHz), the linewidth tolerances for future coherent systems can be more stringent, in the order of sub-Hertz. Recently, a 200 km link based on probabilistically shaped 3 GBd 4096-QAM scheme[25] used a 1-Hz linewidth laser at the transmitter and a <100-Hz laser at the receiver to demonstrate spectral efficiency as high as ~19 bit/s/Hz. Enabling this level of performance for higher bit-rates at a chip-scale demands realization of integrated sub-Hz linewidth lasers to create next-generation photonic network-on-chip solutions for future high capacity long-haul DCIs and coherent communication systems.

1.2.2 Metrology and Spectroscopy

Another application area that both hugely benefited from and contributed to the advancement of spectrally pure lasers is the development of accurate frequency standards[5] and clocks[1,2]. Particularly, technological advances in precision spectroscopy[4] have enabled furthering the improvements in metrological standards of both length and time. Consequently, a range of state-of-the-art applications including optical sensing[11], positioning and navigation (GPS, GNSS)[3], and path-breaking scientific discoveries like gravitational wave detection[26,27] have all reaped the benefits of enhanced metrological standards.

Among these standards, the "second" acts as the "ruler" or the defining parameter for three other SI units (meter, candela, and ampere)[28], owing to the astounding uncertainties

approaching 1 part in 10^{18} achievable by current clocks[3]. Realizing this level of clock stability is made possible through precision spectroscopy of ultra-narrow atomic resonance widths using highly frequency-stabilized probe lasers and self-referenced frequency combs. Atomic clocks based on single Hg^{+} ions require a pre-stabilized probe laser with a sub-Hz linewidth[3]. Octave spanning optical frequency combs required for absolute optical frequency measurements have traditionally used femto-second mode locked lasers[5] and are now being replaced by microresonator based dissipative Kerr soliton (DKS) combs[29]. These combs have also been demonstrated to be useful in parallel coherent communications[9,30] and high-spectral purity photonic RF generation[31]. Given the dependence of comb linewidth on the pump linewidth[32] and stringent linewidth requirements of probe lasers for optical clocks[3], realizing low phase noise, integrated sub-Hz linewidth lasers is essential to pave the way for a novel set of future photonic chip-scale metrological applications.

To meet these demands of realizing high coherence, sub-Hz linewidth laser sources in a small form factor, an understanding of the physical mechanisms and factors that degrade the spectral purity of lasers is necessary.

1.3 Spectral Noise Properties of a Laser

Laser linewidth, conventionally adopted as the sole and primary metric for characterizing the spectral purity of a laser, is insufficient for a complete understanding of the noise sources contributing to the spectral degradation. The cognizance of all these spectral noise factors is particularly important for realizing high coherence or narrow linewidth lasers and is accomplished through the analysis of phase/frequency noise fluctuations in time/frequency domain.

1.3.1 Phase and Frequency Noise

The phase noise of a laser results from the fluctuations in the optical phase of the emitted light. For single frequency lasers, this quantity describes how the phase of the laser electrical field output deviates from an ideal sinusoidal wave and causes spectral broadening (see Figure 1.2(a)). The resulting full-width half maximum (FWHM) of the laser spectral profile is conventionally referred to as linewidth of the laser. For a laser with an output electric field, $E(t) = E \cdot e^{(j\omega t + \Phi)}$ where E is the amplitude, ω is the angular frequency, and Φ is the phase angle, the noise contributions from phase diffusion and intensity variations over time result in a radial spread of field intensity ΔE, and phase fluctuation ΔΦ, as depicted in Figure 1.2(c) (figure has been adapted from the work of Aram Mooradian[33]).

This phase evolution, usually described by the (one-sided) phase noise power spectral density (PSD), $S_\Phi(\nu)$ (rad^2/Hz)[34] (see Figure 1.2(d)), can be used to segregate the noise contributions to the laser and estimate several key metrics like linewidth, coherence length, and frequency instability. Analytically, $S_\Phi(\nu)$ is the Fourier transform of the auto-correlation function of the phase angle Φ, $\langle \varphi(\tau)\varphi(\tau') \rangle$ and can be represented using Wiener–Khinchin theorem as

$$S_\varphi(\nu) = \int_{\tau=-\infty}^{\infty} \langle \varphi(\tau)\varphi(\tau') \rangle \; d\tau \, e^{j\omega\tau} \qquad (1.1)$$

Conventionally, phase noise is expressed in terms of single sideband power within a 1 Hz bandwidth at a frequency ν away from the carrier ν_0 ($\nu << \nu_0$), referenced to the carrier frequency power, denoted as $\mathcal{L}(\nu)$ (dBc/Hz) and is related to $S_\Phi(\nu)$ as[34]

$$\mathcal{L}(\nu) = 10 \cdot log_{10}\left(\frac{S_\Phi(\nu)}{2}\right) \quad (1.2)$$

Alternatively, the spectral noise contributions can also be represented using the one-sided frequency noise PSD, $S_f(\nu)$ (Hz^2/Hz) as shown in Figure 1.2(f) and is related to $S_\Phi(\nu)$ as[34]

$$S_\varphi(\nu) = \frac{S_f(\nu)}{\nu^2} \quad (1.3)$$

Equations (1.1-1.3) present a technique to identify different sources of noise that contribute to laser linewidth. The sources of noise are analyzed by examining the power-law dependence ($1/\nu^\beta$) of different regions of $S_\Phi(\nu)$ with respect to the Fourier frequency offset, ν. Flicker frequency (FF:β=3), white frequency (WF:β=2), flicker phase (FP:β=1), and white phase noise (WP:β=0) are the common noise sources of interest that impact the laser performance and are shown in Figure 1.2(d,e). Among these sources, the largest frequency deviations from the central frequency of the laser emission result from the contribution of flicker frequency noise, observed at low frequency offsets followed by white frequency noise sources (see Figure 1.2(e)). Consequently, flicker frequency noise is the primary and dominant source for laser linewidth broadening, with large flicker frequency noise components resulting in a Gaussian-like spectral profile[35].

The absolute or integral laser linewidth can be evaluated from the Fourier frequency at which the unity phase modulation index occurs. In other words, for white frequency noise, the RMS square phase noise for all Fourier frequencies exceeding the linewidth is[36–39] $\frac{1}{\pi}$ rad^2. Using this the relation between $S_\varphi(\nu)$ and the (absolute or integral) linewidth of the laser $\Delta\nu$ is given by

$$\int_{\Delta\nu}^{\infty} S_{\varphi}(\nu) = \frac{1}{\pi}\, rad^2 \qquad (1.4)$$

1.3.2 Fundamental Linewidth

In the absence of flicker frequency noise, white-frequency noise sources result in a Lorentzian spectral profile and determine the minimum achievable linewidth of a laser, referred to as "fundamental linewidth"[33]. This quantity is of crucial importance since it sets a lower limit of laser linewidth performance.

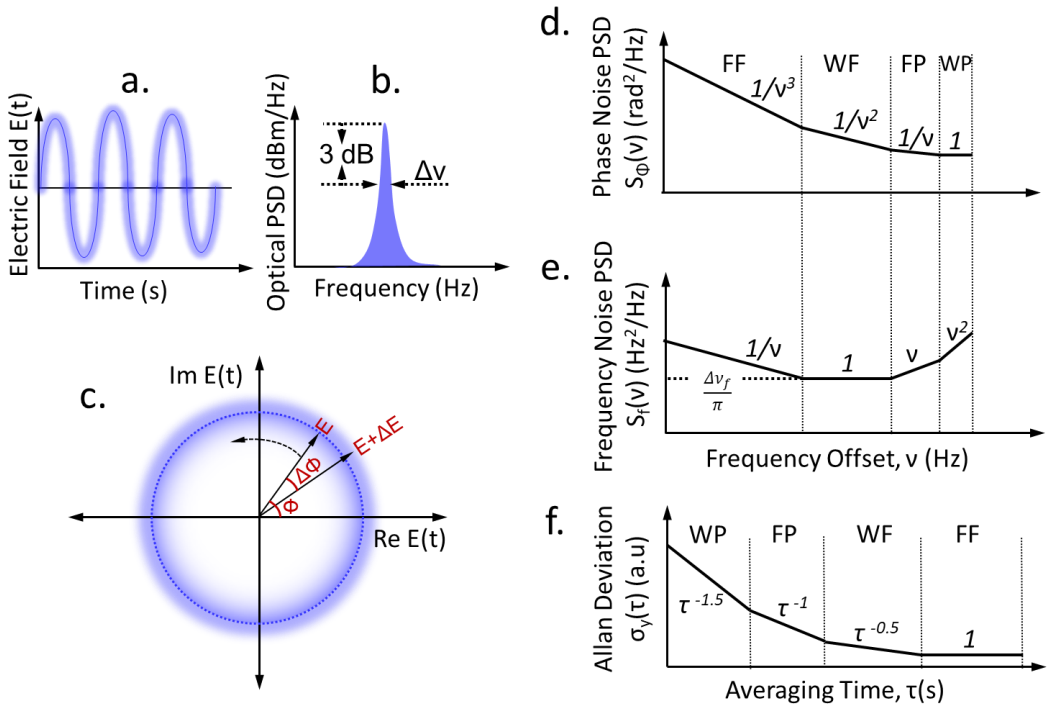

Figure 1.2. Phase Noise, Frequency Noise, and Linewidth of a single frequency laser: *(a) Output electric field of a laser distorted from an ideal sinusoidal form due to the effects of phase and intensity noise (b) Typical Lorentzian profile of a white-frequency noise limited laser spectrally broadened to a 3-dB width of Δν, commonly referred to as "laser linewidth" (c) Complex representation of laser electrical field E(t), illustrating the radial spread of intensity and phase diffusion with time (d-f) Spectral (phase(d) and frequency(e) PSD) and time domain (Allan deviation) techniques to identify and analyze various noise contributions (FF: Flicker Frequency; WF: White Frequency; FP: Flicker Phase; WP: White Phase) and frequency stability/instability of lasers – (Figures (d-f) use log-log axes and are not to scale)*

Assuming an additive white Gaussian noise (AWGN) limited laser source, the PSD $S_f(\nu)$ becomes a constant value yielding a fundamental linewidth, $\Delta\nu_f$ (see Figure 1.2(e)) of[35] (using Eq. (1.4))

$$\Delta\nu_f = \pi S_f(\nu) \qquad (1.5)$$

The value of $\Delta\nu_f$ depends on: (a) Noise contributions inherent to lasing action and varies with the type of the laser, (b) Cavity parameters such as photon damping rate (γ), and number of intra-cavity photons (N_P). For a conventional two-level laser system that employs population inversion to realize stimulated emission in a cavity, $\Delta\nu_f$ can be expressed as[40]

$$\Delta\nu_{f(2-level)} = \frac{\gamma}{4\pi N_P}\left(N_T + \frac{1}{2}\right) \qquad (1.6)$$

where N_T is the number of thermal quanta of the optical field (negligible at optical frequencies). In case of semiconductor lasers (SL), spontaneous emission (due to photon re-absorption) and amplitude to phase coupling effects increase $\Delta\nu_{f(2-level)}$ to $\Delta\nu_{f(SL)}$ given by[33]

$$\Delta\nu_{f(SL)} \approx \frac{\gamma}{8\pi N_P}(1 + \alpha^2)n_s \qquad (1.7)$$

where n_s is the spontaneous emission factor α is referred to as the linewidth enhancement factor. Equations (1.6, 1.7) represent the well-known modified *Schawlow-Townes (ST) and Schawlow-Townes-Henry linewidth* formulae respectively. Since the broadening of $\Delta\nu_{f(2-level)}$ or $\Delta\nu_{f(SL)}$ is predominantly due to quantum fluctuations, the fundamental linewidth of these lasers can also be referred to as the *quantum-limited* linewidth.

1.3.3 Fractional Frequency Stability

Another key parameter that determines the spectral purity of a laser is the wavelength or frequency (in)stability. This is quantified by measuring the variation of fractional frequency, y (= Deviation from central laser frequency, $\Delta\nu$ to the central laser frequency, ν_0) in time or frequency domain. The (one-sided) fractional frequency noise PSD, $S_y(\nu)$ (Hz^{-1}) is related to $S_f(\nu)$ as[34]

$$S_y(\nu) = \frac{S_f(\nu)}{\nu_0^2} \qquad (1.8)$$

While these spectral analysis techniques provide a means to quantify short-term fractional frequency (in)stability, time domain Allan deviation measurements are preferred for long term stability analysis (see Figure 1.2(f)). The Allan deviation, $\sigma_y(\tau)$ (a.u) and its relation to $S_y(\nu)$ is expressed as[34]

$$\sigma_y^2(\tau) = \frac{1}{2(M-1)} \sum_{i=1}^{M-1} (y_{i+1} - y_i)^2 \quad (1.8)$$

$$\sigma_y^2(\tau) = 2 \int_0^{\nu_h} S_y(\nu) \frac{sin^4(\pi\nu\tau)}{(\pi\nu\tau)^2} \, d\nu \quad (1.9)$$

where y is i^{th} fractional frequency value averaged over the measurement (sampling) interval, τ, and ν_h is the cutoff frequency of $S_f(\nu)$ measuring system in Hertz. Analogous to the spectral analysis techniques, the white frequency noise contribution can be extracted from the portions of the deviation data that exhibits $\tau^{-0.5}$ dependency. This thesis work mainly focuses on the spectral domain analysis of frequency noise, laser fundamental linewidth, and frequency instability.

1.4 Approaches for Linewidth Narrowing

Equation (1.7) brings out an important inference that ***lasers with narrow fundamental linewidths can be achieved with a cavity having low photon damping rate and high number of intra-cavity photons***. The photon damping rate of a cavity depends on the resonator cavity quality factors and the number of intra-cavity photons depends on the external power coupling of the resonator. When expressed in terms of cavity quality factor(s) and emitted power, Eq. (1.7) can be re-written as[40]

$$\Delta\nu_{f(2-level)} = \frac{\hbar\omega^3}{4\pi P Q_T Q_E}\left(N_T + \frac{1}{2}\right) \quad (1.11)$$

where $\hbar$ is the reduced Planck's constant, ω is the angular frequency of the optical source, Q_T(Q_E) is the total/loaded(external) quality factor of the cold cavity, and P is steady state emitted optical power (=$N_P\left(\frac{\hbar\omega^2}{Q_E}\right)$). Assuming no excess coupler loss[41], the dependency of the loaded quality factor ($Q_T = \frac{\omega}{\gamma}$) on the optical propagation loss, α (m^{-1}), length L (m), group index n_g, external power coupling coefficient κ^2, emission wavelength λ can be expressed as

$$\underbrace{Q_T^{-1}}_{(\kappa^2+\alpha L)\left(\frac{2\pi n_g L}{\lambda}\right)^{-1}} = \underbrace{Q_E^{-1}}_{(\kappa^2)\left(\frac{2\pi n_g L}{\lambda}\right)^{-1}} + \underbrace{Q_U^{-1}}_{(\alpha L)\left(\frac{2\pi n_g L}{\lambda}\right)^{-1}} \quad (1.12)$$

where Q_U is the unloaded or intrinsic quality factor of the cavity and is independent of cavity coupling coefficient, κ^2.

1.4.1 External Cavity Lasers

Equation (1.11, 1.12) suggest that a long, low loss cavity with low external power coupling yields high loaded quality factor, longer effective cavity length (and hence longer photon life time) and consequently, narrow fundamental linewidth. However, the low power coupling

comes at the cost of low emitted power implying a design trade-off between output power and linewidth to meet the application requirements. Moreover, degradation of mode suppression ratio (MSR) can ensue from multiple longitudinal cavity modes of a very high Q resonator. Despite these caveats, the approach of realizing longer effective cavity lengths using high Q resonator cavity is the basic operating principle for external cavity (diode) lasers and (integrated) ring resonator coupled lasers. Linewidths as low as sub-10 mHz in ultra-low expansion (ULE) glass Fabry-Pérot (FP) cavity stabilized lasers[27] and sub-kHz fundamental linewidths[42] using a high Q integrated 1-D silicon grating resonator in III-V/Si platform have been demonstrated.

However, the linewidth narrowing efficiency of these lasers is limited by the physically achievable cavity length which cannot be increased indefinitely[17]. Moreover, the cost and system complexity of high finesse cavity (e.g. ULE cavities) stabilized lasers and the associated locking bandwidth requirements limit their applicability as a low-cost solution for Hz-level spectrally pure, low phase noise lasers. Other reported techniques to realize sub-Hz linewidths like Rayleigh backscatter optical feedback based self-injection locked lasers[43] rely on foundry-incompatible high Q crystalline cavities (~10^9) making them currently impractical for low cost integration.

1.4.2 Brillouin and Raman Lasers

Nonlinear, stimulated Brillouin (Raman) scattering (SB(R)S) based lasers overcome the limitations of external cavity configuration lasers through linewidth narrowing properties[15,17–19,44] inherent to their lasing action. While inhibiting these nonlinearities in fiber-based communication systems and high-power fiber lasers is crucial to avoid undesirable effects such as transfer of energy from one channel to neighboring channels and limiting the output optical

power, these inelastic scattering mechanisms enable signal to noise reduction when employed for signal amplification and lasing. Though both Brillouin and Raman amplification processes can be used for to realize nonlinear signal amplification, features like large gain spectral bandwidth, flexibility of generating multiple wavelengths, and use of fiber as the gain medium resulted in wide-spread use of fiber-based Raman amplifiers to boost signal-to-noise ratio (SNR) in long-haul communications, and fiber-based SRS lasers in biological spectroscopic applications.

These inelastic scattering processes result in the generation of a red (down)-shifted *Stokes* photon or blue (up)-shifted *anti-Stokes* photon through the interaction of incident photons and traveling phonon gratings. The phonons mediating the transfer of energy between the incident and Stokes/anti-Stokes photons originate from the acoustic waves in the case of Brillouin scattering (referred to as acoustic phonons) and molecular vibrations in the case of Raman scattering (referred to as optical phonons). The gain imparted to the Stokes photon via scattering processes is the highest for Brillouin scattering (which is the strongest of all optical nonlinearities: Brillouin, Raman, Kerr) with a peak gain (~5e-11 m/W) in silica fibers, about 3 orders of magnitude greater than the peak Raman gain (~7e-14 m/W). The resulting Stokes frequency shift in the case of Raman scattering (13 THz) is much larger than the Brillouin frequency shift (11 GHz).

SBS proves to be the ideal choice to realize integrated narrow-linewidth lasers due to its relatively superior pump-Stokes conversion efficiency and desirable characteristics of inhibiting noise transfer from pump to Stokes[18] and relative intensity noise (RIN) suppression[45]. Debut et. al[18] showed that optomechanical coupling process of Brillouin lasing effectively suppresses the transfer of phase noise from pump to Stokes orders by a factor[18] of

$K^2 = (1+ \Gamma/\gamma)^2$, where Γ is the decay rate of the acoustic mode and (when $\Gamma > \gamma$). The total linewidth of a Brillouin laser $\Delta\nu_T$ is the sum of contribution of Schawlow-Townes linewidth $\Delta\nu_{ST}$ and contribution of pump-phase diffusion denoted as $\Delta\nu^{tr}$ and can be expressed as[16]

$$\Delta\nu_T = \Delta\nu_{ST} + \Delta\nu^{tr} = \Delta\nu_{ST} + \frac{\Delta\nu_{Pump}}{K^2} \qquad (1.13)$$

where $\Delta\nu_{Pump}$ is the linewidth of pump. Eq. (1.13) shows that the Brillouin lasing action effectively suppresses the contribution of pump phase diffusion to Stokes order and the magnitude of suppression (K^2) depends on the optical and acoustic damping rates of the cavity.

Over the past decade, advances in microfabrication and photonic integration technology have resulted in demonstration of several chip-scale microresonator based Brillouin lasers[16,46–48] with ultra-low phase and frequency noise performance indicative of fundamental linewidths as low as sub-Hz[15]. Yet, several key issues like the incompatibility of these platforms/devices for large scale integration with other photonic components and the low susceptibility of laser performance to external noise factors have remained unaddressed.

1.5 Sub-Hz Fundamental Linewidth Si_3N_4 Brillouin Laser

This thesis reports the first demonstration of sub-Hz fundamental linewidth performance in a foundry compatible, monolithically integrated bus-ring silicon nitride waveguide Brillouin laser. The Si_3N_4/SiO_2 waveguide Brillouin laser (see Figure 1.3(a)), realized in an ultra-low loss all-waveguide silicon nitride (Si_3N_4) design that does not support acoustic confinement. The resulting high acoustic damping rate (by Eq. (1.13)) effectively suppresses pump phase noise enabling sub-Hz linewidth Stokes emissions that can be used in a variety of chip-scale photonic applications. Four system-on-chip applications are illustrated in Figure 1.3(b) – (e):

a chip scale atomic clock, an optical gyroscope, a coherent multi-terabit wavelength division multiplexed (WDM) transceiver, and a photonic microwave synthesizer.

This thesis describes the theoretical simulations, experimental results and the associated analysis of Brillouin gain spectrum in Si_3N_4/SiO_2 waveguides, and Brillouin laser power and (intensity, phase) noise dynamics. The demonstrated results of a low-phase noise microwave oscillator using the cascaded order Brillouin laser are presented. The possible applicability of the laser to realize the next generation Brillouin laser gyroscope is discussed along with the demonstrated results of Si_3N_4 waveguide coil based interferometric gyroscope.

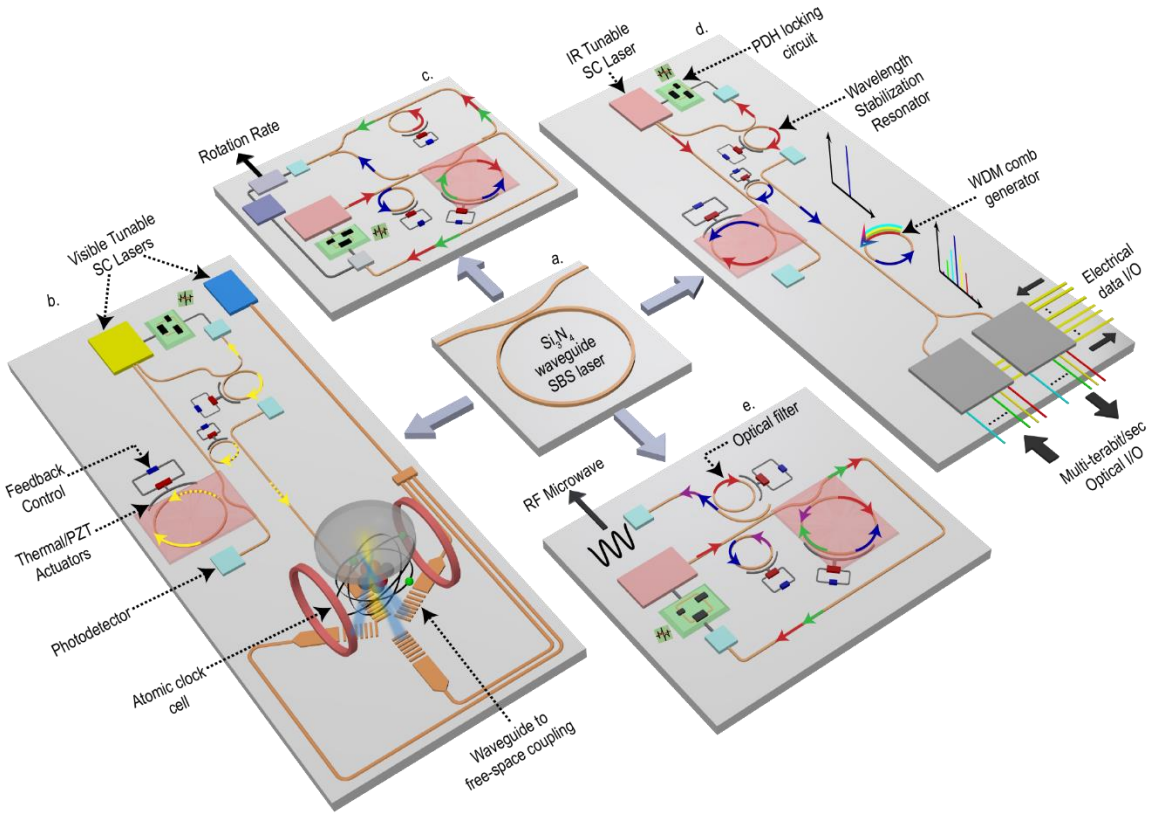

Figure 1.3. Silicon nitride waveguide Brillouin laser and application system-on-chip examples: *(a) Silicon nitride waveguide Brillouin laser resonator. (b) Chip scale atomic clock showing an atomic cell pumped probed by a visible Si_3N_4 waveguide Brillouin laser. (c) Integrated laser optical gyroscope to detect rotation rate based on Sagnac-induced phase shift between counter-propagating Stokes orders. (d) WDM multi terabit/sec coherent transceiver using an on-chip Si_3N_4 waveguide Brillouin laser pumped Si_3N_4 Kerr comb generator and a multi-channel integrated transceiver. (e) Low-noise chip-*

scale photonic microwave synthesizer that generates microwave frequencies by photo-mixing highly coherent optical Stokes orders from a cascaded-order Si_3N_4 waveguide Brillouin laser

1.6 Structure of the thesis and Contributions

The chapters comprising this dissertation and the contributors of each chapter are as follows. D.J.B. was the research and thesis advisor for this work. D.J.B., K.N., P.R., and M.S. supervised and led the scientific collaboration for all the Brillouin laser related work in this thesis. D.J.B and J.B. supervised the work related to waveguide coil based interferometric gyroscope in this thesis.

Chapter 2 presents an overview of Brillouin scattering theory and reviews the evolution of chip-scale Brillouin lasers. The integrated silicon nitride waveguide Brillouin laser is introduced as a solution to address the challenges related to their performance and manufacturability.

Chapter 3 describes the properties of waveguide materials and a theoretical simulation of Brillouin gain spectrum. The fabrication details of passive ULL Si_3N_4 waveguide spiral structures are discussed and the measured results of Brillouin gain spectrum are presented. ***Contributors:*** T.H. and J.N. contributed to the ULL Si_3N_4 waveguide spiral fabrication. R.B., P.R., M.P., T.Q., S.G., and K.N. contributed to the simulation and modeling of Brillouin gain spectrum. S.G., M.P., and J.W. independently measured the Brillouin gain spectrum.

Chapter 4 discusses the SBS laser resonator operating principles, design, and characterization. Techniques to characterize the cavity quality factor are described and the wafer-level yield of resonators based on the measured resonator Qs is evaluated. ***Contributors:*** M.P., S.G., P.R., R.B., J.N., K.N., M.S. and D.J.B. contributed to the laser resonator design. T.H., D.B., and J.N.

contributed to the laser resonator fabrication. S.G., G.B., C.P., and N.C. contributed to the laser resonator characterization.

Chapter 5 discusses the theory of power dynamics in single and cascaded order Brillouin lasers and includes the measured cascaded power dynamics in several of our Brillouin laser resonators. ***Contributors:*** R.B., N.O., P.R., S.G., and D.J.B. contributed to the development of theory for cascaded Brillouin laser power dynamics. S.G., measured the laser power dynamics of Brillouin laser resonator. S.G. and R.B., contributed to the analysis of laser power dynamics.

Chapter 6 discusses the theory of frequency and intensity noise dynamics of cascaded order Brillouin lasers and discusses the measured frequency and intensity noise dynamics. Includes demonstration of sub-Hz fundamental linewidth and -150 dBc/Hz RIN. ***Contributors:*** R.B., N.O., P.R., S.G., and D.J.B. contributed to the development of theory for cascaded Brillouin laser noise dynamics. S.G., and G.B., measured the laser noise dynamics of Brillouin laser resonator. S.G. and R.B., contributed to the analysis of laser noise dynamics.

Chapter 7 discusses the formulation of beat note linewidth between cascaded Stokes orders and demonstrates the phase noise results of photonic RF oscillator. ***Contributors:*** R.B., N.O., P.R., S.G., and D.J.B. contributed to the development of theory for beat note noise dynamics of a cascaded Brillouin laser. S.G., M.P., and J.W., measured the beat note noise dynamics of cascaded Brillouin laser. S.G. and R.B., contributed to the analysis of RF beat note noise dynamics.

Chapter 8 presents a comparative study of Brillouin laser gyroscopes vs conventional interferometric optical gyroscopes. The predicted performance of our Brillouin laser-based gyroscope will be discussed along with the demonstrated results of a 3-m silicon nitride

waveguide coil based interferometric optical gyroscope. ***Contributors:*** T.H., M.B., and S.G., contributed to the waveguide coil design for interferometric optical gyroscope and T.H., fabricated the waveguide coil. M.B., and S.G., contributed to the waveguide packaging. S.G., and M.B., contributed to the gyroscope characterization.

Chapter 9 summarizes the thesis and discusses possible directions for future work.

Chapter 2: Evolution of Chip-scale Brillouin Lasers

2.1 Abstract

Stimulated Brillouin scattering (SBS), is a third-order optical nonlinearity that is widely exploited in the development of a variety of photonic applications including low noise amplifiers, lasers, and photonic microwave filters and oscillators. Optical microcavities offer a solution to miniaturize SBS lasers to chip-scale without compromising on their degree of coherence. A majority of the high-performance micro-resonator cavities guide light in whispering gallery modes and have been realized in numerous geometric configurations including cylindrical, spherical, toroidal, and disc-shaped structures. While these discrete, tapered-fiber-coupled microcavity based SBS lasers are capable of sub-Hz emission, a CMOS compatible, monolithic integration of SBS lasers with this level of performance is yet to be realized. This chapter reviews the theoretical aspects of SBS necessary to develop the framework of narrow linewidth SBS lasers and presents an overview of the evolution of chip-scale SBS lasers. The issues related to noise performance, packaging and foundry-compatibility, yield and mass-manufacturability of these demonstrations are discussed. The prospect of addressing these challenges using integrated silicon nitride waveguide Brillouin laser is introduced.

2.2 Theory of Stimulated Brillouin Scattering

Brillouin scattering is a nonlinear optical process in which the light interacts coherently with acoustic waves. This optomechanical process of Brillouin photon-phonon coupling results from the annihilation of a high-frequency pump (angular frequency: ω_P, momentum: k_P) photon in to a travelling acoustic phonon (Ω, q) and a lower frequency Stokes photon (ω_S, k_S) or a

higher frequency anti-Stokes photon (ω_{aS}, k_{aS}), as shown in Figure 2.1(a,b). Since the population of phonons that can be absorbed is less than those that that a given material can emit, the energy transfer to a Stokes photon is way more efficient compared to the anti-Stokes photon. In systems where phase matching between these waves is satisfied, the energy and momentum of the participating waves is conserved (see Figure 2.1(c)), yielding

$$\left.\begin{aligned} \omega_P &= \Omega + \omega_S \\ k_P &= \mathrm{q} + k_S \end{aligned}\right\} \quad (2.1)$$

and results in efficient energy transfer from pump to Stokes mode.

The two key physical mechanisms that generate the acoustic phonons responsible for the coupling process are electrostriction and radiation pressure. Electrostriction is the compression or expansion of a material in the presence of an optical intensity gradient and results in variations of material density along the direction of optical propagation. Radiation pressure arises from forces induced by light scattering off the boundaries of the optical structure and results in the momentum exchange of light with the material boundaries having a discontinuous dielectric constant. Both these processes result in the formation of a density wave in the material. While electrostriction dominates the contribution to Brillouin coupling in optical fibers, radiation pressure becomes significant in high-confinement microscale structures, where the forces from light scattered off the nanoscale boundaries is non-negligible and often comparable to the electrostrictive forces[49]. The silicon nitride waveguides considered in this work have moderate index contrast but support extremely dilute optical modes due to the high-aspect ratio thin core waveguide geometry resulting in negligible Brillouin gain from radiation pressure.

The sequence of steps describing the creation of density wave and interaction of acoustic phonon with pump photon to generate a Stokes photon is conceptually illustrated in Figure 2.1(d). It is known that a standing-wave or a fringe pattern with periodic optical intensity fluctuations results from the interference of two counter-propagating optical waves with identical frequency. If the frequency of one of these interacting waves is slightly detuned from the other, a moving beat pattern is generated (see (ii) of Figure 2.1(d)). Through electrostriction or radiation pressure, this results in a traveling elastic density (acoustic) wave and a moving index grating (see (iii,iv) of Figure 2.1(d)) whose velocity depends on the frequency detuning between the participating optical waves. If the density wave velocity matches the velocity of sound of the material, the acoustic mode is resonantly amplified. This process enhances the transfer of energy from optical mode with higher frequency (pump) to Doppler-frequency shifted (Stokes), which in-turn, strengthens the beat pattern and sustains the traveling index grating, creating a cycle of opto-acoustic interaction. This is the conceptual basis for stimulated Brillouin lasing. The "detuned" counter-propagating wave in the SBS laser seeds from spontaneous Brillouin scattering due to thermally excited sound waves or (at low temperatures) by quantum noise (see (i) of Figure 2.1(d)). The transition from spontaneous to stimulated Brillouin scattering regimes is triggered at a specific optical intensity of the pump and is characterized by "threshold" pump power.

2.3 Acoustic Confinement and SBS Gain Spectrum

The strength and confinement regime of phonons into either longitudinal or transverse elastic modes determines the Brillouin Gain Spectrum (BGS) of the waveguide structure. The BGS of a structure represents and can be used to extract several key Brillouin scattering

parameters such as gain, frequency shift, and bandwidth which are inherently determined by the opto-acoustic properties of the material and waveguide structure.

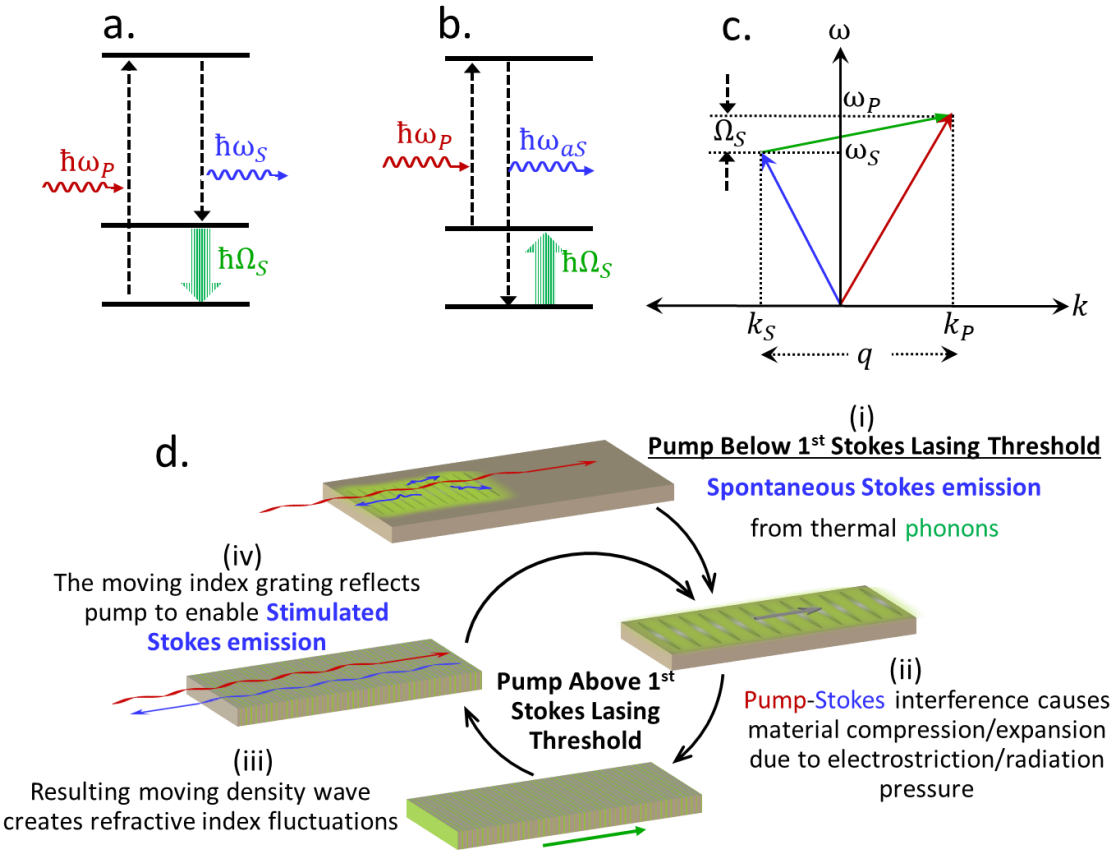

Figure 2.1. Conceptual Illustration of Brillouin Scattering: *(a,b) Energy level diagram of backward SBS showing annihilation of incident photon in to an acoustic phonon and a (a) Stokes photon or (b) anti-Stokes photon (c) Energy-momentum relations of photon-phonon coupling in Stokes Scattering process (d) Illustration of the physical mechanism that results in spontaneous and stimulated Brillouin scattering*

The Brillouin frequency shift ν_B for backward SBS (BSBS) changes with the composition of the material and the wavelength of incident optical pump λ_P $\left(=\left(\frac{2\pi c}{\omega_P}\right)\right)$ and is expressed as

$$\nu_B = \frac{\Omega}{2\pi} = \frac{qV_a}{2\pi} \approx \frac{2k_P V_a}{2\pi} = \frac{2\left(\frac{2\pi n}{\lambda_P}\right)V_a}{2\pi} = \frac{2nV_a}{\lambda_P} \qquad (2.2)$$

where V_a represents either the elastic longitudinal (V_L) or shear (V_S) acoustic velocity and n is the optical refractive index of the material. The acoustic velocities are related to the mechanical properties of the material: density (ρ), Young's modulus (E), Poisson's ratio (μ) as

$$\left.\begin{aligned} V_L &= \sqrt{\frac{E(1-\mu)}{\rho(1+\mu)(1-2\mu)}} \\ V_S &= \sqrt{\frac{E}{2\rho(1+\mu)}} \end{aligned}\right\} \quad (2.2)$$

The phonon guiding, and confinement depends on the sound velocity (V_a) and (specific) acoustic impedance ($Z = \rho V_a$) contrast between optical core and cladding of the waveguide. In an embedded waveguide structure (see Figure 2.2(a)), phonon guiding through total internal reflection (TIR) requires a slower acoustic mode in the core compared to the cladding. This is the operating regime for optical waveguides with softer cores (low E) such as chalcogenide waveguide structures.

For waveguides with cores supporting faster acoustic velocities than the cladding, phonons can still be confined to the core and guided if a very high core-cladding acoustic velocity contrast exists. The confinement and guiding do not result from TIR but occur due to the very long leakage time resulting from the huge impedance contrast at the interface and this principle is employed in silica[46] or crystalline[16] SBS micro-resonators. These two cases result in a phonon guiding profile like the one illustrated in Figure 2.2(b). The long mean photon life time results in a mean-phonon decay path length (L_A) comparable to photon decay length (L_O) due to the large opto-acoustic mode overlap leading to increased peak gain and narrow bandwidth of Brillouin gain spectrum ($\Delta\nu_B$), as illustrated in Figure 2.2(c). For waveguides with moderate acoustic velocity contrast, the phonons couple into radiating acoustic modes or a free-space continuum of leaky acoustic modes that quickly diffract away from the core into

the cladding, as shown in Figure 2.2(d). This process decreases the average phonon lifetime and decreases the Brillouin gain while broadening the gain spectrum, as shown in Figure 2.2(e). ***While the reduction in gain impedes the pump-Stokes conversion efficiency, this property plays an important role in suppression of noise transfer from pump to Stokes orders and is one of the key characteristics of the silicon nitride waveguide Brillouin laser, and is detailed in later chapters.***

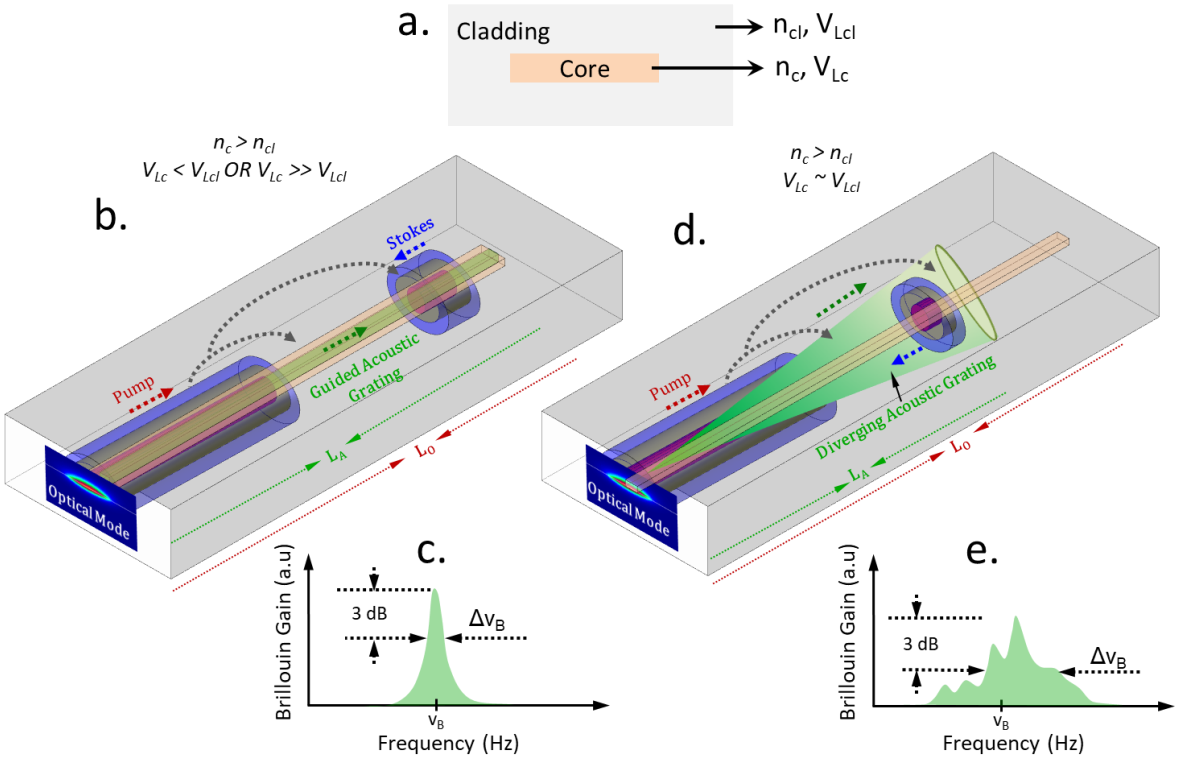

Figure 2.2. Illustration of Acoustic Confinement Regimes: *(a)Cross-section of a rectangular embedded waveguide showing optical and acoustic parameters (b-e) Illustration of acoustic phonon grating and associated BGS in embedded waveguides that (b,c) support acoustic confinement and (d,e) do not support acoustic confinement*

Over the years, several theoretical frameworks have been developed to estimate the SBS gain contribution realizable in waveguides that operate in these phonon-coupling regimes. Conventionally, the evaluation of Brillouin gain considered the density fluctuations forming

the elastic acoustic wave as a scalar quantity and the light waves to be linearly polarized. While such treatment yields reasonable accuracy for large structures like optical fibers, a more generic treatment is needed for nanoscale structures to account for the full-vectorial nature of the forces contributing to the Brillouin gain. Such a framework, proposed in [49], uses the optical mode of the waveguide to simulate the photo-elastic generation of the associated acoustic wave, and evaluate the acousto-optic overlap and hence the Brillouin gain.

The frequency-dependent SBS gain, g(Ω) experienced by the Stokes wave[50] is calculated by parametrically sweeping the acoustic frequency Ω across the analytically predicted phase-matched frequency as

$$g(\Omega) = \frac{\omega_S}{2\Omega P_S P_P} \operatorname{Re}\left\langle f \cdot \frac{du}{dt} \right\rangle \qquad (2.3)$$

where $P_p(P_S)$ is the optical pump (Stokes) power, and u describes the elastic deformation of the waveguide induced by the optical forces f generated by the pump and the Stokes. A detailed discussion and the mathematical treatment of framework for evaluation of Brillouin gain spectrum described in Eq. (2.3) can be found in P.T.Rakich et. al.[50].The quantity $\left\langle f \cdot \frac{du}{dt} \right\rangle$ represents the opto-acoustic mode overlap integral over the waveguide cross-section. Thus, the realizable peak SBS gain increases with small waveguide cross-section due to large overlap of photon-phonon modes and is one of the key factors that led to the development of miniaturized, chip-scale Brillouin lasers.

2.4 Chip-scale Brillouin Lasers

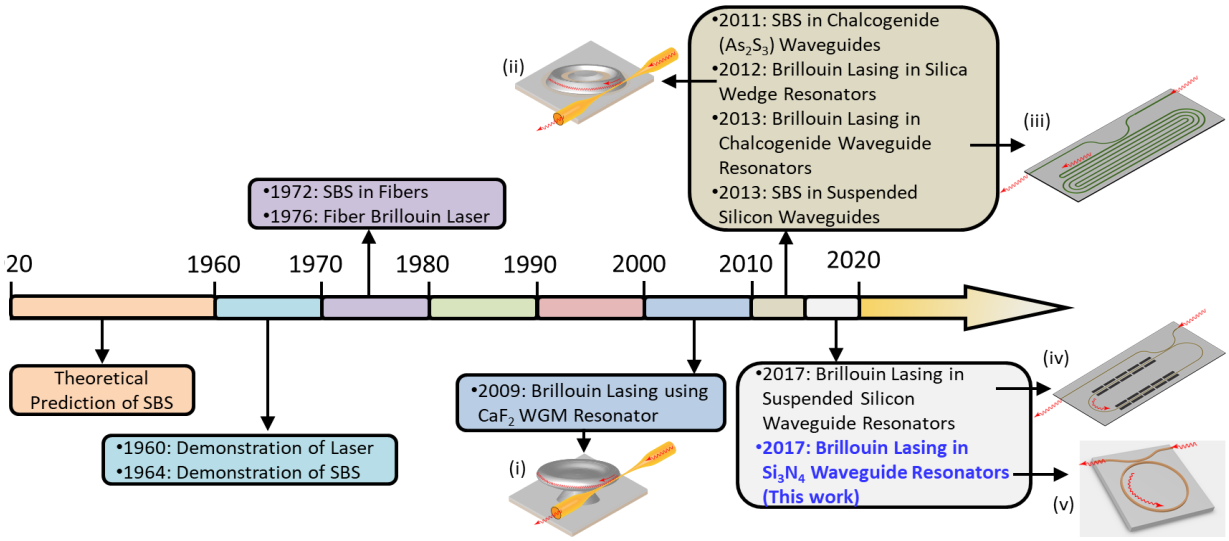

Figure 2.3. Key Milestones in the Development of Chip-scale Brillouin Lasers: *Timeline showing the progress towards integrated Brillouin lasers. Also shown are artistic illustrations of the optical microcavity geometries employed in each of these demonstrations: Tapered fiber coupled (i) Crystalline CaF_2 whispering-gallery mode resonator[16] (ii) Chemically etched silica wedge microresonator[46] and Fiber to waveguide bus-coupled (iii) Chalcogenide[47] (iv) Suspended silicon waveguide[48] (v) Silicon nitride waveguide[51,52] resonators*

Figure 2.3 illustrates the timeline of major advances in the realization of chip-scale SBS lasers. The theoretical predictions of an inelastic scattering of light from acoustic phonons were made by Brillouin[53] and Mandelstam[54] as early as 1920s. Due to the intensity dependent nature of the Brillouin nonlinearity and its narrow spectral bandwidth, the empirical realization of SBS was impeded by the stringent requirement of high power, relatively narrow linewidth light sources. Four decades later, the first observation of SBS in bulk media was made by Chiao et. al[55] in 1964, shortly after demonstration of the first generation of the laser[56] in 1960. Realization of narrow-linewidth SBS lasers was catapulted by the advent of low-loss optical fibers. Following the demonstration of SBS in fibers in 1972 by Ippen et. al[57], K.O.Hill et. al.[58] demonstrated the first CW fiber Brillouin laser in 1976. However, miniaturization of high quality factor optical cavities did not gather pace till the late 2000s.

The development of ultra-high Q crystalline fluoride whispering gallery mode (WGM) microresonator cavities led to the first demonstration of a chip-scale Brillouin laser in 2009[16]. From 2011, several other material systems and waveguide geometries were employed to demonstrate chip-scale Brillouin lasing that included silica wedge resonators[46], chalcogenide [47,59] and suspended silicon waveguides[48,50]. Each of these platforms employ unique waveguide geometries that aid in large photon and phonon confinement and determine the Brillouin gain spectrum, linewidth narrowing properties. The properties of these optical cavities using different material systems to realize narrow linewidth SBS lasers are summarized in Figure 2.4. While discrete tapered fiber coupled microcavity Brillouin lasers are capable of sub-Hz fundamental linewidth emission[15], the path to monolithic integration of these lasers has remained elusive. Also, compact, low linewidth SBS lasers demonstrated using etched-silica microdisk[46] and fluoride[16] resonators present significant challenges with respect to stability, sensitivity to environment conditions, operation across wide wavelength ranges, and incompatible with low cost wafer-scale integration and packaging processes. In addition, microdisk based designs present challenges related to their multiple polarization modes and phonon confinement, bus-resonator coupling, dispersion engineering, and photon-phonon phase matching and air interfaces.

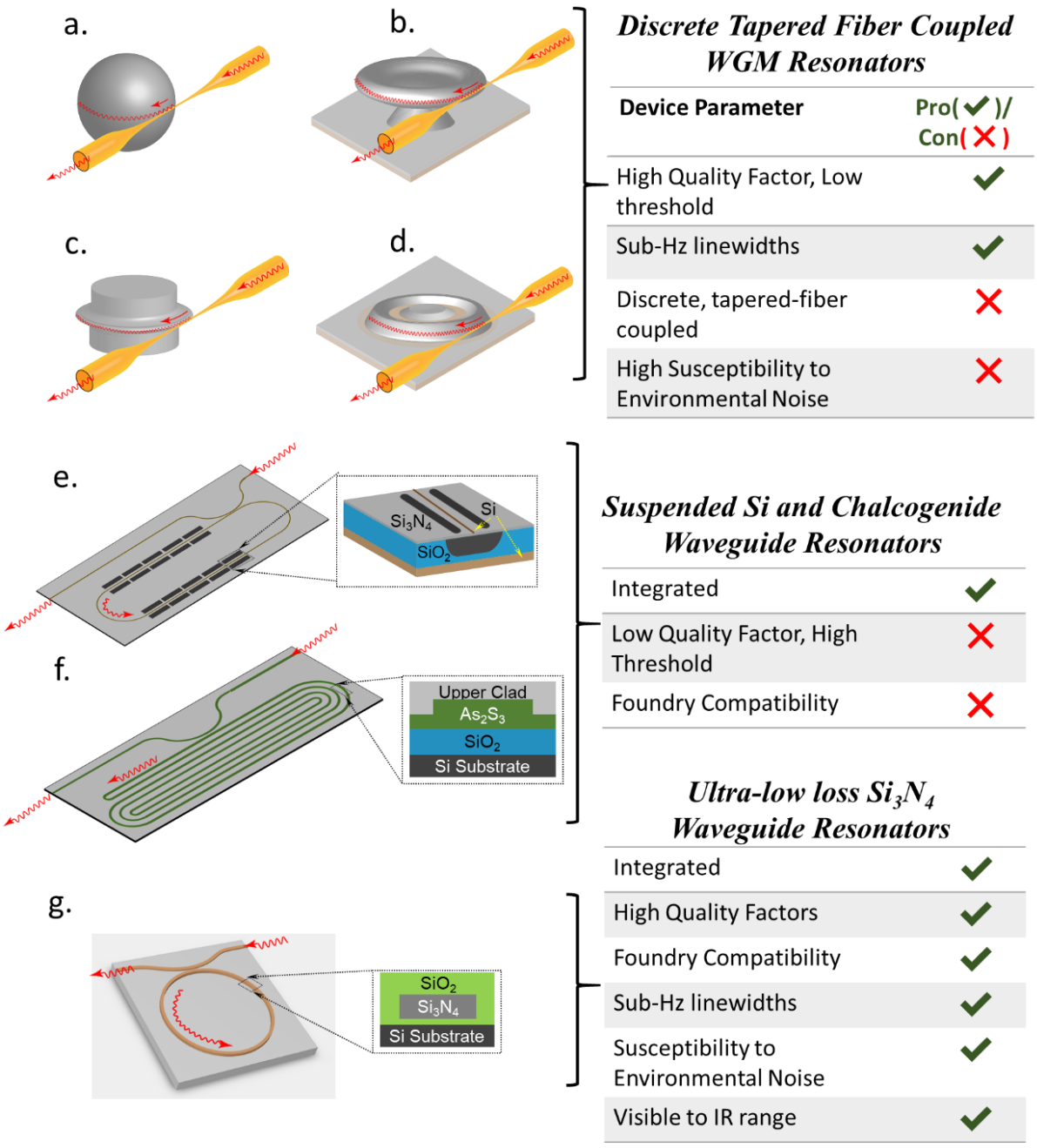

Figure 2.4. Illustration and characteristics of chip-scale optical microcavities for narrow-linewidth SBS laser systems: *Discrete tapered fiber coupled (silica/crystalline) (a) spherical*[60] *(b) toroidal*[44,61,62] *(c) rod*[16,63] *(d) chemically etched wedge WGM micro-resonators*[46] *(e) Nanoscale suspended silicon slot waveguide resonators*[48,50,64] *(f) Buried chalcogenide waveguide resonators*[47] *(g)Ultra-low loss Si_3N_4 waveguide high Q resonators*[51,65,66]

Realization of Brillouin lasing in a monolithically integrated silicon nitride waveguide platform can potentially overcome these issues and open the door for an array of future

photonic systems. Silicon nitride as a waveguide platform[67] has significantly risen to importance as an alternative to high loss silicon and InP platforms for monolithic integration of passive photonic devices. The development of ultra-low loss silicon nitride waveguides and high Q integrated silicon nitride waveguide resonators at University of California, Santa Barbara has led to this thesis work of realizing of monolithically integrated SBS laser in the ULL platform.

2.5 Summary

This chapter presented an overview of SBS theory and discussed the timeline of advances in of chip-scale Brillouin lasers. The opto-acoustic material properties that determine the acoustic confinement and phonon coupling regimes are discussed and the framework to evaluate Brillouin gain spectrum is introduced. The material systems, optical cavity geometry, and performance limitations of the state-of-the art chip-scale Brillouin lasers are discussed. The integrated silicon nitride waveguide Brillouin laser is introduced as a solution to address the challenges related to their performance and mass manufacturability.

Chapter 3: Brillouin Scattering in Silicon Nitride Waveguides

3.1 Abstract

In this chapter, the results of the first observation of Brillouin scattering in ULL Si_3N_4 waveguides are presented. The waveguide fabrication process is discussed, and the results of optical propagation loss and group index obtained through optical back-scatter reflectometry (OBR) are shown. The acousto-optic properties of ULL Si_3N_4 waveguide structures are obtained through thin film material analysis. The Brillouin gain spectrum (BGS) of the waveguides is evaluated by plugging these material properties into the stimulated Brillouin scattering (SBS) framework discussed in section 2.3. The experimental results of the BGS obtained using passive Si_3N_4 waveguide spirals are presented and compared to the simulated spectrum. The thermal dependence of the BGS on the properties of the upper oxide cladding is evaluated by measuring the BGS for waveguides with two different upper PECVD (Plasma Enhanced Chemical Vapor Deposition) oxide cladding variants (silane and TEOS based). Knowledge of the Brillouin gain spectrum of passive waveguide structures is essential to realize SBS laser resonator structures.

3.2 Waveguide Fabrication

The fabrication process flow for Si_3N_4/SiO_2 waveguides used in this work (as reported in Huffman. et. al[66]) is shown in Figure 3.1. A 40 nm thick stoichiometric silicon nitride film was deposited using LPCVD on a 4-inch silicon wafer with a 15 µm thermally grown oxide. The wafer was spun with standard DUV anti-reflective (AR) and photoresist layers and then patterned using an ASML PAS 5500/300 DUV stepper. The AR coating was etched with a

RIE PlasmaTherm etch tool. The resist was used as an etch mask to realize high aspect ratio waveguide core by anisotropically dry-etching the silicon nitride film in a Panasonic E640 ICP etcher in a $CHF_3/CF_4/O_2$ chemistry. The resulting byproducts from this etch were then ashed with a Panasonic E626I ICP tool in an O_2 atmosphere before stripping the resist by sonicating in a hot NMP solution and rinsing in Iso-propanol. The AR coating and other organic impurities were then removed by dipping the wafer in a freshly prepared, standard piranha solution heated at 100 °C. The wafer was inspected by dark-field microscopy for undesired particles near the waveguide core at both post-develop and post-etch stages and additional sonication in hot NMP solution and rinse in iso-propanol were performed if required. An additional plasma clean using a Gasonics Aura 2000-LL Downstream asher tool helped us get rid of any leftover resist and other organic materials. The device features were inspected with a JEOL 7600F FE-SEM and the RMS sidewall roughness was measured using Dimension 3100 AFM to be lower than 3 nm. A 6 µm thick oxide was deposited using plasma enhanced chemical vapor deposition with TEOS as a silicon precursor followed by a two-step anneal at 1050 °C for 7 hours, and 1150 °C for 2 hours and was diced in to individual devices.

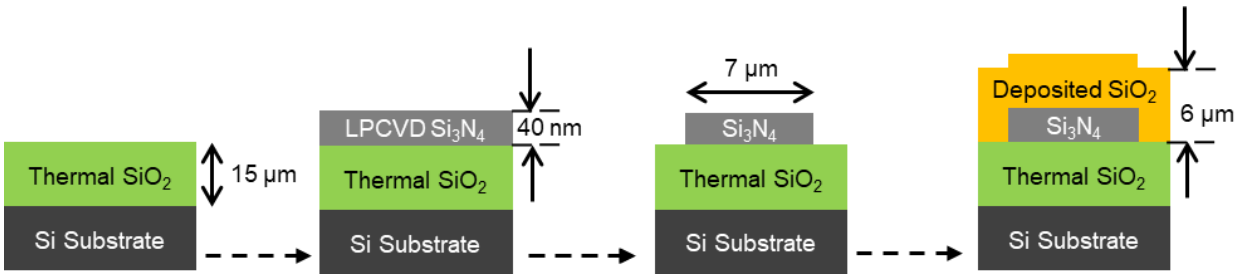

Figure 3.1. Ultra-low loss silicon nitride waveguide fabrication process flow: *Silicon nitride waveguides are realized by performing DUV lithography and dry etch steps on a 4-inch silicon wafers which have pre-deposited 15µm thermally grown wet oxide and 40 nm stoichiometric LPCVD nitride films. The waveguides are capped with 6 µm TEOS PECVD oxide that serves as upper cladding*

3.3 Optical Propagation Loss and Group Index Characterization

The optical propagation loss and group index of a 5 m waveguide spiral with input and output waveguides were characterized using a Luna OBR system (setup shown in Figure 3.2). The S-bend spiral consists of 42 turns stitched between four DUV masks. (168 stitches in total) and has a minimum radius of 11.83 mm. The group index was measured to be 1.478 and propagation loss of the spiral was 1.14 dB/m at 1550 nm.

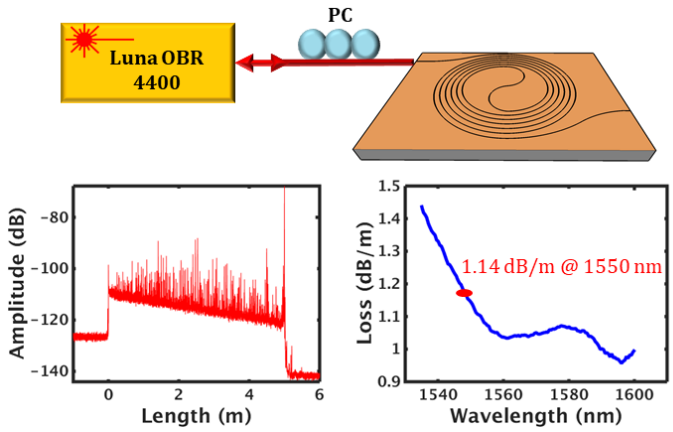

Figure 3.2. Measurement of Optical Propagation Loss Using Optical Back Scatter Reflectometry: *Slope of Rayleigh backscattered signal from the spiral for different wavelengths is used to estimate the optical propagation loss*

3.4 Thin Film Material Analysis

The refractive index, material density, and Young's modulus of thermally grown oxide, LPCVD Si_3N_4, and PECVD SiO_2 were measured using optical ellipsometry, X-ray reflectometry (XRR), and nano-indentation techniques respectively using thin-films deposited on 4-inch silicon wafers. The measured material properties of the waveguide layers listed in Table 3.1 agree well with the values in literature[68,69]. While the refractive index gradient between core (Si_3N_4) and cladding (SiO_2) allows optical guiding ($n_{core} > n_{clad}$), the extracted

sound velocities indicate that the waveguide does not support acoustic confinement and guiding[70] (see section 2.3). However, the optical mode-fields in our waveguide can produce substantial Brillouin gain due to a large spatial overlap between the dilute optical mode and the unguided, leaky acoustic modes.

Table 3.1: Optical and mechanical properties of waveguide layers: *Refractive index (n), stoichiometry, material density (ρ), and mean reduced Young's modulus (Y) were determined using optical ellipsometry, Rutherford backscatter spectroscopy, X-ray reflectivity, and nano-indentation techniques respectively. Longitudinal (V_L) and shear (V_S) acoustic velocities were extracted from the measured values assuming a Poisson ratio of 0.17 for thermal SiO_2, 0.25 for deposited SiO_2, and 0.23 for Si_3N_4. (*: ρ of TEOS oxide was not characterized; ρ = 2300 Kg/m^3 was used to estimate V_L, V_S)*

Film	**n**	**Stoichiometry**	**ρ (Kg/m^3)**	**$\bar{Y}$ (GPa)**	**V_L (m/s)**	**V_S (m/s)**
SiH_4 based PECVD SiO_2	1.459	Si:O ~ 0.5	2290	91	6904	5637
Thermally grown wet oxide	1.444	Si:O ~ 0.5	2240	74	5959	5314
LPCVD Si_3N_4	1.936	Si:N ~ 0.724	3020	201	8774	7348
TEOS based PECVD SiO_2	1.452	Si:O ~ 0.5	-	78	6378*	5207*

3.5 Simulation of Brillouin Gain Spectrum

Utilizing the parameters evaluated from material analysis of oxide and nitride thin films, the position, shape, and amplitude of the SBS gain spectrum of our waveguides was theoretically predicted. To do this, a fully three-dimensional finite element method (FEM) model of the waveguide was constructed to study the acousto-optic behavior. The 3-D simulation model was setup with periodic boundary conditions at waveguide facets and perfectly matched layers (optical and acoustic) in the transverse plane to inhibit back-reflections as shown in Figure 3.3(a). Using COMSOL finite element solver, the optical mode-field E_P (E_S) supported by the structure at the pump (Stokes) frequency ω_P (ω_S) (example cross section shown in Figure 3.3(b) with simulated effective optical mode, A_{eff} area was ~28 μm^2)

was simulated. These simulated fields were used to find the photoelastic force density that drives the acoustic waves. The cross sections of the total photoelastic force field *f* induced by (E_P, E_S) and acoustic displacement field *u* of the elastic mode driven by *f* at the phase matching frequency, $\omega_P - \omega_S \sim (2\pi n_{eff} V_a/\lambda_P)$ are shown in Figure 3.3(c,d). The simulated gain spectrum (gain g_B per effective area A_{eff}, $\left(\frac{g_B}{A_{eff}}\right)$ in $m^{-1}W^{-1}$) as shown in Figure 3.3(g) using Eq. (2.3) shows a gain peak at $\nu_B \sim 10.9$ GHz. This frequency shift for peak gain, as expected, is close to that of silica since nearly the entire optical mode lies in the cladding material.

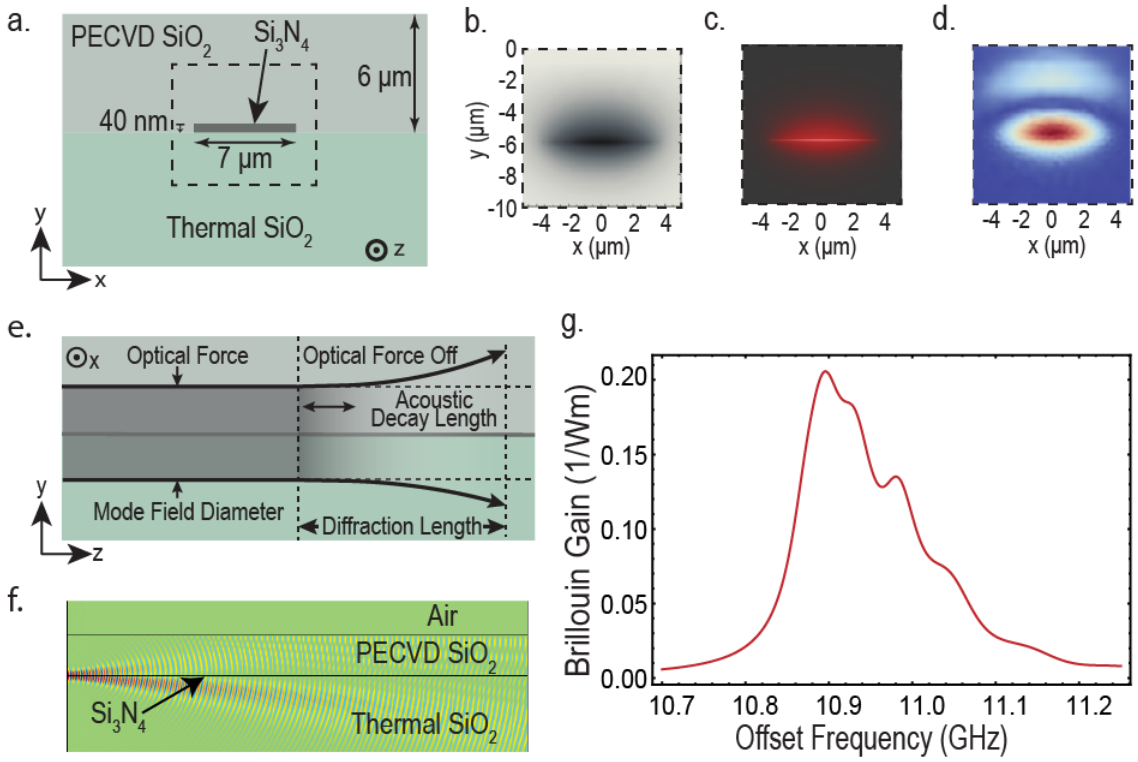

Figure 3.3. Calibrated Brillouin gain simulations: *(a) Waveguide structure used for finite-element method simulations; (b) Simulated TE-like dilute optical mode of waveguide structure; (c) Resulting optical force field; (d) Generated acoustic displacement field (e) Concept of acoustic divergence due to lack of acoustic confinement; (f) Simulated acoustic mode experiencing acoustic dampening as it diverges in to the cladding; (g) Simulated Brillouin gain spectrum with fundamental acoustic mode at around 10.9 GHz and spectral broadening at high frequencies*

Due to the lack of acoustic confinement, the generated sound waves diffract away from the waveguide core as they propagate (conceptually illustrated in Figure 2.2(d), Figure 3.3(e)).

The BGS exhibits a high degree of skewness toward higher frequencies since the acoustic waves to couple into a portion of the free-space continuum in silica cladding. The predicted degree of broadening is consistent with the value estimated through observation of the angle of divergence of a single acoustic wavelet. The simulated divergence of the generated acoustic beam in the direction of propagation over a single guided optical wavelength can be seen in Figure 3.3(f). Asymmetry in divergence is due to the different acoustic velocities of the cladding oxides. Since the optical mode field is much larger than the acoustic wavelength, the acoustic diffraction length (Rayleigh range) is much larger than the phonon mean-free path (~ 30 μm). The short acoustic mean-free path results from the large aperture optical mode driven acoustic field combined with the acoustic dampening properties of the oxide cladding. Therefore, the rate of acoustic leakage due to diffraction is much smaller than the decay rate due to intrinsic acoustic absorption in the surrounding oxide.

3.6 Brillouin Gain Spectrum Measurements

We determined the BGS of the fabricated ultra-low loss Si_3N_4 coils using a standard pump probe technique[71] (see setup shown in Figure 3.4(a)). Two stable, tunable fiber (NP Photonics) lasers were directed into a temperature stabilized 5 m long segment of waveguide from opposite ends. The silica fiber pigtail of the circulator that couples pump laser in to waveguide spiral was shortened and spliced to a segment of a highly nonlinear single mode Nufern UHNA3 fiber which has a Brillouin gain peak spectrally isolated from our waveguide. This minimized the contribution of probe gain within silica fiber whose gain spectrum is very close to Si_3N_4 waveguides used in this work. The pump was amplified with an erbium-doped fiber amplifier and the difference in optical frequency between the two lasers was swept through the simulated frequency of the SBS gain peak. The beat note between the pump and

probe was monitored by combining the two and monitoring the signal they generated in an electrical spectrum analyzer. As the pump and probe beams propagated counter to each other within the waveguide, the pump contributed gain to the probe based on the frequency-dependent value of the SBS gain coefficient.

The probe gain was measured for the 5 m waveguide spiral with TEOS PECVD oxide upper cladding for on-chip pump powers varying from about 200 mW to 600 mW as the pump laser frequency was tuned to vary the spacing between the two lasers from about 10.7 GHz to 11.1 GHz (see Figure 3.4(c)). The maximum probe gain was plotted as a function of on-chip pump power and the peak SBS gain coefficient over the effective spiral length was extracted by performing a numerical fit of the data.

The loss coefficient of the spiral, extracted using optical backscatter reflectometry to be 1.14 dB/m, was used to calculate the effective length of spiral as 2.7843 m. Using this data, the peak SBS gain coefficient is $0.10 \pm .009$ $m^{-1}W^{-1}$ (see Figure 3.4(d)) which is close to the simulated value. Similar measurement made using 3-m spiral with silane PECVD oxide upper cladding showed lower gain due to shorter length and higher loss (see Figure 3.4(b)). The frequency shift at peak Brillouin gain for silane PECVD oxide clad spiral was found to be 11.09 GHz slightly higher than that of SMF and TEOS PECVD oxide clad spiral. This difference can be explained by examining the material properties in Table 3.1. The index and acoustic velocity of TEOS PECVD oxide cladding was found to be closer to silica (thermal oxide) compared to the silane PECVD variant.

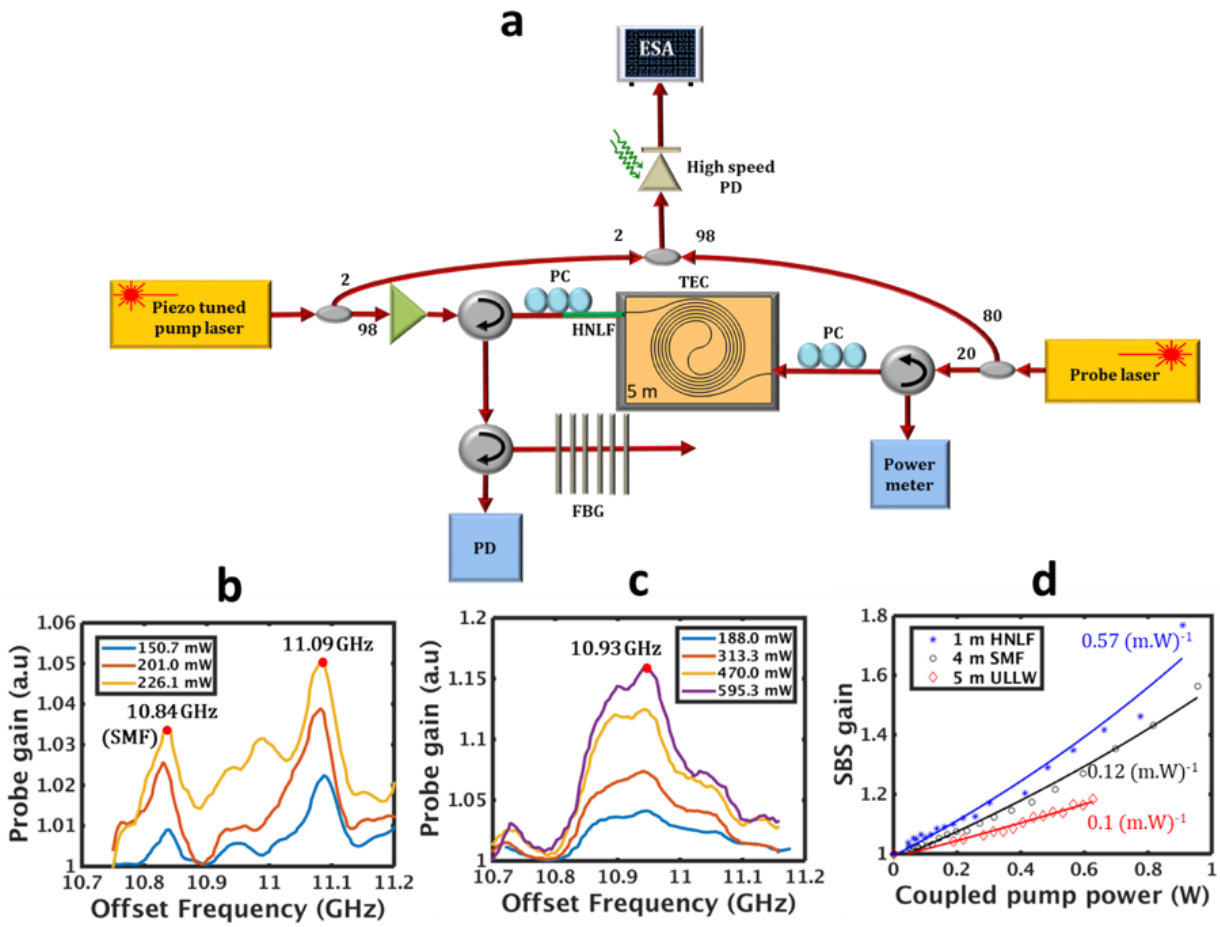

Figure 3.4. Brillouin gain measurements using pump-probe technique: *(a) Experimental setup to measure Brilluoin gain spectrum of Si_3N_4 waveguides; (b) Brillouin gain observed in 3-m Si_3N_4 waveguide spiral with SiH_4 PECVD oxide upper cladding with a gain peak at 11.09 GHz. (c) Brillouin gain observed in 5-m Si3N4 waveguide spiral with TEOS PECVD oxide upper cladding with a gain peak at 10.93 GHz. TEOS oxide cladding was used for fabricating Brillouin laser resonators. (d) Comparison of SBS gain coefficient (g_B /A_{eff}) in Si_3N_4 waveguides (TEOS clad) with SMF-28 fiber and highly non-linear fiber (HNLF: Nufern UHNA3)*

To confirm the accuracy of the measurement technique, the BGS measurements were performed using 1 m UHNA3 and 5 m single-mode fibers as well and the estimated peak Brillouin gain is in accordance with the expected value (see Figure 3.4(d)). The results gave us confidence in the accuracy of our theoretical methods (see Figure 3.5) for SBS gain calculation and provided us inputs to design a Brillouin ring laser resonator.

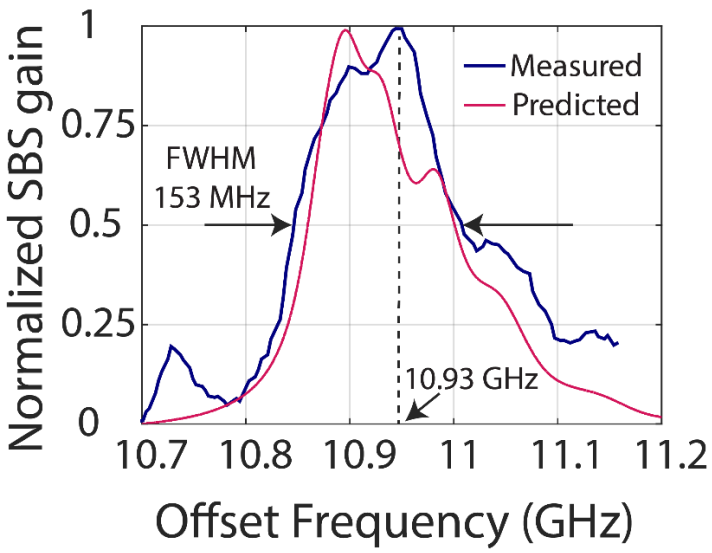

Figure 3.5. Agreement between predicted and measured BGS: *The measured and predicted Brillouin gain spectra for TEOS oxide upper cladding showed decent agreement. The slight difference between the traces is attributed to the variations in the material parameters compared to the ones shown in Table 3.1.*

3.7 Thermal Dependence of Brillouin Gain Spectrum

The shift in Brillouin gain spectrum with varying temperature was measured for SiH_4 oxide and TEOS oxide clad waveguides using a temperature-controlled stage. The observed shift in gain offset frequency for SiH_4 oxide-based waveguides was 1.2 MHz/C (see) which was slightly lower than TEOS oxide clad waveguides at 2 MHz/C (see Figure 3.6). The measured values agree with the thermal shift of offset frequency observed in silica fibers[72].

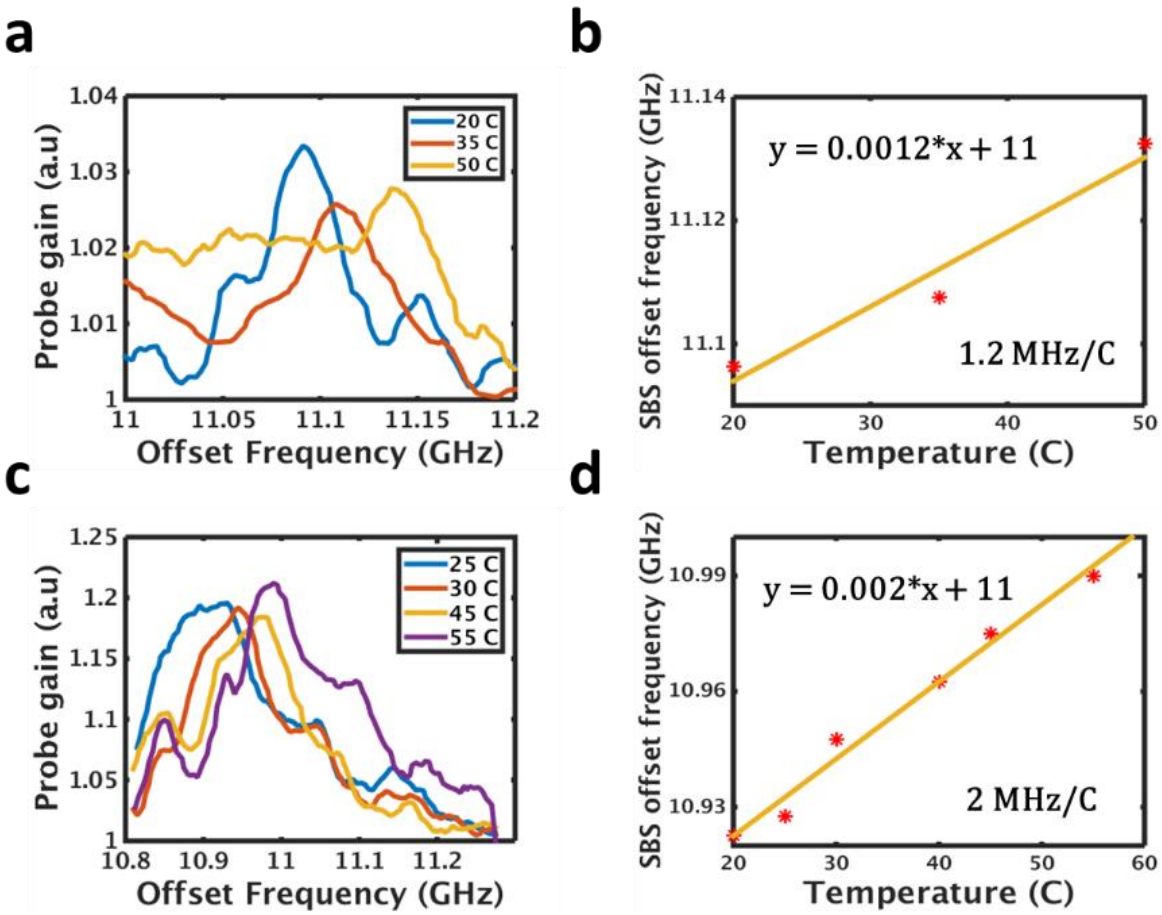

Figure 3.6. Thermal dependence of Brillouin gain (SBS) offset frequency: *(a, b): Measurement of SBS offset frequency variation in a 3-m Si_3N_4 waveguide spiral with SiH_4 PECVD oxide upper cladding with increasing temperature yields 1.2 MHz/C. (c, d): Measurement of SBS offset frequency variation in a 5-m Si3N4 spiral with TEOS PECVD oxide upper cladding with increasing temperature yields 2 MHz/C*

3.8 Summary

This chapter detailed the fabrication process of passive ULL Si_3N_4 waveguide spiral structures and presented the measured results of Brillouin gain spectrum (Peak gain $\left(\frac{g_B}{A_{eff}}\right)$ ~ 0.1 $m^{-1}W^{-1}$ at ν_B = 10.92 GHz). These BGS measurements provide the necessary information for designing SBS laser resonator and will be described in the next chapter.

Chapter 4: SBS Laser Resonator Design and Characterization

4.1 Abstract

This chapter describes the design and characterization of silicon nitride waveguide SBS laser resonator. The resonator length is chosen to match the peak gain frequency of measured BGS of passive waveguide structures (described in the previous chapter) and power coupling coefficient is chosen to maximize quality factor of the resonator to lower the lasing threshold. Measurement results of resonator cavity parameters using calibrated MZI and ring-down techniques are described, and the wafer-level yield of resonators is analyzed based on the measured resonator Qs.

4.2 Resonator Design

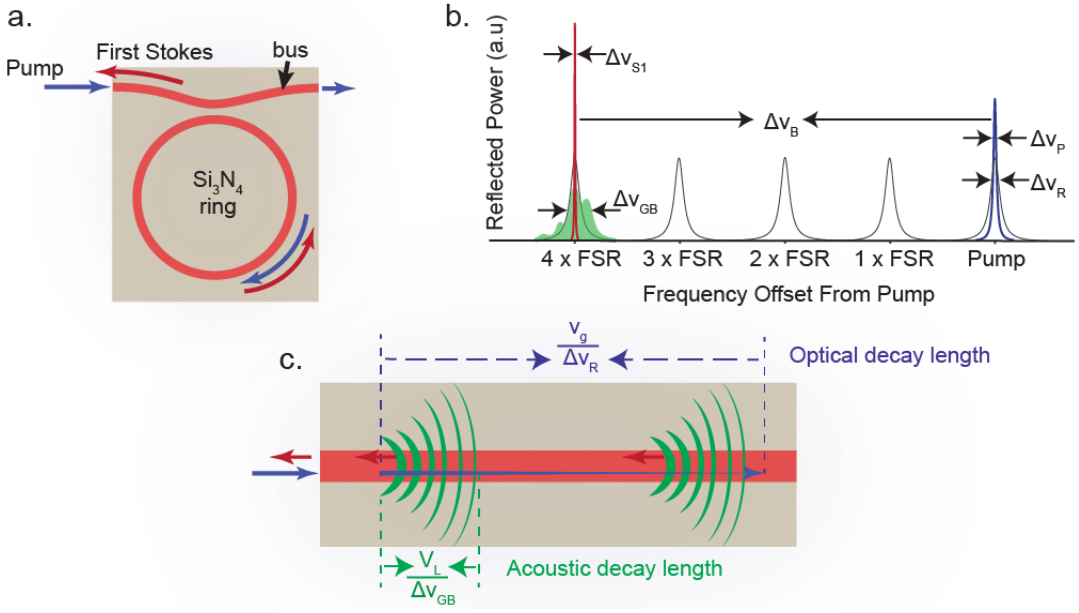

Figure 4.1. Brillouin laser optical guiding, phonon generation, and resonant gain: *(a) Generation of first Stokes order in a Si_3N_4 waveguide Brillouin laser. (b) Resonator reflection spectra and the FSR (black), broadened Brillouin gain spectra (green), input pump signal*

(blue) and generated first Stokes order (red) (c) Illustration of unguided phonons in a high Q optical resonator. The longer optical photon life time facilitates continuous creation of phonons.

This section describes the laser resonator design as reported in the work of Huffman et. al[66].The long optical waveguide resonator, where ν_B spans multiple FSRs, relaxes the fabrication precision required to phase match the optical and acoustic fields and yields an advantage over low mode-volume single FSR microdisk designs. This large cavity is used to store many photons required to reduce the fundamental linewidth (Eq. 1.5).

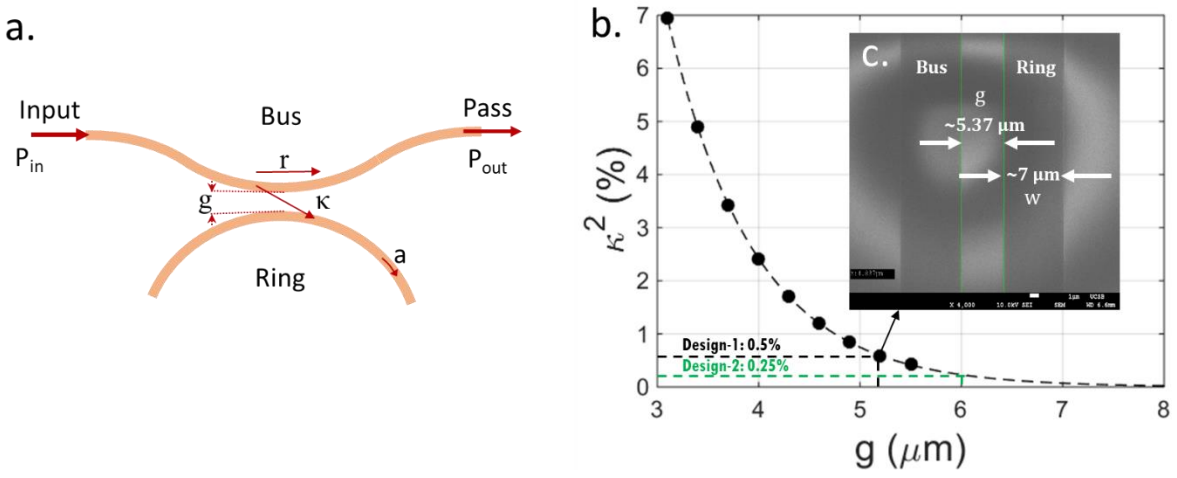

Figure 4.2. Directional Coupler Design for SBS Laser Resonator *(a) Schematic of ring-bus interface of laser resonator showing key resonator parameters: loss coefficient a, coupling gap g, and self and cross coupling coefficients r and κ, input and output powers P_{in} and P_{out} (b) Simulated values of coupling gap g vs power coupling coefficient κ^2 and chosen design values of coupling coefficient: 0.5% (design-1) and 0.25% (design-2) (c) SEM of bus-ring gap of a fabricated resonator with coupling gap of 5.37 µm with a design coupling coefficient of 0.5%.*

In order to realize high Q resonators, we used test structures to calibrate simulated coupling coefficients of fabricated couplers. Simulation of the coupling coefficient as a function of ring-bus gap was performed using PhoeniX Software's Optodesigner and is shown Figure 4.2(b). Resonators with gap values of 5.42 µm and 6.00 µm correspond to the simulated coupling coefficients of 0.5% and 0.25% respectively and are indicated as "Design-1" and "Design-2" in Figure 4.2(b). Measured values of these test structures returned coupling

coefficients of 1.14% and 0.88% for gap values of 5.42 µm and 6.00 µm. The difference between the calibrated and measured power coupling coefficients may be attributed to the minute fabrication process variations related to waveguide width and core thickness. The radius of the resonator designs 1 and 2 were chosen to be 11.83 mm and 11.803 mm respectively to achieve the Brillouin phase matching criterion by meeting 4xFSR ~ Brillouin frequency offset corresponding to peak gain.

4.3 Resonator Characterization

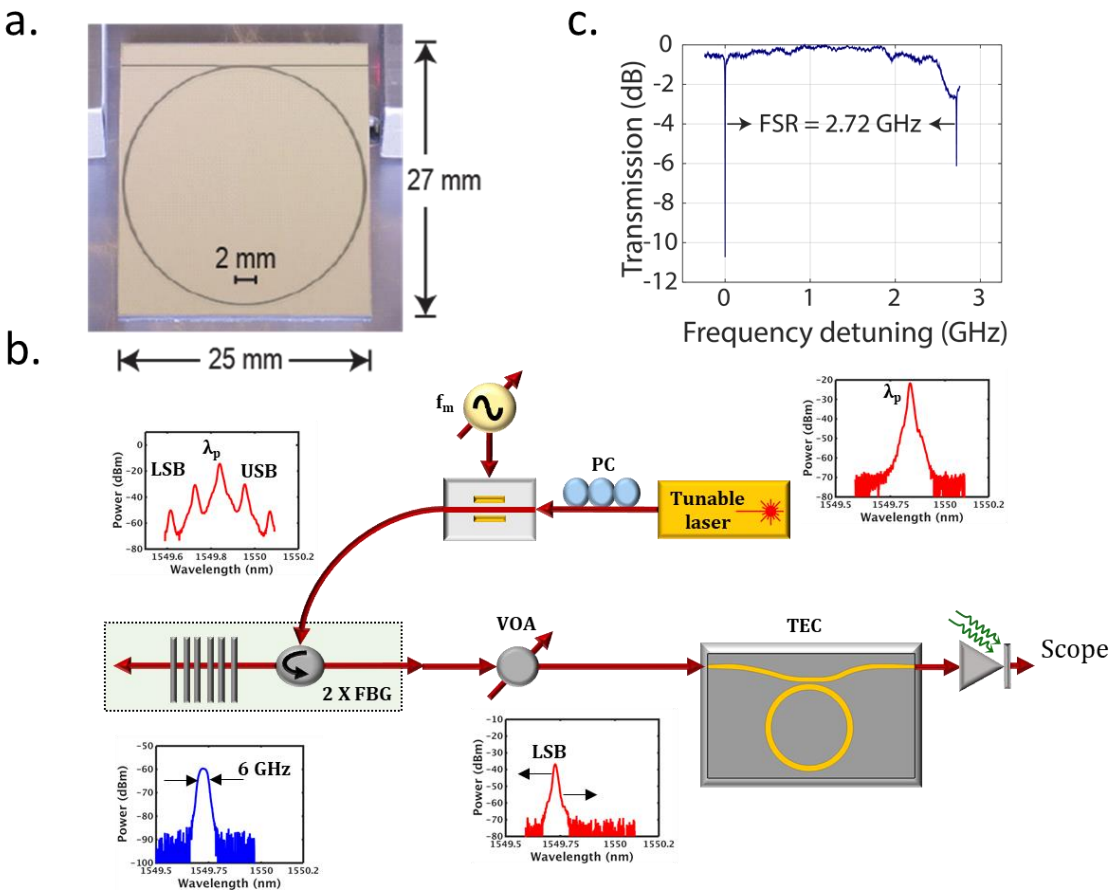

Figure 4.3. FSR characterization of ULL Si_3N_4 resonator using single side-band swept source: *(a) Contrast enhanced photograph of 27 mm X 25 mm silicon nitride laser chip. (b) Setup of single sideband swept source (c) Transmission spectrum showing FSR of 2.72 GHz, demonstrating a unique FSR due to single polarization operation.*

A fabricated Si_3N_4 waveguide laser chip is shown in the contrast enhanced image in Figure 4.3(a). The resonator length, L is ~74 mm, with a waveguide group index of 1.478 and optical mode area = 27.83 μm^2, yielding a cavity mode volume ~ 2.07 x 10^{-12} m^3. The FSR was measured by monitoring the scope output while tuning a single-sideband (SSB) of a modulated laser (Figure 4.3(b)) through two resonance dips of the cavity. The lower side band (LSB) was extracted by applying a two cascaded stages of narrow fiber Bragg grating filter (Oeland custom-made gratings) to suppress the carrier and the upper sideband (USB) of an intensity-modulated (EO space modulator) fiber laser (NP Photonics Rock laser). The modulator RF bias frequency, f_m was tuned across the resonance dips of the ring to measure the FSR to be around 2.72 GHz (no additional dips were seen indicating single TE optical mode operation).

4.3.1 RF Calibrated MZI Based Resonator Characterization

A 200 m unbalanced fiber-based unbalanced Mach-Zehnder interferometer (UMZI) was used as a reference frequency spectrum to accurately measure the resonator Q[73]. The interferometer FSR of the fiber UMZI was measured using the single sideband swept source setup shown in Figure 4.3(b). The intensity maxima (and minima) frequency spacing on the scope output corresponding to the interferometer FSR, measured to be 1.07 ± .0146 MHz. By simultaneously scanning the laser frequency through both the MZI and device under test, the MZI fringe spacing (FSR) provides an RF calibrated frequency reference for accurate evaluation of resonator Q factors. The transmission curve of the resonator (blue trace in Figure 4.4(a)) is fit to the standard Lorentzian response of an all-pass resonator[74] given by

$$\frac{P_{Out}}{P_{In}} = \frac{a^2 - 2ra\,cos\phi + r^2}{1 - 2ra\,cos\phi + (ra)^2} \quad (4.1)$$

where $\phi = \beta L$ is the single-pass phase shift, with β being the propagation constant of the circulating optical mode. The quality factor of a representative resonator (design-2) measured to be 28.2 million (shown in Figure 4.4(a)). The optical loss (α (dB/m) = $\frac{8.686 \ln(a)}{L}$) and power coupling coefficient (κ^2) extracted from the fit are 0.4 dB/m and 0.878 %.

4.3.2 Cavity Ring-Down Measurements

Standard cavity ring-down technique[62] was used an independent measurement of resonator Q to corroborate the Q-values obtained from the RF calibrated MZI Q measurements. For this measurement, a fiber laser, connected to an intensity modulator and edge coupled to the ring resonator was swept around resonance by applying a triangular voltage input to its piezo electric transducer (PZT) input. Further, a 50% duty cycle, 10 kHz square wave was applied to the intensity modulator with fast switching response (< 10 ns) that acted as the gating signal. When the gating signal is "off" at ring resonance, the optical power inside the cavity discharges showing an exponential decay of optical intensity at the transmission port. This "ring-down" decay time(τ) was measured by monitoring the transmission port output on an oscilloscope and was used to evaluate the loaded quality factor of the resonator ($Q_L = \omega\tau$). The ring-down time and Q_L of a representative resonator (design-2) were measured to be 24.48 ns and 29.8 million as shown in Figure 4.4(b).

These RF calibrated MZI and ring-down measurements correspond to a cold-cavity unloaded ***Q (Q_U) ~65 million and loaded Q (Q_L) ~28.2 million, indicating the highest Q reported till date for any single-mode Si_3N_4 ring resonator with deposited cladding***[41,66].

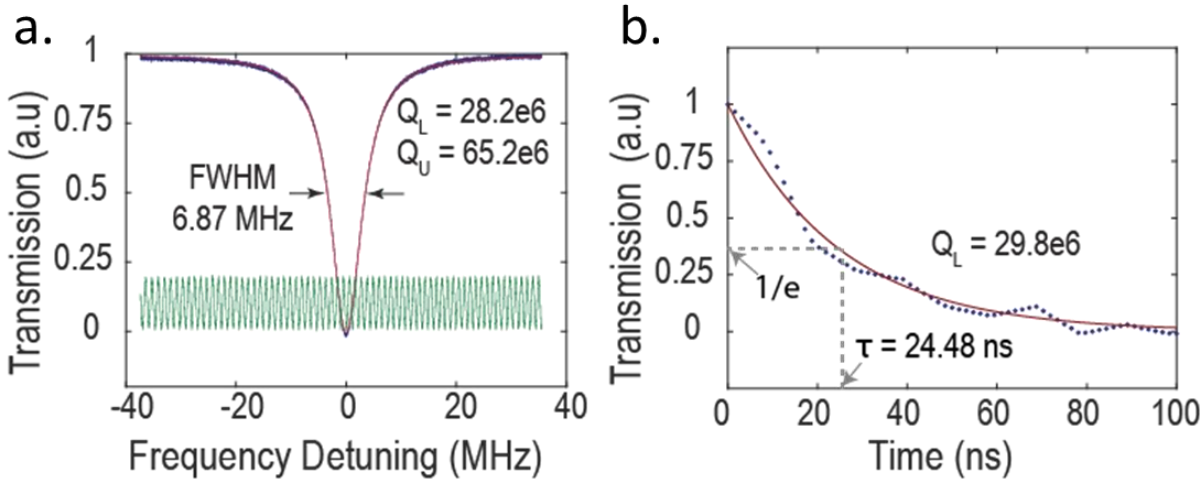

Figure 4.4. Quality Factor Characterization of ULL Si_3N_4 resonators: *(a) RF calibrated MZI measurements of transmission FWHM and calculated quality factors using Lorentzian fit to transmission spectra (b) Ring-down measurement of laser resonator showing a cavity ring-down time of 24.48 ns corresponding to a Q_L of 29.8 million agrees well with the Q value from RF calibrated MZI measurement*

4.4 Wafer Yield

One of the key results of the fabrication process in this work is the high wafer yield and intra-wafer and inter-wafer device performance consistency. This resonator technology is compatible with commercial 4" silicon nitride wafer-scale processing[67].

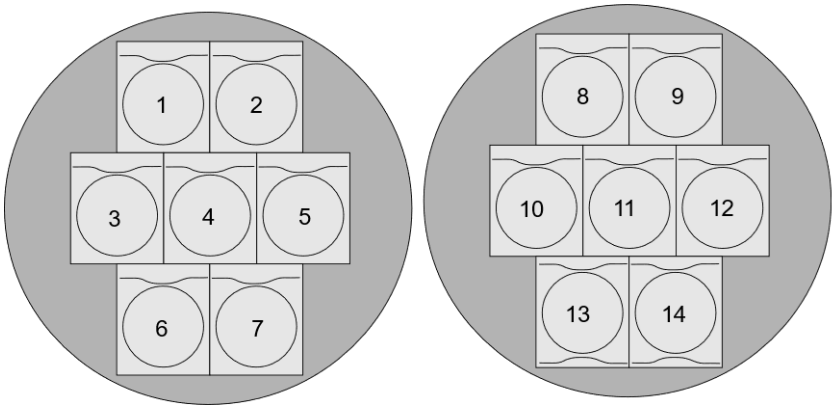

Die #	Wafer #	Q_L
6	1	21.4e6
7	1	23.5e6
8	2	28.2e6
9	2	31.3e6
10	2	28.2e6
11	2	29.1e6
12	2	28.5e6

Figure 4.5. Wafer-Scale Measurements of SBS Laser Die. *Two wafers were fabricated with a total of 14 die. Loaded Q values of 7 representative resonators measured using the RF calibrated MZI technique are shown in the table*

Our laser resonators were fabricated on thermally grown oxide on silicon 4” wafer substrates with 7 lasers per wafer as shown in Figure 4.5 (dies 1-7 used design-1 and dies 8-14 used design-2: see Figure 4.2(b) for design details).The measured quality factor and cavity performance of one representative resonator was discussed in section 4.3. To characterize the repeatability of resonator quality across wafers we measured the loaded Q factor ranging from 21 million to 31 million, for representative die as shown in the table in Figure 4.5.

4.5 Summary

This chapter described the design, characterization, and wafer-yield of SBS laser resonators. The FSR of the ring resonator was measured using single-sideband swept source technique was found to be in excellent agreement with the peak gain frequency of BGS characterized in section 3.6. Loaded quality factor of > 28 million and intrinsic quality factor of > 60 million, measured using two different cavity characterization techniques (RF calibrated MZI and cavity ring-down) indicate the highest measured loaded quality factor for a silicon nitride ring resonator with a deposited cladding. The next two chapters describe realization and performance characterization of Brillouin lasing in these resonators.

Chapter 5: Brillouin Laser Power Dynamics

5.1 Abstract

In this chapter, the experimental results and theoretical analysis of cascaded Brillouin lasing observed in silicon nitride waveguide resonators are presented. The concepts and analytical expressions for lasing threshold and power evolution of Stokes orders in a cascaded SBS laser are introduced and cascading up to 10 Stokes orders and a small amount of Brillouin-induced Four-wave-mixing (FWM) is demonstrated by optically pumping the silicon nitride waveguide resonator. The measured power evolution of the first three Stokes orders is shown to be in excellent agreement with the power dynamics evaluated by combining the developed theory and the measured resonator parameters (section 4.3).

5.2 Theory of SBS Laser Power Dynamics

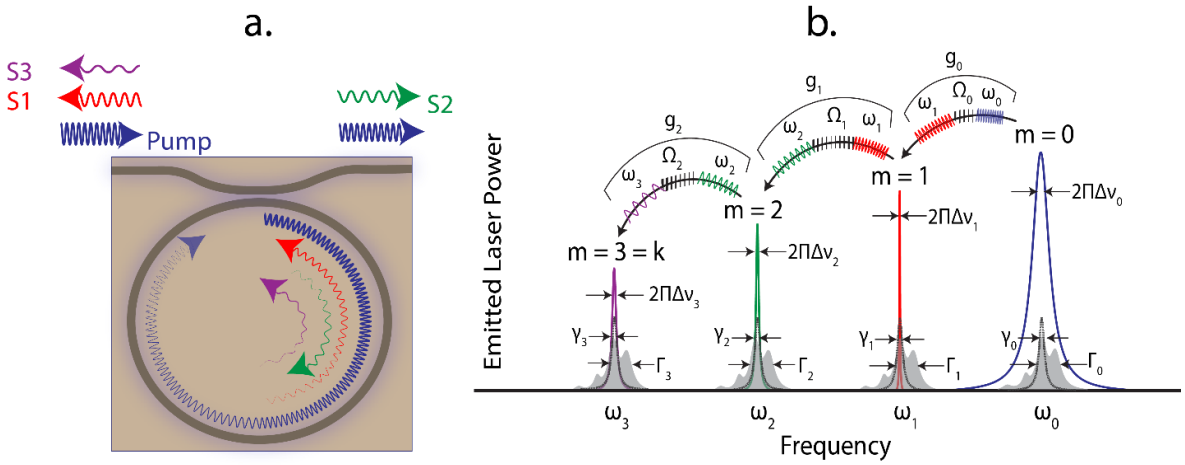

Figure 5.1. Illustration of Cascaded Brillouin Lasing in an Optical Cavities: *(a) Conceptual illustration of Brillouin laser cascading resulting in successive orders of Stokes tones emitted in opposite directions due to BSBS in a ring resonator (b) Spectral representation of Brillouin laser cascading tones and the important opto-acoustic parameters and interactions involved*

This section introduces the concepts of single and cascaded power dynamics of Brillouin laser and provides the theoretical equations from the new theoretical framework

developed by Behunin et al[19] relevant for analyzing cascaded lasing power dynamics observed in our Si_3N_4/SiO_2 microring resonator. A complete mathematical treatment and derivation of these equations can be found in the reference[19]. Brillouin lasing results from the annihilation of a pump photon to generate a Stokes photon and an acoustic phonon. As described in section 2.2 and Figure 2.1(d), the first Stokes order rapidly increases in power due to stimulated Brillouin scattering process when the pump power exceeds the *threshold* value. When the optical intensity of the first Stokes order increases to significantly high value, it acts as a pump for the next higher Stokes order, leading to cascaded Brillouin lasing. This cascaded lasing behavior naturally occurs in WGMRs and ring resonators, where the optical modes are regularly spaced by the cavity free spectral range (FSR) (see Figure 5.1(a,b)). The physics of a cascaded Brillouin laser can be described by the model Hamiltonian H given by

$$H = \hbar \sum_m \left[\omega_m a_m^\dagger a_m + \Omega_m b_m^\dagger b_m + (g_m a_m^\dagger a_{m+1} b_m + H.c.)\right] \qquad (5.1)$$

Here, a_m and b_m are the respective annihilation operators for the m^{th} optical and phonon modes, with respective angular frequencies of ω_m and Ω_m. The mode index m labels the cascaded Stokes order, m = 0 corresponding to the pump, m = 1 corresponding to the first Stokes order, etc. This model generalizes the treatment of optomechanical laser noise described in prior work[15,17,48,75,76] to include the effects of cascaded lasing. In contrast with linear waveguides, where mode amplitudes can change along the system's symmetry direction, this model treats the field within the optical and acoustic resonator as independent of space, and essentially composed of a pure k-vector mode (either traveling or standing); this aspect contrasts with the work of Debut et al.[18], which accounts for the spatial dynamics of the optical field throughout the laser resonator. This approximation is valid so long as the loaded optical

decay rate and the gain bandwidth are much smaller than the resonator FSR. The coupling rate g_m quantifies the Brillouin interaction between the mth phonon mode and the mth and (m+1)th optical modes, including the effects of spatial phase matching. The framework to determine opto-acoustic coupling rate due to the spatial overlap of the acoustic and optical modes, is qualitatively described in section 2.3 and discussed rigorously in detail in Behunin et al[19] and Qiu et al[49].

In microresonators with high loaded quality factors ($Q_{Tm} = (Q_{Um}^{-1} + Q_{Em}^{-1})^{-1}$ where Q_{Um} and Q_{Em} are intrinsic and external Qs as defined in Eq. (1.12)) such as the one considered in this work, as shown in Figure 5.1(b), the cavity photon decay rate $\left(\gamma_m = \frac{Q_{Tm}}{\omega_m}\right)$ is significantly smaller than the mean phonon decay rate ($\Gamma_m = 2\pi\Delta\nu_B$, where $\Delta\nu_B$ is Brillouin gain bandwidth). In this mode of operation, Eq. (5.1) can be used to deduce the threshold powers and steady state power dynamics of each Stokes order of a cascaded-order Brillouin laser as described in Behunin et al[19]. The steady-state emitted Stokes power of the mth mode P_m is related to the intracavity photon number N_m ($= a_m^\dagger a_m = |a_m|^2$) and external Q as $P_m = \left(\frac{\hbar\omega_m^2}{Q_{Em}}\right) N_m$. The threshold power required to initiate stimulated Brillouin scattering of mth Stokes power is given by

$$P_m^{th} \approx \frac{\omega_m^2 n_g^2 L Q_{Em}}{32\left(\frac{g_{Bm}}{A_{eff}}\right) Q_{Tm}^3 c^2} \begin{cases} m(m+2)^2 & m\ even \\ (m+1)^3 & m\ odd \end{cases} \qquad (5.2)$$

where c is the velocity of light in vacuum, n_g is the group index, L is the resonator length, and $\left(\frac{g_{Bm}}{A_{eff}}\right)$ is the Brillouin gain coefficient in m^{-1}W^{-1} (described in section 3.5).

The steady-state emitted optical powers of the even (2m) and odd (2m+1) Stokes orders for varying optical pump power (P_{pump}) in cascaded Brillouin laser with an odd number (2k+1) of cascaded orders can be evaluated using

$$P_{2m} = \frac{\hbar\omega_{2\text{m}}\gamma_{\text{ext}}\gamma}{2\mu'}(k+1-m) \quad (5.3a)$$

$$P_{2m+1} = \frac{4\omega_{2\text{m}+1}{\gamma_{\text{ext}}}^2}{\omega_{\text{pump}}\gamma^2}\frac{m+1}{(k+1)^3}\left[\sqrt{P_{2k+1}^{th}P_{\text{pump}}}\frac{k+1}{m+1} - P_{2k+1}^{th}\right] \quad (5.3b)$$

where $\mu'\left(=\frac{\hbar\omega_{\text{m}}c^2}{2n_g^2L}\left(\frac{g_{Bm}}{A_{eff}}\right)\right)$ is the Brillouin amplification rate per photon (Hz). The analysis also assumes the resonator Q remains unchanged for pump and Stokes orders ($\gamma_{\text{extm}} = \gamma_{\text{ext}}$ and $\gamma_{\text{m}} = \gamma$ for all m) thereby neglecting the effect of dispersion, and can be justified since the pump-Stokes frequency difference is very small (~GHz) compared to the optical frequencies. For an even number (2k) of cascaded orders, the emitted optical powers in the even (2m) and odd (2m+1) Stokes orders are described by

$$P_{2m} = \frac{4\omega_{2\text{m}+1}{\gamma_{\text{ext}}}^2}{\omega_{\text{pump}}\gamma^2}\frac{1}{(k+1)^2}\left[P_{\text{pump}} - \frac{m}{k}P_{2k}^{th}\right] \quad (5.4a)$$

$$P_{2m+1} = \frac{\hbar\omega_{2\text{m}+1}\gamma_{\text{ext}}\gamma}{2\mu'}(k-m) \quad (5.4\text{b})$$

Equations (5.3, 5.4) agree with the theoretical framework for steady-state power dynamics of Raman and Brillouin lasing in silica resonators[15,44]. Similar to their work, the framework predicts alternating power clamping of Stokes orders depending on the highest order of lasing can also be observed from these equations. For k$^{\text{th}}$-order cascading, the (k−1)$^{\text{th}}$ mode is clamped. As a result, the equations imply that the modes k−3, k−5, k−7,... are clamped

as well. In other words, if k is even, all odd orders are clamped, and if k is odd all even orders are clamped.

Equations (5.3, 5.4) also provide an insight to the physical processes resulting in the power-dynamics behavior of cascaded Brillouin lasers and is detailed in ref[77]. Each Stokes wave having reached the laser threshold must satisfy the criterion of equality between losses and gain on a single pass of resonator. Since each Stokes order, except the first and the last orders is generated by the previous one and serves as a pump to the next, a recurrence relation between powers of Stokes orders is established with constant power difference, P_C between successive even or odd Stokes orders as shown in Figure 5.2 and can be evaluated from Eqs (5.3b, 5.4b). The constant power difference is related to the conversion efficiency of power between Stokes orders and results in clamping of Stokes powers depending on the number of Stokes orders.

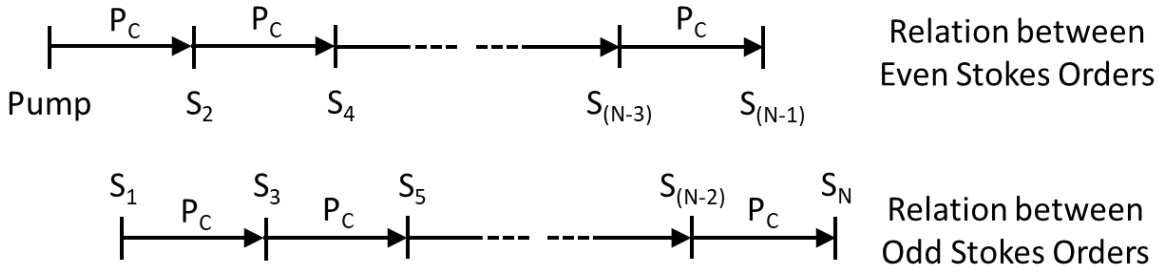

Figure 5.2. Power Evolution of Stokes Orders: *The power difference between successive Stokes orders is determined by the equality between gain and loss on a single pass resonator and can be evaluated using Eqs. (5.3, 5.4)*

The theoretical model used here to derive the steady-state power dynamics in Eq. (5.3, 5.4) neglects the interactions produced by the Kerr effect, such as self- and cross-phase modulation. This is a good approximation in a variety of materials like CaF_2[16], silica[46] or Si_3N_4/SiO_2 (this work) used to create Brillouin lasers, where Brillouin coupling is much larger

than Kerr nonlinearities. Kerr nonlinearities can shift the resonance conditions for the laser resonator and mimic the effects of cascaded-order lasing by energy transfer through four-wave mixing (FWM). When the pump laser is locked to the resonator, the primary effect of Kerr-induced resonance frequency shifts is to perturb the phase matching for Brillouin scattering. These effects are negligible when the shift in frequency is much less than the Brillouin gain bandwidth, quantified by the inequality given by $\omega_m n_2 I/(n\Gamma) << 1$, where n_2 is the Kerr-induced second-order refractive index, and I is the total optical intensity inside the resonator. This inequality is well satisfied for the Si_3N_4/SiO_2 waveguide Brillouin laser described in this work over the range of investigated powers (i.e., intracavity power much less than 1500 W).

The relative importance of FWM can be quantified by taking the ratio of the bulk Brillouin gain g_B to $\omega n^2/c$, representing the spatial rate of energy transfer per W/m^2 produced by the Kerr effect. In high band gap materials, such as silica[46] and CaF_2[16], this ratio $cg_B/(\omega n_2)$ is ~163 at 1.55 μm in silica and ~532 at 1.06 μm in CaF_2[78], illustrating that FWM is perturbative in these systems. A minute amount of FWM induced by Brillouin laser cascading is observed in this work and will be described later in the chapter, the impact of this on the lasing dynamics is considered negligible similar to other silica systems and not taken in to account for the theoretical fit of measured results.

5.3 Measurement of Cascaded SBS Laser Power Dynamics

5.3.1 Experimental Setup

Brillouin laser dynamics of our silicon nitride waveguide laser demonstrating cascaded Stokes order lasing to ten Stokes orders (S1 – S10) is shown in Figure 5.3. Measurements made using the characterization setup shown in Figure 5.3(a) include transmission and reflection optical spectra using an OSA, RF beat tones between cascaded Stokes orders using an ESA, Stokes

power transfer curves at both ports, and optical threshold for three Stokes orders of devices from two different wafers. A 1550 nm tunable fiber pump laser was coupled to the resonator mounted on a temperature-controlled stage. The pump was locked to a resonator mode using an external phase modulator and Pound-Drever-Hall (PDH)[79] feedback loop.

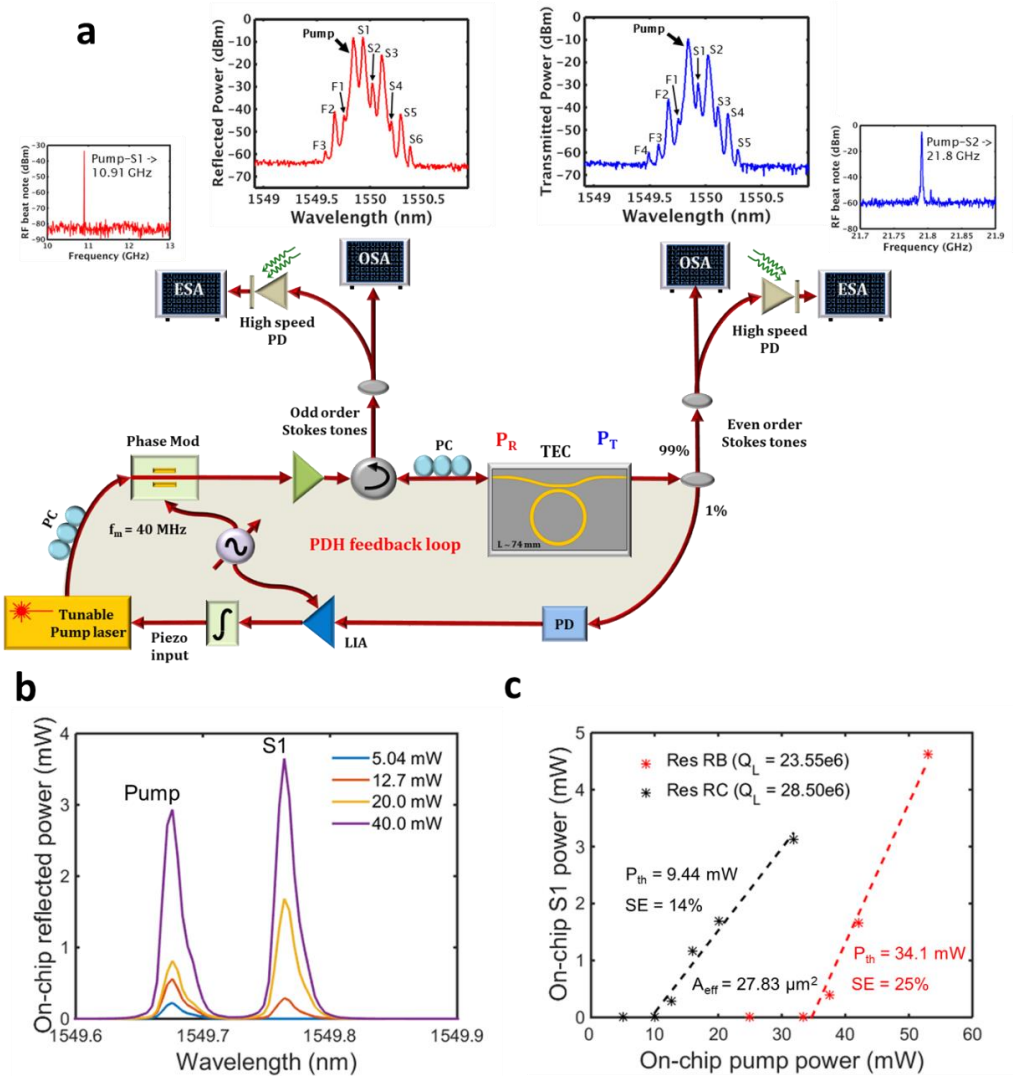

Figure 5.3. Brillouin Laser Power Dynamics Characterization: *(a) Experimental setup to measure laser power dynamics showing integrated waveguide Brillouin gain medium and resonator chip on temperature-controlled mount, with external continuous-wave pump laser and PDH feedback loop. OSA and ESA measurements at the reflection and transmission ports were used to measure Brillouin even and odd Stokes orders and pump-S1 (10.9 GHz) and pump-S2 (21.8 GHz) RF beat-tones. (b) Threshold behavior of first Stokes order for resonator RC (c) On-chip pump power vs. on-chip first Stokes order power for resonators RB and RC*

The coherent emission of Stokes light is measured at the reflection port (P_R) and transmission port (P_T) for the odd and even Stokes orders respectively. Ideally, as Stokes energy buildup occurs, the odd Stokes orders are generated counter-propagating to the pump and are emitted from port P_R, while the even Stokes orders co-propagate with the pump and are emitted from port P_T. However, reflections at the chip facets result in energy from a portion of odd orders appearing at port P_T and a portion of energy from even orders appearing at port P_R. An example of transmission and reflection optical spectra and an RF beat tones are shown in the OSA and ESA traces in Figure 5.3(a).

5.3.2 Threshold and Slope Efficiency of First Stokes Order

Brillouin laser emission for the first Stokes order (S1) is observed (see Figure 5.3(b)) as a function of the on-chip pump power. As an example, the onset of lasing for Resonator-C (RC) (die #8 in Figure 4.5) was observed at ~13 mW as the pump is increased. As the pump power is further increased the cascading of higher Stokes orders is observed and the power in S1 becomes clamped. Using an optical spectrum analyzer (OSA) to measure the output of both bus coupled ports we observe the pump and the even and odd Stokes orders similar to the traces shown above the OSAs in Figure 5.3(a). Lasing threshold and pump vs. Stokes power were measured for two sample resonators and three stokes orders. The optical CW pump vs. first order Stokes power along with linear fits of S1 power is plotted for resonators RC (die #8 in Figure 4.5) and RB (die #7 in Figure 4.5) in Figure 5.3(c) demonstrating threshold at ~10 mW and 34.1 mW respectively. The loaded Q values of 28.50 million and 23.55 million for these resonators demonstrate the increased efficiency and decreased threshold with increased loaded Q.

By lowering the coupling factor to 0.25% and increasing the loaded Q to 28 million (compared to coupling factor of 0.5% and loaded Q of 23.55 million of resonator RB), the threshold power for resonator RC decreased to ~10 mW with a slope efficiency close to 10%. The decrease in slope efficiency for RC occurs due to various factors including power shedding into higher Stokes orders. The threshold optical power for S2 and S3 for resonator RC were measured to be approximately 50 mW and 100 mW respectively.

5.3.3 Brillouin Cascading and Four-Wave Mixing

In addition to optical fields generated from the Brillouin nonlinearity, four-wave mixing (FWM) produces frequencies that coincide with Stokes orders and generates new frequencies (as seen in Figure 5.3(a) and here in Figure 5.4(a)) on the blue shifted side of the pump, similar to observations in chalcogenide waveguides[80]. We indicate the FWM frequencies by FWMX;Y;-Z as shown in Figure 5.4(a), where X, Y and Z are the contributing Stokes orders. This contribution of FWM is observed in Figure 5.4(a). The pump power is initially set to generate only S1 and FWM is not observed (grey trace). As the pump power is increased to generate S2, degenerate FWM between the pump and S2 is observed as the blue shifted and red shifted tones denoted by FWMP;P;-S2 and FWM S2;S2;-P in Figure 5.4(a). The blue shifted FWM field cannot be explained as an anti-Stokes process and the red shifted FWM field cannot be efficiently generated by Brillouin scattering until S3 reaches threshold.

Cascaded Stokes order lasing dynamics become evident when the pump power is increased well above the lasing threshold which causes the circulating Stokes power to reach sufficient levels to initiate lasing in higher order SBS modes demonstrating highly efficient cascaded lasing up to 10 Stokes orders (S1 – S10). The spectra in Figure 5.4(b) is taken at pump input power well above threshold.

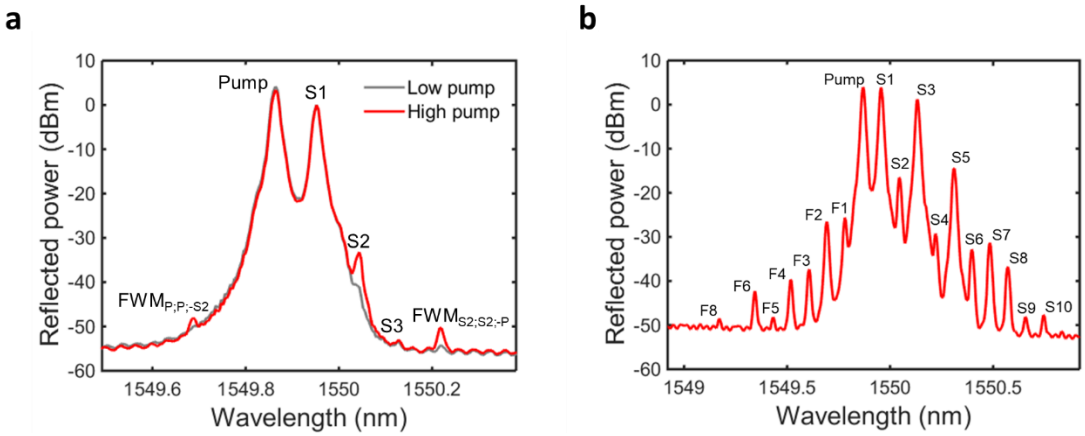

Figure 5.4. Observation of Brillouin Induced Four-Wave Mixing and Cascading up to 10 Stokes Orders: *(a) Demonstration of four wave mixing generation. (b) Reflection port optical power spectrum for resonator RA (die # 6 in Figure 4.5) showing cascading of 10 Stokes orders and four-wave mixing tones*

5.3.4 Analysis of Laser Dynamics and Theoretical Fitting

The measured cascaded Stokes power evolution of the first and third order Stokes emissions of resonator RC are fit to equations (5.3, 5.4) as shown in Figure 5.5. The resonator and waveguide parameters used for the fit are listed in Table 5.1. The theory predicts the steady state power dynamics using the measured Brillouin gain, the resonator linewidth, the ring-bus coupling (κ^2), and a calibration factor (β) relating the on-chip power to the power measured on the OSA. By fitting the measured laser output power to these analytical expressions, we obtain the power coupling from the laser to the OSA and κ^2, the only under-constrained parameters. The analytical power evolution curves show excellent agreement for $\beta = 0.35$ and $\kappa^2 = 0.009$. The measured cold-cavity resonator characteristics used to generate the Stokes predicted fit power curves (Fit: CC) agrees well until the input pump is increased beyond 150 mW. We attribute this deviation to changes in the resonator characteristics under hot-cavity conditions.

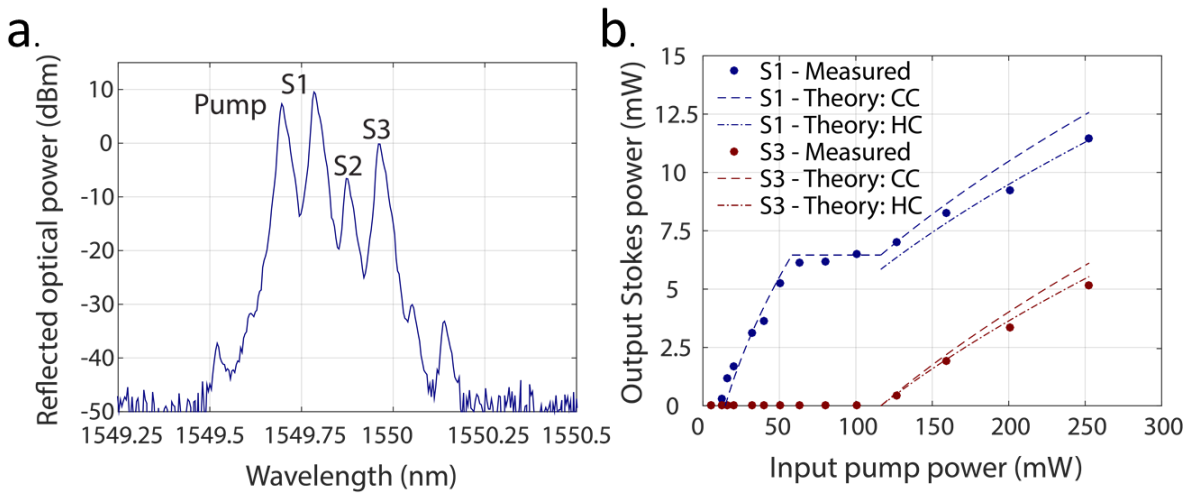

Figure 5.5. Cascaded Order Power Dynamics and Analytical Fits: *(a) Measured optical power spectrum at the reflection port for three Stokes orders showing pump and second order reflection. (b) Measured cascaded power dynamics of first and third Stokes orders with corresponding theoretical curves using cold cavity (CC) parameters and extraction of hot cavity (HC) parameters at high pump input powers. Power of first order Stokes emission clamps at the onset of second order Stokes order.*

At high input pump powers, where the intra-cavity intensity builds to very high values and thermal effects induce changes in cavity parameters including the bus-ring power coupling coefficient (κ^2) and the waveguide group index (n_g). Performing a hot-cavity (HC) fit for S1 and S3 where the output power decreases, as shown in Figure 5.5(b), provides an estimated 5% increase in the external quality factor (Q_{ext}).

The fit agrees well with the expected behavior of cascaded power dynamics of Brillouin laser[19]. From the fit, we obtain the optical threshold of the first Stokes order as 14.6 mW which is close to the measured threshold of ~10 mW. Beyond the second Stokes order threshold (58.4 mW), first Stokes order is measured to clamp at ~6.2 mW which agrees well with the predicted value of clamped power for the first Stokes order (6.46 mW) from Eq. (5.4b). Additionally, when the pump power is increased to be slightly greater than the third order Stokes threshold (116.3 mW), the difference between the theoretical fits of first and third Stokes orders is ~6.5 mW which is close to the clamped power of first Stokes order, as expected. For even higher

pump powers (P_{pump} > 150 mW), the measured Stokes power is seen to be less than the predicted values. The deviation of power dynamics fit from the measured characteristics due to change of resonator characteristics under hot cavity conditions.

Table 5.1: Summary of cold-cavity characteristics of resonator and Brillouin lasing parameters of silicon nitride waveguides used for fitting of cascaded Brillouin power dynamics

Pump frequency (ω_{pump})	2π x 193.55 THz
Optical cavity decay rate (γ)	2π x 6.79 MHz
External decay rate (γ_{ext})	2π x 3.81 MHz
Resonator length (L)	74.14 mm
Group index (n_g)	1.478
Brillouin gain coefficient (G_B)	0.1 $m^{-1}W^{-1}$
Brillouin amplification rate per photon ($\mu = \left(\frac{\hbar\omega c^2 G_B}{2n_g^2 L}\right)$)	3.55 mHz
External Q, $Q_{ext} = \frac{\omega}{\gamma_{ext}} = \left(\frac{2\pi n_g L}{\lambda}\right)(\kappa^2)^{-1}$	50.71 million
Loaded Q, $Q_T = \frac{\omega}{\gamma}$	28.5 million
Loss (α)	0.4 dB/m
Power coupling coef. κ^2	0.878%
Intrinsic Q, $\frac{1}{Q_{Int}} = \frac{1}{Q_T} - \frac{1}{Q_{ext}}$	~65 million
Theoretical S1 threshold, $P_{th}^1 = \frac{\omega^2 n_g^2 L Q_{ext}}{4 G_B Q_T^3 c^2}$	14.6 mW

5.4 Summary

This chapter presented the theoretical equations that govern the cascaded lasing dynamics of cascaded Brillouin lasers pertinent to high Q optical resonators like the ones used in this work. The characterization of threshold as low as ~10 mW and slope efficiency as high as 25 % for

the first Stokes order in our silicon nitride waveguide Brillouin laser is shown and cascading of Brillouin lasing up to 10 Stokes orders is demonstrated. Observation of Brillouin induced four-wave mixing is demonstrated. The measured cascaded lasing power dynamics are shown to be in excellent agreement with the theory. The results promise the ability to engineer the slope efficiency by changing the design parameters (design #1, 2 for RB, RC respectively). The next chapter discusses the noise dynamics properties of the laser.

Chapter 6: Brillouin Laser Noise Dynamics

6.1 Abstract

This chapter discusses the theory, results and analysis of frequency and intensity noise dynamics of our silicon nitride waveguide Brillouin laser. Linewidth narrowing in Brillouin lasers is described and analytical expressions to evaluate fundamental linewidth of any Stokes order in a cascaded Brillouin lasing system are presented. The broad gain bandwidth, high quality factor, and large optical mode area of our silicon nitride waveguide Brillouin laser are shown to be advantageous for realizing ultra-narrow linewidth lasers. The absolute frequency noise measurement results demonstrating sub-Hz fundamental linewidth lasing are detailed and RIN measurements with a minimum of -150 dBc/Hz RIN at > 20 MHz frequency offset are discussed.

6.2 Theory of SBS Laser Noise Dynamics

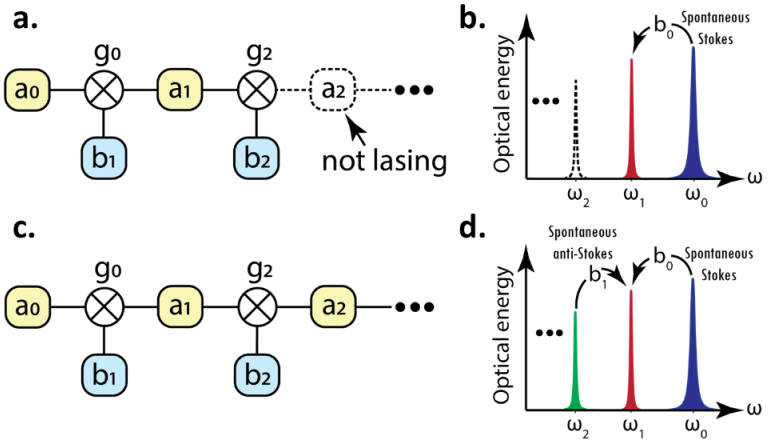

Figure 6.1. Illustration of noise dynamics in cascaded Brillouin lasers: *Tiles represent optical and acoustic modes. The mixer symbol represents the nonlinear optomechanical coupling between two optical modes and one acoustic mode. (a,b) Below threshold for cascaded lasing, optomechanical coupling enables noise transfer between the m = 0 and the m = 1 through spontaneous Brillouin scattering from the phonon mode b_0. (c,d) Above threshold for cascaded lasing noise can be injected into the m = 1 mode from spontaneous scattering from thermal phonons in the b_0 and b_1 modes.*

This section presents the mathematical framework of fundamental noise dynamics of a cascaded Brillouin lasing system reported in Behunin et. al[19]. Optomechanical coupling produces a nonlinear interaction between three waves in a manner that is similar to a mixer (see Figure 6.1), where the mixer output frequency is given by the sum and difference of the two injected tones. Using this analogy, we can explain the optomechanical noise present in Brillouin lasers. For example, when a coherent field in the optical mode a_0 and a noisy acoustic field b_0 (due to thermal fluctuations) are injected into neighboring mixer ports, the mixer output comprises a coherent carrier with two noisy sidebands. In a Brillouin laser, the frequency of the lower sideband is given by ω_1, and as a result this spontaneous Stokes scattering process injects noise into the a_1 mode. Likewise, a coherent field present in the optical mode a_1 can also mix with an acoustic field to produce a carrier with noisy sidebands. However, in this case the frequency of the higher sideband is given by ω_0, thereby transferring noise from the acoustic field to the a_0 mode through spontaneous anti-Stokes scattering (see Figure 6.1(c,d)). Below the cascaded lasing threshold, the optical mode a_2 is neither coherent nor occupied with a large number of quanta. In other words, a_2 is noisy and fluctuates in amplitude around zero. While this noisy field, in addition to a noisy acoustic field b_1, can be injected into the two ports of a mixer to produce multiplicative (spontaneous-spontaneous) noise in the a_1 mode, the magnitude of this noise source is small because the thermal occupation (quantifying the noise amplitude) of the optical mode a_2 is essentially zero. However, once cascaded lasing is achieved, the coherent field now present in the a_2 mode can efficiently transfer noise from the acoustic mode b_1 to a_1 (see Figure 6.1(c,d)), coupling the optical mode a_1 to an additional heat bath. These noise channels, introduced by cascading, enhance the phase and amplitude noise, thereby producing contrasting behaviors from single-mode Brillouin lasers[15,16,46].

6.2.1 Frequency Noise and Fundamental Linewidth

The fundamental linewidth of the Brillouin laser is determined by the white frequency noise contributions from the Stokes orders. This includes noise contribution of spontaneous scattering from the optical mode that acts as the pump for the current Stokes order and anti-spontaneous scattering from the higher Stokes orders. The mathematical treatment and the derivation of fundamental linewidth for cascaded Brillouin laser systems is detailed in Behunin et. al[19] and this section shows only the final result of the analysis. The reader is encouraged to go through the reference for a complete understanding of the derivation of noise dynamics. For the m^{th} Stokes order, the fundamental linewidth $\Delta\nu_m$ is given by[19]

$$\Delta\nu_m = \frac{1}{4\pi N_m}\left[\gamma_m\left(N_m^{th} + n_{m-1}^{th} + 1\right) + 2\mu' N_{m+1}\left(n_m^{th} + n_{m-1}^{th} + 1\right)\right] \quad (6.1)$$

Here, γ_m, μ', $N_m \left(= \left(\frac{Q_{Em}}{\hbar\omega_m^2}\right) P_m\right)$ and N_m^{th} are the respective decay rate, Brillouin amplification rate per pump photon, and coherent intracavity and thermal photon numbers, all defined for the m^{th} order. The thermal occupation number, n_m^{th}, is defined for the phonon mode mediating Brillouin scattering between the $(m-1)^{\text{th}}$ and m^{th} Stokes tones. The thermal photon and phonon occupation numbers are evaluated using $N_m^{th} = \frac{1}{e^{\left(\frac{\hbar\omega_m}{k_B T}\right)} - 1}$ and $n_m^{th} = \frac{1}{e^{\left(\frac{\hbar\Omega_m}{k_B T}\right)} - 1}$ where k_B is the Boltzmann's constant and T is the ambient temperature. Given that the optical frequencies are very high compared to the acoustic frequencies, $N_m^{th} \ll 1 \ll n_m^{th}$, and consequently the contribution of thermal photons to laser noise is insignificant, simplifying Eq. 6.1 to $\frac{n_m^{th}}{4\pi N_m}[\gamma_m + 4\mu' N_{m+1}]$ assuming negligible acoustic dispersion ($n_{m-1}^{th} \approx n_m^{th}$).

The fundamental linewidth $\Delta\nu_m$ is dominated by the thermomechanical noise arising from the thermal phonon number n_m^{th} (~570 at room temperature). The thermal phonon

contribution in Brillouin lasers is generally small compared to the spontaneous emission contribution in semiconductor lasers, thus resulting in linewidth narrowing from pump to Stokes. This is the primary distinction between semiconductor lasers and Brillouin lasers that the noise contribution in semiconductor lasers is dominated by the photons from spontaneous emission and the noise in Brillouin lasers is only due to the contribution of thermal phonons resulting from (Stokes or anti-Stokes) spontaneous scattering. Notably, thermal phonons only from the adjacent orders: spontaneous Stokes scattering from immediate lower Stokes mode (n_{m-1}^{th} : from $(m-1)^{\text{th}}$ to m^{th} Stokes) and spontaneous anti-Stokes scattering (n_m^{th} : from $(m+1)^{\text{th}}$ to m^{th} Stokes) from next higher mode contribute to the fundamental linewidth broadening, increasing white frequency noise floor (using Eq. (1.5), $S_f(\nu) = \frac{\Delta\nu_m}{\pi}$) of m$^{\text{th}}$ Stokes order. This means the phase dependence exists only between adjacent Stokes orders, making Stokes orders that are more than an order apart phase-independent of each other.

Also, Eq. (6.1) does not indicate contribution or transfer of phase noise from pump to Stokes orders. The total fundamental linewidth of Stokes order $\Delta\nu_{mT}$ is a combination of linewidth broadening due to pump phase diffusion, $\Delta\nu_m^{tr}$ and linewidth contribution from spontaneous scattering, $\Delta\nu_m$ shown in Eq. (6.1). Such treatment is in agreement with the work of Debut et. al[18] who showed that optomechanical coupling process of Brillouin lasing effectively suppresses the transfer of phase noise from pump to Stokes orders by a factor[18] of K = $(1+\Gamma/\gamma_m)^2$, where Γ is the decay rate of the acoustic mode (when $\Gamma > \gamma_m$). The quantity $\Delta\nu_{mT}$ can therefore can be expressed as

$$\Delta\nu_{mT} = \Delta\nu_m + \Delta\nu_m^{tr} = \Delta\nu_m + \frac{\Delta\nu_{Pump}}{K^2} \qquad (6.2)$$

Since our laser has a relatively large Brillouin gain bandwidth (fast decay rate, $\Gamma = 2\pi$ x 153 MHz), the suppression of transfer of pump phase noise diffusion to Stokes is superior (by at least a factor of 25 compared to silica resonators with $\Gamma \sim 2\pi$ x 30 MHz having equal photon decay rate) compared to other chip-scale Brillouin lasers compared to other all-waveguide designs[48,81]. This makes Si_3N_4/SiO_2 waveguide platform an ideal choice for realizing integrated narrow linewidth Brillouin lasers that are immune to pump phase noise.

6.2.2 Relative Intensity Noise

In addition to the reduction of phase noise and linewidth narrowing, the Brillouin lasing action is also known for reduction of RIN or RIN transfer from pump to Stokes orders[45]. For the m^{th} laser mode, the RIN $S_m^{RIN}(\omega)$ is defined by the two-sided power spectrum of the relative laser power fluctuations:

$$S_m^{RIN}(\omega) = \frac{1}{P_m^2} \int_{\tau=-\infty}^{\infty} \langle \delta P_m(t+\tau)\delta P_m(t) \rangle \; d\tau \; e^{j\omega\tau} \qquad (6.3)$$

where δP_m represents the time-dependent variation of the laser power from its steady-state value P_m. Unlike frequency noise, amplitude noise of a m^{th} Stokes order in SBS lasers is coupled to all other Stokes orders. In this chapter, we limit the discussion and experimental results of RIN to first Stokes order cascading only. For a complete theoretical analysis of RIN of cascaded order Brillouin laser systems, reader is encouraged to refer to the work of Behunin et. al[19]. In the first Stokes order cascading regime, Eq. (6.3) can be used to derive $S_1^{RIN}(\omega)$ as

$$S_1^{RIN}(\omega) = |\chi_{RIN}(\omega)|^2 \begin{bmatrix} \frac{1}{2}\omega_0^{rel\,2}\gamma_0\left(N_0^{th}+\frac{1}{2}\right) \\ +\frac{1}{2}(\omega^2+\Gamma_{RIN}^2)\gamma_1\left(N_1^{th}+\frac{1}{2}\right) \\ +\frac{\mu'\Gamma_0}{4}\left(n_0^{th}+\frac{1}{2}\right)(\omega_0^{rel\,2}N_1 - 2\omega_0^{rel}\Gamma_{RIN}\sqrt{N_1N_0}+(\omega^2+\Gamma_{RIN}^2)N_0)\frac{\Gamma_0}{\omega^2+\Gamma_0^2/4} \end{bmatrix} \qquad (6.4)$$

where $N_0 = \left(\frac{Q_{E0}}{\hbar\omega_0^2}\right)P_0$ and $N_1 = \left(\frac{Q_{E1}}{\hbar\omega_1^2}\right)P_1$ are the steady-state intra-cavity photon numbers of pump and first Stokes orders and are related to the time-independent mean amplitude of external pump field $\sqrt{N_{Pump}}$ as $\left(\frac{\gamma_0}{2} + \mu' N_1\right) = \sqrt{\frac{\gamma_{ext} N_{Pump}}{N_0}}$. $\omega_0^{rel} = 2\mu'\sqrt{N_1 N_0}$ is the RIN relaxation oscillation frequency, $\Gamma_{RIN} = \sqrt{\frac{\gamma_{ext} N_{Pump}}{N_0}}$ is the RIN damping rate, and the quantity $\chi_{RIN}(\omega) = (-\omega^2 - i\Gamma_{RIN}\omega + \omega_0^{rel^2})^{-1}$.

6.3 Measurement of Brillouin Laser Noise Dynamics

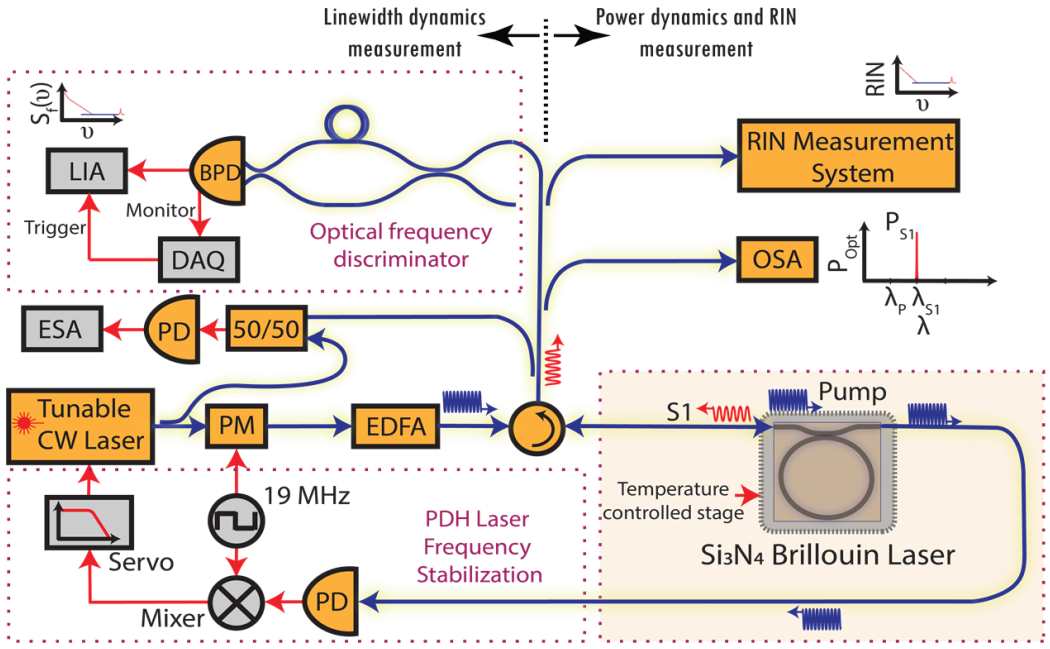

Figure 6.2. Brillouin Laser Noise Dynamics Characterization: *Experimental setup for measurement of Brillouin laser linewidth, phase noise, RIN and power dynamics.*

6.3.1 Frequency Noise and Fundamental Linewidth

Measurement of 0.72 Hz fundamental linewidth for S1 and demonstration of linewidth narrowing as a function of input pump are performed using the experimental setup in Figure 6.2. The setup comprises of an optical frequency discriminator using a fiber-based unbalanced Mach-Zehnder interferometer (UMZI) and a balanced photodetector. The relation between

power spectral density (PSD) of the detector output $S_{out}(\nu)$ in (V^2/Hz), frequency noise of the laser $S_f(\nu)$ in (Hz^2/Hz), and the fundamental linewidth of the laser $\Delta\nu_{S1}$ in Hz, is given by[82]

$$S_f(\nu) = S_{out}(\nu)\left(\frac{\nu}{\sin(\pi\nu\tau_D)\,V_{PP}}\right)^2 \quad (6.5)$$

$$\Delta\nu_{S1} = \pi S_w \quad (6.6)$$

where τ_D is the optical delay of the UMZI, f is the frequency offset, V_{PP} is the peak-peak voltage of the detector output, and S_w is the value of frequency noise where $S_f(\nu)$ is flat (indicates white frequency noise dominated region).

The Brillouin laser output from the reflection port of the circulator is directed to an acoustically isolated, 200 m fiber delay based UMZI with a free-spectral range of ~1.03 MHz (similar to the one used in section 4.3.2). The two outputs of the UMZI are connected to a switchable gain, balanced photo-detector (Thorlabs PDB450C) with a bandwidth of 45 MHz to reduce the impact of intensity fluctuations in the detector output. The power spectral density ($S_{out}(\nu)$) of the detector output is measured over several decades of frequency offsets (sampling rates: 13 kSa/s, 103 kSa/s, 3.3 kSa/s, 13 MSa/s, 26 MSa/s, 53 MSa/s) using a lock-in amplifier (Zurich instruments HF2LI 50 MHz). The monitor port of the detector connected to a National instruments data acquisition controller (NI USB 6259) is programmed to trigger the lock-in amplifier at the quadrature operating point of the UMZI. The single sided FFT data is averaged over 10 traces using an exponential moving average filter and a Hann window is applied to reduce the spectral leakage to evaluate $S_{out}(\nu)$. The measured decade-wise PSD outputs are stitched together and converted to $S_f(\nu)$ using Eq. (6.5). The average value of S_w

is obtained from the flat portion of the measured frequency noise and $\Delta\nu_{S1}$ is then calculated using Eq. (6.6).

Sub-Hz fundamental linewidth lasing emission was measured using our laser resonator (die #12 from Figure 4.5) that demonstrated a first Stokes order threshold of ~10.53 mW (Figure 6.3 (a)). Just below threshold and at threshold, the output power spectral spontaneous emission width ($\Delta\nu_{sp,S1}$) is measured (colored circles in Figure 6.3 (a)) by coherent heterodyning of the pump and Stokes output S1 on an electrical spectrum analyzer (ESA). At the onset of lasing, the fundamental linewidth ($\Delta\nu_{f,S1}$) is measured using frequency noise measurements with a calibrated unbalanced Mach-Zehnder Interferometer (UMZI) at seven points, 3 below and around the first Stokes order threshold, 3 at points midway, and one point just below the S2 threshold (Figure 6.3 (a)).

The ESA heterodyne measurements in Figure 6.3 (b) show the evolution from spontaneous Brillouin emission below threshold (pink curve with FWHM spontaneous linewidth, $\Delta\nu_{sp,S1}$ on the order of 1 MHz) with spectral narrowing starting just below the onset of lasing (yellow curve with $\Delta\nu_{sp,S1}$ ~ 160 kHz). Frequency noise measurements for S1 just above threshold to the onset of S2 lasing, are shown in Figure 6.3(c) as well as that for the pump laser(black).

The slope of frequency noise traces at frequency offset close to 1 kHz is attributed to the demodulation bandwidth of the lock-in amplifier used in the PDH electronics. The peaks in Figure 6.3 (c) beyond 1 MHz are artifacts from data conversion of the optical frequency discriminator output to frequency noise and occur at multiples of the UMZI FSR. Figure 6.3(d)

summarizes the linewidth narrowing exhibiting an inverse dependence of fundamental linewidth on the power in the first Stokes order.

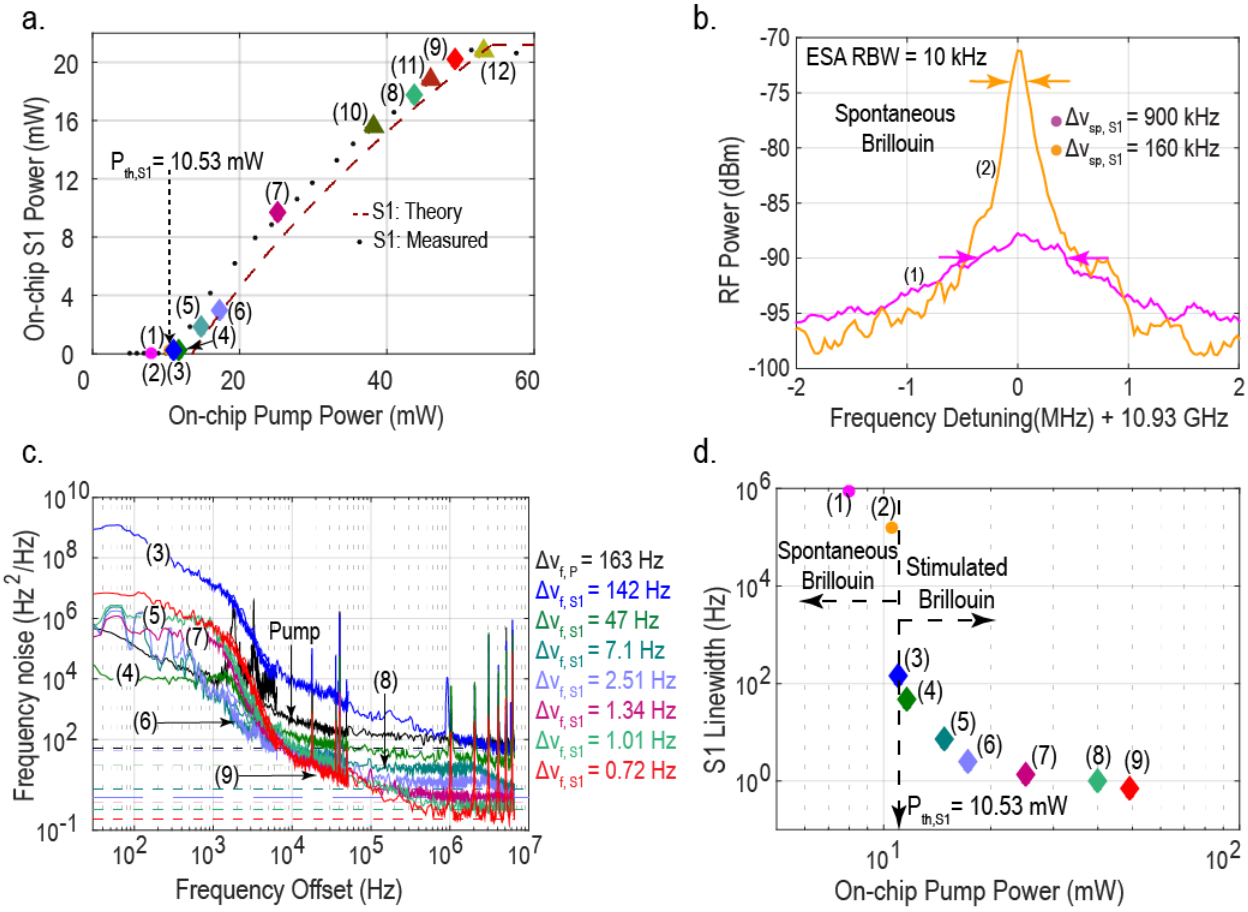

Figure 6.3. Laser linewidth measurement and linewidth narrowing: *(a) Measured power evolution of first Stokes order threshold of 10.53 mW with subthreshold, threshold and above threshold linewidth measurement points indicated. Comparison of theory to measured data shows agreement with predicted behavior. (b) Measurement of laser emission spectrum at two pump powers below threshold using pump-S1 heterodyne beat note measurement on ESA. (c) Measured S1 frequency noise as a function of pump power starting at threshold. Measurements shows single sided frequency noise of S1 where the dotted lines indicate the white frequency noise level of each measurement related to the respective fundamental linewidth of the laser. The pump laser frequency noise and linewidth are shown in black demonstrating significant pump diffusion phase noise reduction and linewidth narrowing. (d) Linewidth evolution of first Stokes order from subthreshold ~ 1 MHz spontaneous linewidth to ~ 0.7 Hz fundamental linewidth at second Stokes order threshold, showing graceful emission bandwidth reduction up to threshold and dramatic linewidth reduction at threshold as well as expected linewidth narrowing trend with increased pump power.*

Significant linewidth narrowing is observed as the pump is increased from below to above threshold and the laser transitions from spontaneous to stimulated emission with a

continued decrease of fundamental linewidth from 142 Hz just above threshold to 0.72 Hz at a point just below the S2 threshold.

6.3.2 Pump Diffusion Linewidth Contribution and Measurement Limitation

The contribution of pump phase diffusion to fundamental linewidth using Eq. (6.2) is calculated to be 0.3 Hz as shown in Figure 6.4(b). The measured (sub-Hz) fundamental linewidth of S1 is detector shot-noise limited. It should be noted that the minimum predicted[19] linewidth (using Eq. 6.2) of our laser is ~0.3 Hz. Our measurements are shot-noise limited near the minimum measurable linewidth of ~ 0.7 Hz using our frequency discriminator due to the increase of shot noise of balanced photo detector noise beyond 10 MHz frequency offset (see Figure 6.4(b)).

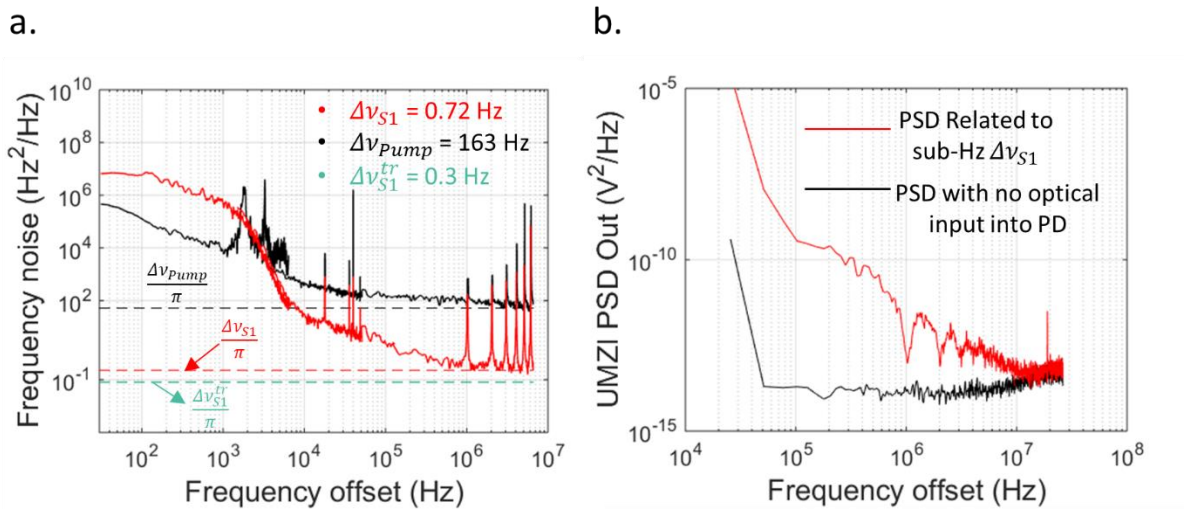

Figure 6.4. Frequency Noise Measurement Limitation: *(a) Contribution of pump phase diffusion to fundamental linewidth of S1 (b) Measured voltage PSD output of S1 at marker 9 of Figure 6.3 and photo-detector with no optical input showing measurement limited by the noise floor of the photodetector beyond 10 MHz due to increased noise of detector.*

6.3.3 Fractional Frequency Stability and Integral Linewidth

The linewidth narrowing action of Brillouin process is evident from the decrease of the white frequency noise of pump from 52 Hz^2/Hz to 0.23 Hz^2/Hz of S1 (marker # 9 of Fig 6.3) as shown in Fig 6.5(a). The associated fractional frequency noise (FFN) for the sub-Hz linewidth emission of S1 was evaluated using Eq. (1.8) measuring fractional deviation as low as 2.5e-15 $Hz^{-1/2}$ at > 1 MHz frequency offsets and is shown in Fig 6.5(c).

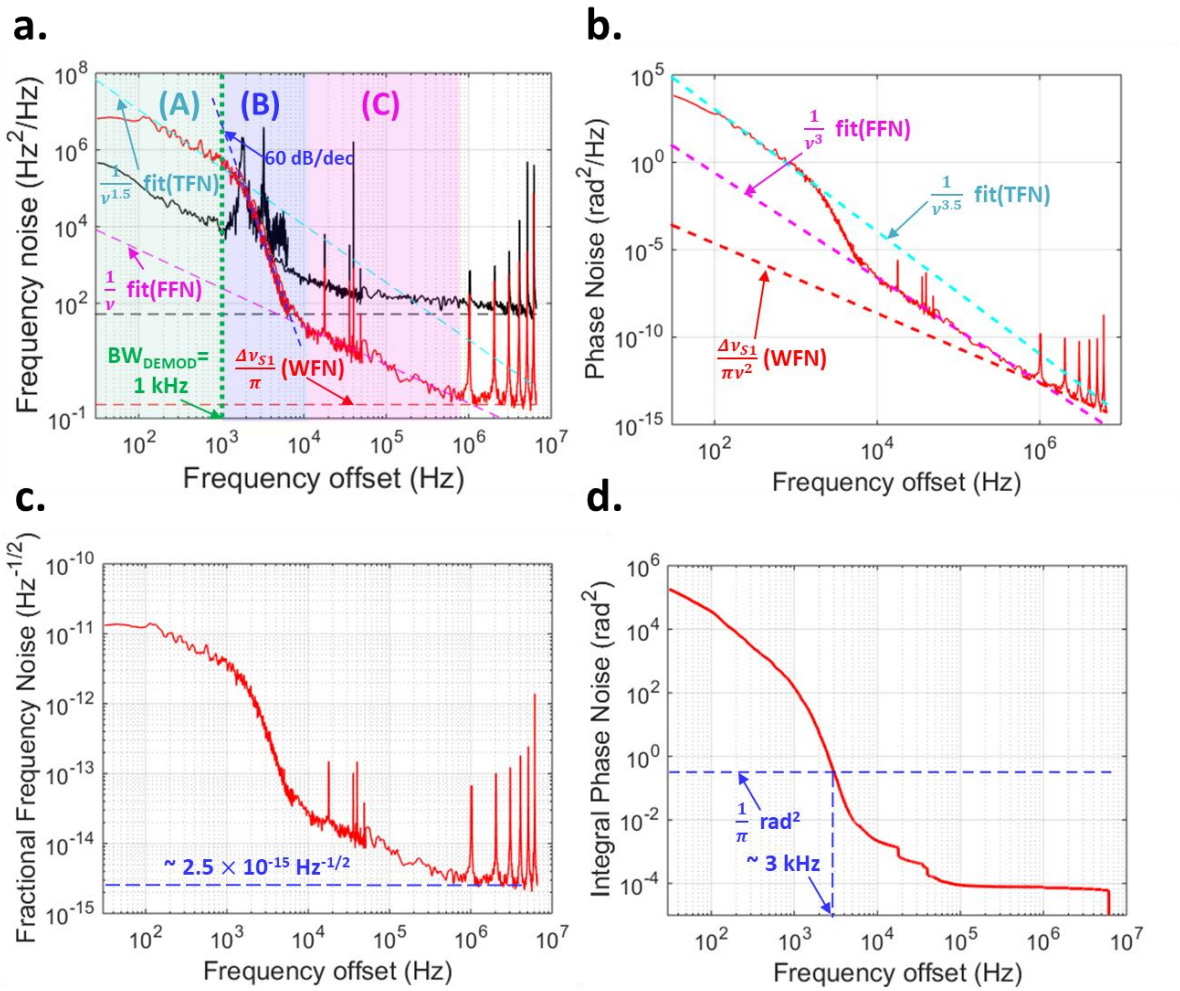

Figure 6.5. Spectral Noise properties of Sub-Hz Fundamental Linewidth Brillouin Laser: *(a) Frequency noise PSD of sub-Hz fundamental linewidth emission of S1 (marker 9 of Fig 6.3) and pump showing white frequency noise (WFN) floor reduction by more than 2 orders of magnitude (black dotted line showing WFN of ~52 Hz^2/Hz for pump vs. red dotted line showing WFN of ~0.23 Hz^2/Hz for sub-Hz fundamental linewidth S1 emission). Red (A), blue (B), and pink (C) shaded regions indicate different regimes of PSD resulting from contribution of thermal frequency noise (TFN), PDH*

demodulation filter-roll off and flicker frequency noise (FFN) sources. The red and black dotted lines indicate the white-frequency noise floor (WFN) showing 2 orders of reduction in WFN from 52 Hz^2/Hz to 0.23 Hz^2/Hz. (b)Phase noise evaluated from frequency noise (c) Fractional frequency noise (FFN) of sub-Hz fundamental linewidth S1 showing a minimum FFN of ~2.5e-15 $Hz^{-1/2}$ at frequency offsets exceeding 1 MHz (d) Evaluation of integral linewidth from integral phase noise using Eq.(1.3)

However, the small deviations at these high frequency offsets indicate the decrease of power in wings of the Lorentzian spectrum of laser but do not necessarily indicate integral linewidth narrowing, as discussed in section 1.3.1. The integral linewidth of sub-Hz fundamental linewidth S1 emission was evaluated using Eq. (1.4) to be ~ 3 kHz, as shown in Fig 6.5(d).

6.3.4 Discussion of Noise Sources

The noise regimes (A,B,C) and power-law spectral noises (flicker frequency and white frequency noises) contributing frequency noise PSD of sub-Hz fundamental linewidth S1 emission (marker # 9 of Fig 6.3) are shown in Fig 6.5(a). Noise contributions in regions (A, C) are predominantly flicker frequency noise or pink noise. These regions correspond to the $1/\nu^{1.5}$ and $1/\nu$ power law spectral noises and both are referred in the literature[83] as "flicker" frequency noise sources. Understanding the origin of the physical processes contributing to these flicker noise sources require a systematic isolation and quantification of the noise processes through simulations and case-specific experiments. Thermodynamic noise contributions can be evaluated through COMSOL simulations of the resonator structure following the approach suggested by Lim et. al[83]. The required experiments can include determination of thermal response time of the SBS laser resonator[63], evaluation of the dependence of Stokes frequency shift on the pump power (discussed in sections 3.7, 7.4.2), optimization of PDH gain-bandwidth parameters through determination of frequency response of the control loop[84] and so on.

The high frequency deviations from region-A exhibit a $1/\nu^{1.5}$ dependence suggesting contributions from thermodynamic frequency noises (TFN) including thermo-refractive and thermo-expansive noise from the resonator similar to the noise observed in fluorite WGM resonators[43,83,85]. The thermal fluctuations in the UMZI frequency discriminator output, and PDH electronics can also contribute to this noise regime. A third order low-pass filter with a bandwidth of 1 kHz was used for demodulation and can be seen from the 60 dB/dec or 18 dB/oct roll off in region (B) beyond the 1 kHz cut-off frequency of the filter.

Table 6.1: Summary of suspected contributions and mitigation strategies for the noise sources identified in Fig 6.5(a)

Region	Dependence on ν	Suspected noise sources	Mitigation Strategies
A	Varies as $1/\nu^{1.5}$	• Flicker frequency noise: ○ Thermodynamic noise from resonator ▪ Thermo-refractive ▪ Thermo-expansive ○ Technical noise from PDH electronics ○ Thermal noise from UMZI	• Improved locking and servo electronics • On-chip actuators[86] or chip enclosures[83] • Locking to a low thermal noise cavity[87] • Thermal isolation of UMZI
B	60 dB/dec roll-off	• Third order cascaded low-pass filter used for lock-in amplification with demodulation bandwidth of 1 kHz	• Optimization of gain-bandwidth parameters of error-signal generation and servo bandwidth[35,84,88]
C	Varies as $1/\nu$	• Flicker frequency noise: ○ Technical noise from PDH electronics ○ Thermal noise from UMZI ○ Thermo-refractive noise from resonator	• Improved locking and servo electronics • On-chip actuators[86] or enclosures[83] • Locking to a low thermal noise cavity[87]
Beyond C	Constant at 0.23 Hz^2/Hz	• White frequency noise: ○ Detector shot noise (see Figure 6.4) ○ Pump phase diffusion ($\Delta\nu_1^{tr}$, see Figure 6.4) ○ Thermal phonon noise ($\Delta\nu_1$, see Figure 6.4)	• Increase of loaded Q of resonator • Optimization of Brillouin gain spectrum • Better photo detectors

The flicker noise contribution shown in region (C) showing 1/ν dependence is attributed to technical noise sources from PDH electronics including servo and demodulation electronics, detector noise and flicker (1/ν) noise arising from thermal fluctuations inside the resonator. Beyond region (C), the noise is predominantly white, indicating fundamental linewidth of the S1 emission[19]. These noise sources are summarized in Table 6.1.

6.4 Relative Intensity Noise Measurements

We measured the RIN of the first Stokes order of our Brillouin laser using a commercial OEwaves OE4000 RIN measurement system. The measured RIN for different S1 output powers is shown in Figure 6.6. RIN reduction is observed for increasing Stokes power followed by an increase in RIN once the second Stokes threshold is met. The RIN relaxation oscillation peaks are observed at a frequency offset of ~ 5MHz after which the RIN approaches its minimum value of ~ -150 dBc/Hz. The points (9-12) in the Figure 6.3(a) indicate the optical pump and first Stokes order powers at which the RIN measurements were taken. The RIN data was collected for each frequency decade from 10 Hz to 100 MHz. The number of averages Hz was set to 5 and 10 for the decades 10 Hz to 100 Hz and 100 Hz to 1 kHz respectively. For all the frequency decades above 1 kHz, the number of averages was set to 500.

The acquired and averaged frequency decade-wise RIN data, shown in Figure 6.6 shows a reduction in measured RIN (traces 9-11) till the pump power is below second Stokes threshold. The amplitude coupling between adjacent Stokes orders leads to RIN relaxation oscillations are observed at around 5 MHz, beyond which the measured RIN drops below the intensity noise of pump to -150 dBc/Hz at frequency offset close to 40 MHz, indicating the reduction of intensity noise due to Brillouin interaction. As expected[19], a sudden increase in RIN of first Stokes order is observed (trace 12) when the pump power is increased beyond

second Stokes order threshold due to additional noise contribution of anti-Stokes scattering from second Stokes order.

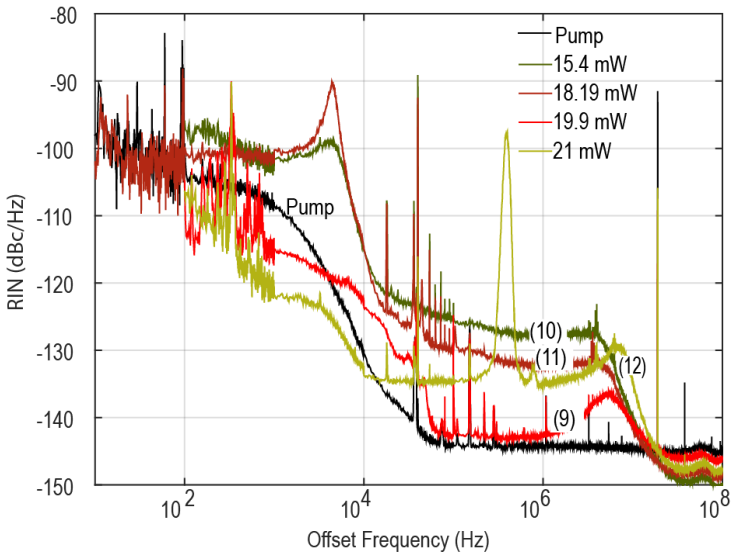

Figure 6.6. RIN Measurement of S1 of Si_3N_4 waveguide Brillouin Laser: *Measured relative intensity noise characteristics of first Stokes order of our Brillouin laser for different Stokes output powers. The marker numerals that associate the traces to the pump powers in Figure 6.3 are included*

6.5 Summary

The chapter presented the first observation and measurement results of sub-Hz (~0.72 Hz) fundamental linewidth emission in a monolithically integrated all-waveguide Brillouin laser. The theoretical aspects of fundamental noise dynamics in cascaded Brillouin lasers are described and the associated measurements of frequency and intensity noise of our Brillouin laser are presented. Absolute frequency noise measurements using UMZI based frequency discriminator were used to extract the fundamental linewidth of the laser and was found to be ~0.72 Hz when the pump power was close to the second Stokes threshold. The fractional frequency noise floor and integral linewidth associated with the sub-Hz fundamental linewidth emission have been evaluated to be 2.5e-15 $Hz^{-1/2}$ and ~3 kHz respectively. The RIN measurements performed using commercial measurement system showed relaxation

oscillations at around 5 MHz frequency offset and a minimum RIN of ~ -150 dBc/Hz at frequency offset close to 40 MHz. Realizing this high-performance laser in our foundry-compatible platform paves the way for a variety of applications including high spectral purity photonic RF oscillators and precision inertial sensing. These two applications will be discussed in the next two chapters.

Chapter 7: Photonic RF Oscillators

7.1 Abstract

In this chapter, the first application of our Brillouin laser, a low phase noise photonic RF oscillator is demonstrated. An overview of the need for photonic RF oscillators and the performance of the state-of the art discrete and integrated photonic microwave and mm-wave oscillators is presented. The theory associated with the beat note generation by photo-mixing the Stokes tones of cascaded order Brillouin laser is discussed and the relation between fundamental linewidth of beat note and that of participating Stokes orders is shown. The demonstrated results of Ku-band 21.8 GHz microwave generation by photo-mixing the first and third Stokes orders of our Brillouin laser with a measured phase noise of -84 dBc/Hz at 10 kHz are shown. The extraction of fundamental linewidth of first and third Stokes orders based on the beat note phase noise and the cascaded power dynamics yielding sub-Hz fundamental linewidth for first Stokes order is reported. Results of beat note frequency on the variations in pump power are included.

7.2 Application Overview

Photonic microwave frequency synthesizers (known as photonic RF oscillators) produce a microwave signal with phase noise comparable with the best electronic oscillators and exhibit frequency stability orders of magnitude better than electronic solutions[31]. For future applications like 5G networks, realization of high spectral purity photonic microwave and mm-wave oscillators in 5G access fronthaul is imperative[89] since the traditional electrical mm-wave generators become inefficient in both cost and performance at these frequencies. Discrete component optical frequency comb generators utilize temperature stabilized magnesium

fluoride (MgF_2) microresonators to achieve record low phase noise of -170 dBc/Hz at 10 MHz offset from the fixed 10 GHz RF carrier and -90 dBc/Hz close-to-carrier at 100 Hz offset[31]. RF carrier tunability can be achieved with more complex discrete component optoelectronic-optic (OEO) photonic oscillators that incorporate chip-scale Brillouin waveguides to achieve < -100 dBc/Hz at 100 kHz offset as the carrier is tuned from 5 GHz to 40 GHz[90]. Moving RF photonic oscillators to the chip-scale will lower power consumption, weight, volume, with a trade-off in tunability for today's approaches. The RF carrier frequency is fixed by the device physical dimension. However, optical frequency comb-based approaches can provide multiple RF carrier outputs. Discrete component microresonators utilizing Kerr comb generation produce microwave signals with measured phase noise as low as -115 dBc/Hz at 10 kHz frequency offset from a 35 GHz carrier[31]. Low frequency noise microwave generation using etched-silica microresonator Brillouin lasers in a dual cavity configuration with a stabilized high-Q microcavity and closed loop feedback control, measure close to -90 dBc/Hz at a frequency offset of 10 kHz from a 21.7 GHz carrier[91]. Creating truly tunable microwave photonic oscillator outputs today is accomplished with multiple photonic chip solutions and adaptation of state of the art dual-comb, self-referenced frequency comb based optical frequency synthesizers[92].

7.3 Theory of Phase Noise of Beat Notes Between Cascaded Stokes Orders

This section presents the mathematical framework of phase noise of beat note between Stokes tones of a cascaded Brillouin lasing system reported in Behunin et. al[19]. Only the equations pertinent to the analysis of measurement results are presented and the reader is encouraged to go through the reference for the complete mathematical and analytical treatment of the theory. Phase noise for the beat note between two Stokes orders m and m' is quantified using the

autocorrelation function $\langle \varphi_{Sm-Sm'}(t)\varphi_{Sm-Sm'}(t')\rangle$ where $\varphi_{Sm-Sm'}(t) = \varphi_{Sm}(t) - \varphi_{Sm'}(t)$ indicates the time-dependent phase fluctuations of the beat note. As mentioned in section 6.2.1, the phase noise dependence exists only between adjacent Stokes orders, and Stokes orders that are more than an order apart are uncorrelated in phase. This implies that for $m \neq m \pm 1$, $\langle \varphi_{Sm}(t)\varphi_{Sm'}(t')\rangle = 0$ simplifying the phase-autocorrelation $\langle \varphi_{Sm-Sm'}(t)\varphi_{Sm-Sm'}(t')\rangle$ to $\langle \varphi_{Sm}(t)\varphi_{Sm}(t')\rangle + \langle \varphi_{Sm'}(t)\varphi_{Sm'}(t')\rangle$. The PSD of phase noise is calculated through Fourier transform of $\langle \varphi_{Sm-Sm'}(t)\varphi_{Sm-Sm'}(t')\rangle$ (via the Wiener–Khinchin theorem as used in Eq. (1.1))

$$S_{\varphi(Sm-Sm')}(\omega) = \int dt\, e^{j\omega t} \langle \varphi_{Sm-Sm'}(t)\varphi_{Sm-Sm'}(t')\rangle \quad (7.1)$$

For $m \neq m \pm 1$,

$$S_{\varphi(Sm-Sm')}(\omega) = \int dt\, e^{j\omega t} \langle \varphi_{Sm}(t)\varphi_{Sm}(t')\rangle + \int dt\, e^{j\omega t} \langle \varphi_{Sm'}(t)\varphi_{Sm'}(t')\rangle$$

$$\Rightarrow S_{\varphi(Sm-Sm')}(\omega) = S_{\varphi Sm}(\omega) + S_{\varphi Sm'}(\omega) \quad (7.2)$$

Equation (7.2) implies that the fundamental linewidth of the beat note for $m \neq m \pm 1$, is the sum of fundamental linewidths of the participating Stokes orders yielding

$$\Delta\nu_{Sm-Sm'} = \Delta\nu_{Sm} + \Delta\nu_{Sm'} \quad (7.3)$$

As an example application of Eq (7.3), the fundamental linewidth $\Delta\nu_{S1-S3}$ can be expressed as the sum of the individual fundamental linewidths of the participating Stokes tones[19] as $\Delta\nu_{S1-S3} = \Delta\nu_{S1} + \Delta\nu_{S3}$. For third-order cascading, combining Eq. (7.3) with Eq. (6.1), the individual Stokes order linewidths can be directly related to the measured value of $\Delta\nu_{S1-S3}$ and

the relative optical powers of individual Stokes orders P_{S1} and P_{S3} through the following relations[19]

$$\Delta\nu_{S3} \approx \frac{\Delta\nu_{S1-S3}}{\left(1+\frac{^3P_{S3}}{P_{S1}}\right)} \text{ and } \Delta\nu_{S1} \approx \frac{\Delta\nu_{S1-S3}}{\left(1+\frac{P_{S1}}{^3P_{S3}}\right)} \quad (7.4)$$

Three important conclusions can be drawn from Equations (7.1-7.4). One, they allow realization of high spectral purity RF frequencies by photo-mixing of cascaded Stokes orders. Two, the spectral purity of the beat note (fundamental linewidth) can be engineered by a careful choice of the participating Stokes orders and the relative optical powers of the participating Stokes tones. Equation (7.4) suggests that the minimum beat note linewidth is not necessarily obtained by maximizing the optical powers of the participating Stokes orders. Three, if the beat note linewidth and relative optical powers of two Stokes orders with uncorrelated phases is measured, the fundamental linewidth of the individual participating Stokes orders can be evaluated.

7.4 Measurement Results

We demonstrate the lowest reported single-sided phase noise of -84 dBc/Hz at 10 kHz frequency offset (21.8 GHz carrier) for a monolithically integrated chip-scale Brillouin laser-based microwave synthesizer, within 6 dB of that achieved using a discrete fiber coupled silica wedge design[91]. Figure 7.1(a) shows the schematic of our microwave synthesizer (measurement setup is same as Figure 6.2). For an on-chip pump power of 125 mW, Brillouin lasing to three Stokes orders is observed as shown in Figure 7.1(b). The first and third Stokes orders are measured using a circulator at the resonator reflection port. We measure the phase noise power spectrum of the 21.8 GHz beat note using photo-mixed first and third order Stokes tones on a high-speed photodetector, amplified using a low noise RF amplifier, using a signal

source analyzer (Keysight Model E5052B), and a microwave downconverter (Keysight Model E5053A) for offset frequencies ν (100 Hz - 40 MHz). The measured single sideband RF beat note (21.8 GHz) phase noise and the evaluated frequency noise are shown in Figure 7.1 (c,d). The S1-S3 beat note noise leverage cancellation of common mode noise sources in the laser resonator (e.g. resonator optomechanical noise) during the photo-mixing process.

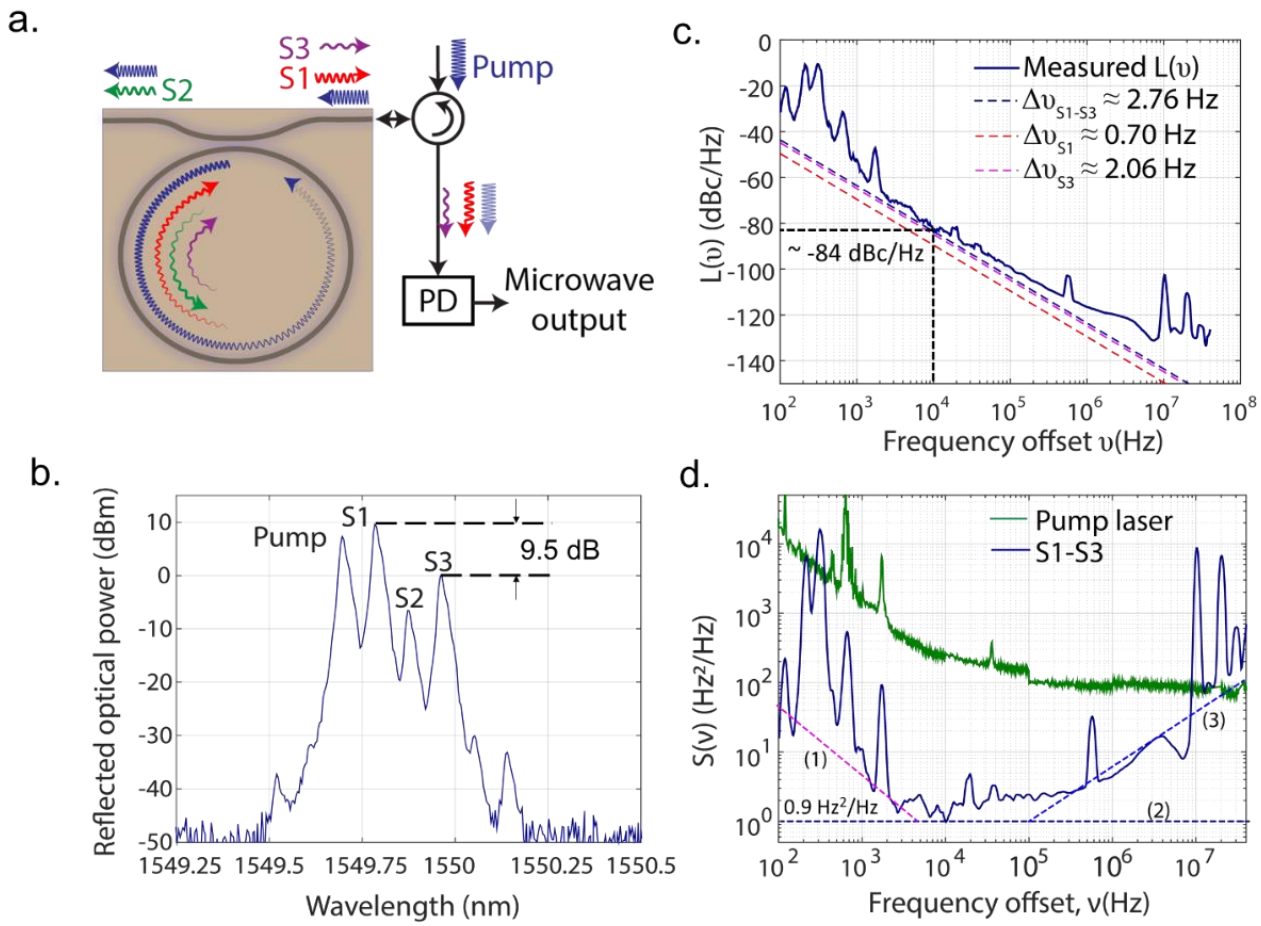

Figure 7.1.Brillouin Laser Based Photonic Microwave Synthesizer*: (a) Photonic microwave synthesizer configured by photo-mixing first and third Stokes orders. (b) Cascaded power spectrum up to third Stokes order showing that the first Stokes order exceeds the third by about 9.5 dB(c) Measured single sideband phase noise of beat note between first and third Stokes orders and corresponding theoretical fit lines to indicate the fundamental linewidth of first order Stokes emission. (d) Comparison of pump frequency noise with S1-S3 beat note frequency noise; Dotted lines (1), (2), (3) show the fits to flicker frequency noise, white frequency noise, and flicker phase noise regions*

7.4.1 Fundamental Linewidth of Beat Note and Individual Stokes Orders

Applying Eq. (7.4), the S1 fundamental linewidth can be extracted using the measured single sideband phase noise of S1-S3 beat note (dark blue line in Figure 7.1(c)) and the ratio of their respective optical powers P_{S1}/P_{S3} = 9.5 dB (see Figure 7.1(b)). The 2.76 Hz upper bound on the fundamental beat note linewidth $\Delta\nu_{S1-S3}$ at the minimum point in the frequency noise power spectrum as shown in Figure 7.1(d) is justified when assuming that the technical and fundamental sources of noise add in quadrature. Consequently, if technical sources of noise are eliminated, the fundamental beat note noise can be no larger than the sum of the fundamental noises of individual Stokes orders. By using this relation that only requires the relative Stokes powers rather than absolute powers, this analysis removes uncertainties in off-chip coupling losses, facet back reflections, and difference between hot- and cold-cavity parameters. In cascaded-order operation it is important to note that the theoretically predicted phonon-limited linewidth[19] of the first Stokes order at pump power close to the threshold of third Stokes order is nearly three times that of the S1 linewidth at the S2 threshold due to phonon noise contribution from the second Stokes order. This suggests that the minimum achievable fundamental linewidth of our Brillouin laser is ~0.3 Hz which was not measurable using the absolute frequency noise measurement setup due to the detector noise limitations detailed in section 6.3.1.

In Figure 7.1(d), we compare the frequency noise of the pump and the microwave beat note, indicating a relative suppression of pump frequency noise. Our measurements reveal regions dominated by frequency flicker (1/f) (region-1), phase flicker (f^1) (region-3), and white frequency noise (region-2 spanning 1-100 kHz), and the common noise peaks at 0.6 kHz, 1.7 kHz, and 3.9 kHz indicate residual transfer of pump phase noise to Brillouin laser. We attribute

the features of region-2 to fundamental noise, yielding fundamental frequency noise floor of ~ 0.9 Hz^2/Hz, indicating at least two orders of improvement from the pump laser frequency noise of ~ 200 Hz^2/Hz.

7.4.2 Power Dependence of Beat Note Frequency

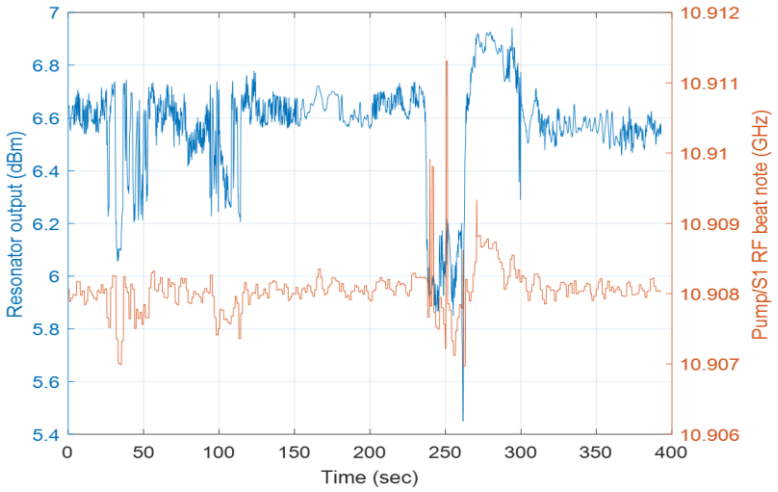

Figure 7.2. Power Dependence of Beat Note Frequency*: The beat note frequency between pump and first Stokes order at 10.9 GHz was found to change by about 3 MHz for a change of 0.6 dB in the power coupled in to the input bus of resonator.*

The high frequency deviations of the beat note at low frequency offsets, shown in Figure 7.1(d) indicated as region 1, are partly attributed to the variations of input pump power that couples in to the cavity. The characterization of beat note frequency dependence on input pump power variations was performed by manually changing the coupled power in to the waveguide bus of the resonator and simultaneously measuring both the resonator output power and the beat note frequency between pump and S1. The combination of material absorption and thermoelastic effect that changes the resonator dimensions (length or waveguide width) due to increase of temperature results in changes of the resulting beat note frequency. This indicates the sensitivity of spectral purity of the generated RF signal from cascaded Brillouin lasers on the intra-cavity power variations and calls for improved feedback mechanisms to counter the slow

intra-cavity thermal variations using on-chip actuators and suppression of intensity variations of pump using RIN servos.

7.5 Summary

This chapter described the demonstration of 21.8 GHz photonic RF oscillator with phase noise as low as -84 dBc/Hz at 10 kHz offset corresponding to a white frequency noise of 0.9 Hz^2/Hz by photo-mixing the first and third Stokes orders of a cascaded silicon nitride waveguide Brillouin laser. Combining the measured phase noise of the beat note with relative optical powers of the Stokes orders, the fundamental linewidth of the individual Stokes orders S1, S3 are extracted using cascaded Brillouin laser noise theory[19] to be 0.7 Hz and 2.76 Hz respectively indicating sub-Hz fundamental linewidth emission of S1. The pump power dependence of beat note frequency is described as one of the factors that degrade the spectral purity of generated beat note. The demonstrated high spectral purity photonic RF oscillator can be tuned by changing the pump wavelength and can provide a cost and power efficient way of microwave and mm-wave generation in applications like 5G networks, metrology, and coherent communications.

Chapter 8: Integrated Optical Gyroscopes

8.1 Abstract

This chapter reviews the operating principle of optical gyroscopes (Sagnac effect) and presents ULL Si_3N_4/SiO_2 waveguide platform to be ideally suited for realizing both interferometric optical gyroscope and Brillouin laser-based gyroscopes. As a second application of our Brillouin laser, the achievable performance of the Brillouin gyroscope using our laser is estimated based on the results of beat note phase noise obtained in section 7.4.1 and compared to the sensitivity achieved by the interferometric optical gyroscopes. The demonstrated results of a 3 m waveguide coil based interferometric optical gyroscope are included and the prospects for full-integration are discussed.

8.2 Application Overview

Sensors used in the fields of guidance and navigation have been undergoing continuous development for more than six decades[93]. Advancements in gyroscope technologies have been instrumental in the realization of high precision inertial motion units (IMUs) and inertial navigation systems (INSs). While the accuracy and performance are important, many applications in navigation today require reduced size, cost, and operating power of the inertial sensor in addition to their accuracy[94]. Smaller sensors enable and impart guidance, navigation, and control into miniaturized, smart, self-guiding systems such as drones which were previously considered unrealizable. Based on their quality and performance, gyroscopes are categorized in to different grades as listed in Table 8.1. Microelectromechanical (MEMS) gyroscopes, ring laser gyroscopes (RLGs), and interferometric fiber optic gyroscopes (IFOGs) are among the commercially mature and available technologies today that are widely used in navigation, tactical, and industrial applications.

Given the sensitivity of optical counterparts far surpasses the MEMS gyroscopes, miniaturization of both IFOGs and RLGs has garnered interest in the past decade[10,95]. While optical gyroscopes have traditionally been expensive, their decreased vibrational sensitivity and rate random walk makes them superior to their MEMS counterparts. Accordingly, MEMS sensors are widely used in commercial and rate grade sensor applications requiring lower sensitivity at reduced cost and RLGs are employed as tactical and navigation grade sensors in IMUs[96].

Traditionally, IFOGs have out-performed RLGs to achieve best-in-class performance and have proved to be the ideal choice for ultra-precision navigation and guiding applications and consequently research efforts to realize waveguide coils for chip-scale interferometric gyroscopes has been of interest. However, Brillouin laser-based gyroscopes[97–99] overcome the disadvantages of RLGs to achieve performance comparable to IFOGs by providing direct frequency read-out, higher immunity for lock-in errors and are better suited for integration.

Table 8.1: Classification of Optical Gyroscopes

Type	**Angle random walk (deg/√hr)**	**Bias instability (deg/hr)**
Rate grade (IOG reported in this chapter)	> 0.5	10 to 1000
Tactical grade	0.5 to 0.05	1 to 10
Intermediate grade	0.05 to 0.005	0.01 to 1
Inertial grade	< 0.005	< 0.01
Strategic grade	< 0.0003	< 0.001

8.3 Brillouin Laser Gyroscopes

The schematic of a Brillouin laser that employs our silicon nitride waveguide Brillouin laser is shown in Figure 8.1(a). The laser is pumped to emit two Stokes orders. While the gyroscope is at rest under earth background rotation, the frequency spacing between adjacent optical tones is very close to $f_B = \Delta\nu_B$. As the gyroscope rotation rate Ω is increased, the Sagnac induced frequency shift results in a relative increase in frequency difference between the counter-propagating first and second order Stokes tones[10], denoted as $\delta\nu$ in Figure 8.1(b). The rotation sensitivity of Brillouin laser gyroscope depends on the frequency noise of the beat note generated between the photo-mixed Stokes tones. The PSD of the rotation output $S_{\delta\Omega}$ is related to the beat notes as

$$\sqrt{S_{\delta\Omega}} = \frac{n\lambda}{D}\sqrt{S_{\delta\nu}} \qquad (8.1)$$

where n and D are the refractive index and diameter of the resonator, λ is the wavelength of laser in vacuum, and $S_{\delta\nu}$ is the PSD of frequency noise of the beat note between counter propagating lasers. For λ = 1.55 μm, n = 1.478, D = 23.6 mm and an $S_{\delta\nu}$ of 0.9 Hz^2/Hz (see Figure 7.1(d)), the achievable rotation sensitivity will be ~19 deg/hr/√Hz. On the other hand, RLGs that offer benefits of compactness with a comparable level of sensitivity are plagued by bias errors due to mode-locking of counter-propagating beams creating a dead zone at low rotation rate. RLGs employing Brillouin scattering called “Brillouin laser gyroscopes” overcome this issue by eliminating the need for gain medium inside the cavity and providing a direct frequency read-out. Brillouin laser gyroscopes are estimated to offer better sensitivity compared to interferometric counterparts in a relatively much smaller foot print.

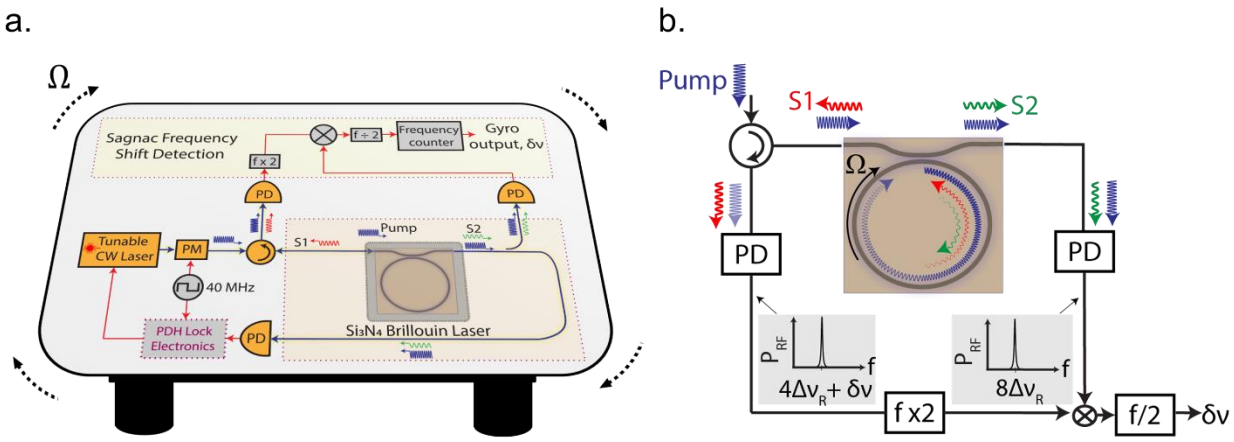

Figure 8.1. Brillouin Laser Gyroscope *(a) Brillouin laser optical gyroscope configured on a rotational stage operated at a rate Ω deg/sec. (b) Illustration of Sagnac frequency shift (δν) in the Stokes orders circulating in the resonator (pump-blue; first Stokes-red; second Stokes-green). The sign of δν depends on the direction of applied rotation and the value of δν is used to determine the rotation rate. The beat note between reflected pump and first Stokes order is frequency doubled and mixed with the beat note between pump and second Stokes order to extract the Sagnac frequency shift.*

8.4 Interferometric Optical Gyroscopes

Based on the design and performance, IFOGs can range from low cost, smaller area industrial rate grade sensors to expensive large area strategic or precision grade devices to be used in IMU/INS systems[100]. This versatility has attracted considerable research in the size reduction of interferometric optical gyroscopes (IOGs) while maintaining their high sensitivity and performance specifications. However, the cost and complexity of assembling high quality fiber optic gyroscopes requiring precision alignment and assembly of discrete optical components, and sensitivity to manufacturing and environmental variations has led to an increased need to integrate them at the chip-scale.

The performance of an IOG improves with increased enclosed area and is degraded by the limited polarization extinction of the optical coils. Chip scale integration can improve the manufacturability of IOGs in general, while at the same time addressing polarization misalignment issues and significantly reducing the size, weight, and cost. It has been

challenging to realize an on-chip waveguide coil based IOG with desired performance due to the absence of an integration platform that realizes very low waveguide loss over the required large on-chip coil lengths, a high degree of polarization selectivity and integration with other key elements like fiber to waveguide mode transformers and low loss waveguide crossings. The Si_3N_4 based ultra-low loss waveguide (ULLW) platform [101,102] provides a wafer-scale compatible solution to enable long, on-chip waveguide coils with losses as low as 0.1 dB/m[101]. In addition to the low waveguide loss and high polarization dependent loss (> 75 dB) of ULLW Si_3N_4 coils[103], the low nonlinear loss and high nonlinearity thresholds (compared to other waveguide platforms)[104], play an important role in minimizing parasitic effects due to the optical Kerr effect, and non-reciprocal polarization drift normally associated with using bulk optical components, thus resulting in improved gyroscope performance. A chip scale IOG can be achieved by three dimensional close-packed multi-chip integration of waveguide coil and integrated front-end chips. A fully integrated IOG can be realized by integrating the gyroscope front-end and low loss waveguide coil onto a single chip thereby exploiting the passive and active function of integrated front ends with the low loss of Si_3N_4 coils. The Si_3N_4 waveguide coil based gyroscope with active optical components on a heterogeneously integrated III/V-Silicon platform has been proposed and analyzed in [105]. Detailed design and characterization of integrated optical components for a IOG are presented in [106].

The rest of this chapter presents the design and characterization of low loss integrated waveguide coil-based interferometric optical gyroscope. We also discuss two approaches to integrate the optical active components with waveguide coil to realize an on-chip gyroscope sensor. We begin with the general setup for an IFOG followed by the description of design, fabrication, and packaging of waveguide coil. The rotation rate measurements, noise

characterization of gyroscope and the prospects for full integration and improvements in gyroscope performance using a longer coil with lower packaging losses are discussed.

8.5 Overview of Interferometric Optical Gyroscope

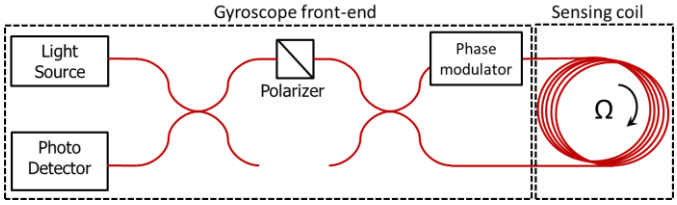

Figure 8.2. Minimum reciprocal configuration of an IFOG *(polarizer being an optional component). Physical dimensions and type of the sensing coil is varied based on the targeted application of sensor.*

The interferometric optical gyro operates on the principle of Sagnac phase shift [100]. The Sagnac phase shift $\Delta\varphi_R$ induced due to rotation in an IOG about the axis with rate Ω, as illustrated in Figure 8.2, is given by

$$\Delta\Phi_R = \left(\frac{8\pi}{c\cdot\lambda}\right)\cdot A_{enc}\cdot\Omega \qquad (8.2)$$

$$A_{enc} = N\cdot A \qquad (8.3)$$

where A_{enc} is the area enclosed in the sensing coil, λ is the mean wavelength of the optical source, and Ω is the rotation rate. For an IFOG, area enclosed is the sum of areas of each turn of the fiber sensing coil as shown in Eq. (8.3), where N is the number of turns and A is area enclosed by an individual turn of the coil.

The performance for a given enclosed area of sensing coil of an IOG is limited by the propagation loss and intrinsic noise sources that affect the performance including detected thermal noise and shot noise, laser relative intensity noise and un-desired interferometric effects that interfere with the desired detected signal, such as coherent backscattering and reflections, the optical Kerr effect, and polarization non-reciprocities [105]. The phase shift

induced by these non-reciprocities degrades the angle random walk and bias instability of the IOG. To address non-reciprocal polarization effects, polarization maintaining (PM) fiber and components can be employed, however the net polarization bias error is limited by the polarization extinction ratio (PER) of the sensing coil, the intensity rejection ratio of the polarizer and manufacturing and environment polarization misalignment and induced polarization coupling.

The RMS value of polarization bias error $\sigma_{\Delta\varphi e}$ induced by a sensing coil of length, L, mean rate of power transfer between the polarization modes h (PER = h.L), depolarization length L_d, and intensity rejection ratio of polarizer ε^2 is given by [100]

$$\sigma_{\Delta\varphi e} = \frac{\varepsilon^2 hL}{\sqrt{N}} \qquad (8.4)$$

where $N = L/L_d$ is the number of depolarization lengths. While the typical ε^2 of a fiber polarizer is limited to around 25-30 dB, high aspect ratio 40-nm core Si_3N_4 waveguides have been shown to have PERs > 75 dB [103], indicating a suppression of the polarization bias error by more than 4 orders of magnitude.

8.6 Integrated Coil Design and Fabrication

The design goal for waveguide coil to be used in an IOG is to realize largest possible area of coil with lowest possible attenuation. This translates to choosing an optimal length for a given waveguide loss to meet the required area and hence, desired gyroscope sensitivity. Archimedian spirals as shown in Figure 8.3, are ideal geometry to achieve maximum enclosed area and length for a given chip footprint. For an Archimedian spiral defined by $\rho = a + b\theta$, where a is the minimum radius and $b = \frac{1}{2\pi}$ x turn radius difference, and N turns, the effective enclosed area is given by

$$A_{enc} = \iint \rho \, d\rho \, d\theta = \frac{1}{2}\int_0^{2N\pi} \rho^2 \, d\theta = N\pi[a^2 + \frac{b^2}{3}(2N\pi)^2 + 2N\pi ab] \quad (8.5)$$

The use of thinner waveguide cores improves propagation and crossing losses (assuming operating in the region where sidewall roughness is the dominant contribution to both these characteristics) but places a limitation on the minimum waveguide bend radius [101]. Here we choose a waveguide structure with 40-nm thick Si_3N_4 core, shown in Figure 8.3 to give us minimal possible loss values, which constrains our bend radius to 11 mm. The lithographic stepper system ASML PAS 5500 DUV used in our fabrication process has a maximum die size of 21x25 mm that limited the bend radius to 10 mm within a single field. To overcome the limitation of die size of our DUV stepper and to realize a large area coil, we used ultra-low loss stitching [107] of 4 different DUV fields which increased the achievable coil radius to 20 mm.

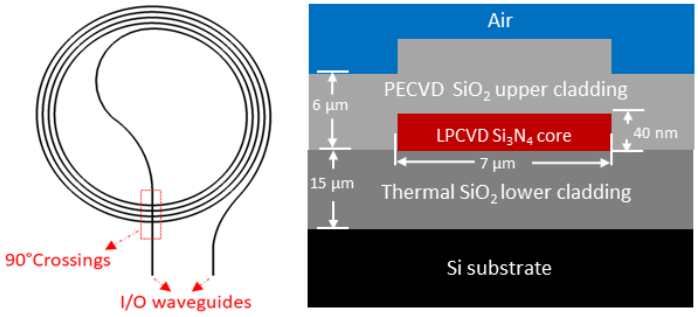

***Figure 8.3**. (left) Illustration of Archimedian waveguide spiral for an IOG. (right) Cross section of ULLW structure with 40-nm core to achieve lowest propagation loss*

Using Eq. (8.5) and the approach described in [105], the optimal length of the ULLW Si_3N_4 coil to be used in an integrated optical gyroscope to achieve ARW close to 1 deg/√hr was estimated as shown in Figure 8.4 to be about 3-10 m. The simulated value accounts for an excess packaging loss of 1 dB/m, RIN of -128 dBc/Hz and waveguide loss of 0.8 dB/m using

an optical input power of 100 mW. The estimated ARW of IOG with a 3-m integrated waveguide coil used in this paper, as shown in Figure 8.4, is close to 1.15 deg/√hr.

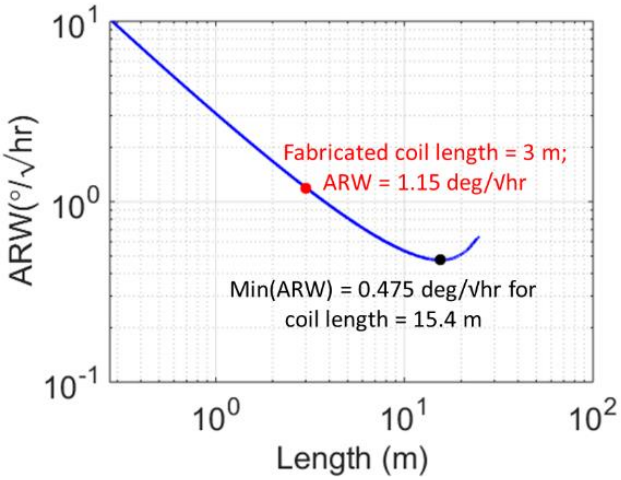

Figure 8.4. *Estimation of angle random walk for varying coil length*

The design parameters for fabricating the waveguide coil with 40 nm x 7 μm waveguide coil used in this paper are summarized in Table 8.2. Fabricated coil and crossing structures are shown in Figure 8.5.

Table 8.2: Summary of Waveguide Coil Design Parameters

Parameter	**Value**
Coil length	3 m
Outer radius	20 mm
Inner radius	17.25 mm
Waveguide spacing	50 μm
Number of crossings	50
Enclosed area	278 cm^2
Estimated ARW	1.15 deg/√hr

Waveguide loss of the coil was characterized using optical backscattering reflectometry (OBR). Different loss sources contributing to the total loss of the waveguide coil are listed in Table 8.3. Complete details about the large area waveguide coil design and characterization can be found in [107,108].

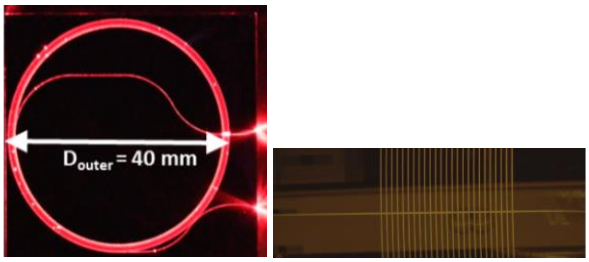

Figure 8.5*. (left) Top view of fabricated 3 m waveguide coil illuminated using a red laser (right) Dark field optical image of 90-degree crossings of the fabricated spiral*

Table 8.3: Summary of loss contributions in waveguide coil[108]

Parameter	Value
Waveguide and stitching loss*	0.78 dB/m
Crossing loss	0.0156 dB/crossing

** indicates the minimum waveguide and stitching loss measured at 1595 nm; At 1550 nm, waveguide loss is close to 1.5 dB/m. Estimated ARW for a waveguide loss of 1.5 dB/m, measured RIN of -122 dBc/Hz, and an excess packaging loss of 12 dB was around 2.23 deg/√hr.*

8.7 Coil Packaging

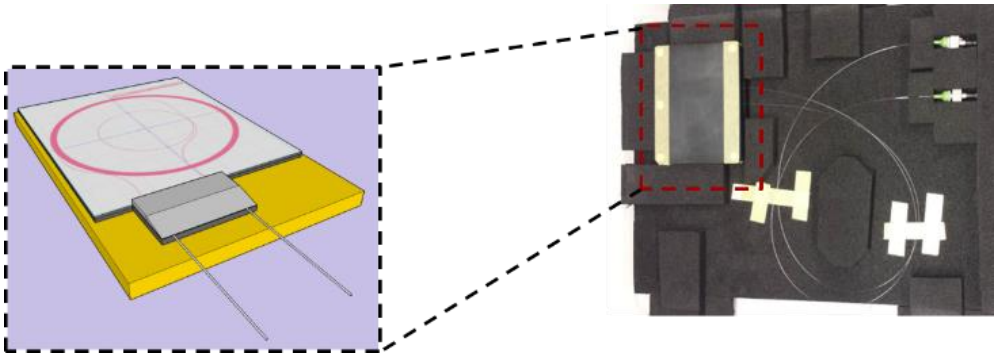

Figure 8.6. *(left) Illustration of the 3 m Si_3N_4 waveguide coil edge coupled to PM fibers using a VGA. (right) Actual packaged coil with FC/APC connectors (used to minimize reflections)*

To assess the performance of waveguide coil as the sensing element in a gyroscope, we packaged the coil and mounted it on a rotation stage for measurements. In order to reduce the polarization induced drift and to improve stability of device packaging, a custom-made V-groove array (VGA) was used to house polarization maintaining fibers which were edge coupled to Si_3N_4 waveguides as shown in Figure 8.6. Dymax epoxies OP-54 and OP-67-LS were used to put the VGA in place after alignment followed by a UV curing procedure using Dymax Bluewave 75 to bond the VGA to the plate. The mode mismatch between highly elliptical mode of our untapered waveguide and nearly circular mode of the fiber resulted in increase of fiber-chip coupling loss. In addition, the drift of the fibers post UV cure increased the coupling loss further, causing a total loss of > 6 dB per facet, resulting in a total insertion loss for the waveguide coil to be 16.2 dB with a broadband source for the packaged device.

8.8 Gyroscope Characterization and Performance Measurements

8.8.1 Proper Frequency

The rotation rate output of an IOG is evaluated using the amplitude of first harmonic of bias modulation frequency in the output of the reflected signal. To achieve perfect rejection of all the even harmonics, realize maximum sensitivity, and suppress other parasitic noise sources, the bias modulation should be at a frequency f_p, which is the inverse of twice the transit delay, $\Delta\tau_g$ of the sensing coil.

$$f_p = \frac{1}{2 \cdot \Delta\tau_g} \tag{8.6}$$

This frequency is known as the proper (eigen) frequency [100,109,110] of the coil where the gyroscope operates with maximum sensitivity. We utilized square wave biasing scheme to further suppress the spurious effects due to nonlinear response of modulator [100]. The gyroscope

characterization was performed using an in-house assembled setup is shown in Figure 8.7. Two 20 dB ZFL-1000LN RF amplifiers were cascaded between the photo detector and the lock-in amplifier to improve the signal to noise ratio. The time constant and filter slope for demodulation using lock-in were set to 300 ms and 24 dB/octave respectively.

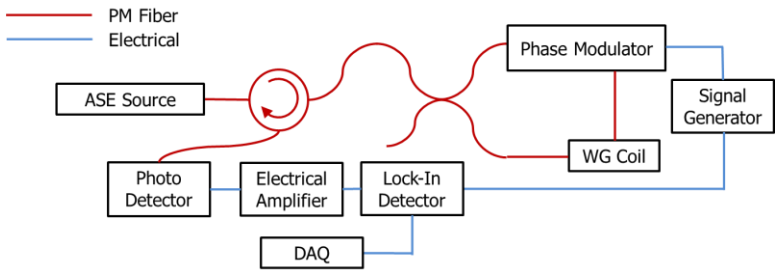

Figure 8.7. *Setup for characterization of gyroscope based on a waveguide (WG) coil. SRS 844 lock-in amplifier was used for demodulation and a National instruments (NI) data acquisition (DAQ) was used to collect the output data*

The proper frequency of our waveguide coil gyroscope, determined by performing a ramp frequency sweep (as described in our previous paper [109,110]), was found to be 21.02 MHz (shown in Figure 8.8.) The measured value agrees well with the expected value of proper frequency based on actual length of the sensing coil (3 m waveguide coil + fiber pig tails ~ 5 m).

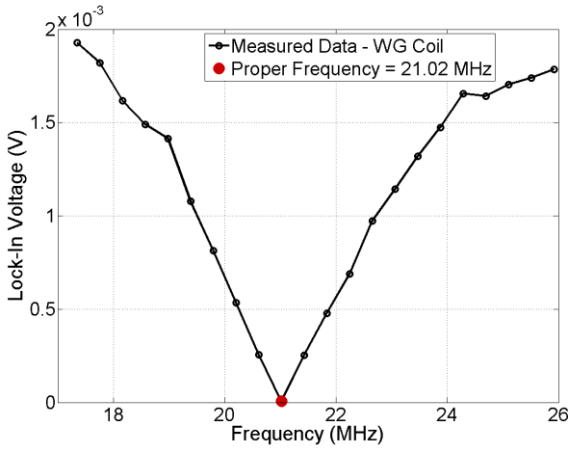

Figure 8.8. *Measured proper frequency of the sensing coil with 3-m Si_3N_4 waveguide in the loop and about 2 m PM fiber pig-tails*

8.8.2 Rotation Signal Measurement and Noise Characterization

To correlate the measured output value of gyroscope to the input rotation rate, we placed the setup on a calibrated rotation stage and measured the scale factor of the sensor. To accomplish this, we used a high precision rotation stage (Ideal Aerosmith 1270VS) and the applied rotation rate was swept from 0.02 deg/sec to 10 deg/sec in both CW and CCW directions. The scale factor was measured to be approximately 335 mV/deg/sec, as shown in Figure 8.9.

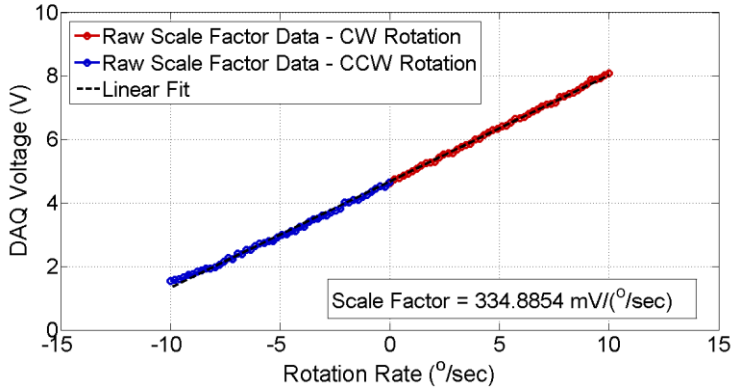

Figure 8.9. *Measured output was quite linear with the input rotation rate and the difference in scale factor between CW and CCW rotation rates was very small*

The detection limit of the gyroscope was characterized with the setup at rest using the standard Allan deviation technique [111]. The samples were captured using NI-DAQ at a rate of 50 Hz for an hour. The plot of Allan variance for one hour of data is shown in Figure 8.10. A -0.5-slope line was fit to the data to extract the angle random walk or the detection limit of the system to be 8.52 deg/√hr. The bias instability of the gyroscope is evaluated from the flat portion (slope = 0) of the Allan deviation plot. As seen in, there is a flat portion (A) at 0.03 hr which gives a BIS of 58.68 deg/hr and another flat portion (B) at around 0.1 hr, which yields a BIS of 45.42 deg/hr before noise becomes predominantly rate random walk (slope = 1).

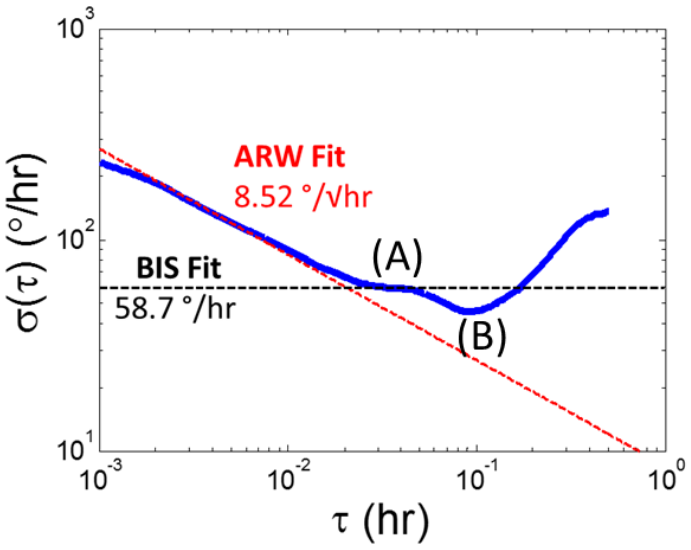

Figure 8.10. *Allan deviation measurement with lock-in time constant of 300 ms, with a filter slope of 24 dB/octave and sampling rate of 50 Hz*

To further verify the value of bias instability, we performed an Allan deviation measurement for five hours at a sample rate of 10 Hz and lock-in time constant of 3 s. The flat portion on this Allan deviation plot was observed at 0.034 hr as shown in Figure 8.11 yielding a BIS of 68.4 deg/hr which is closer to the 58.68 deg/hr measured in region (A) of Figure 8.10.

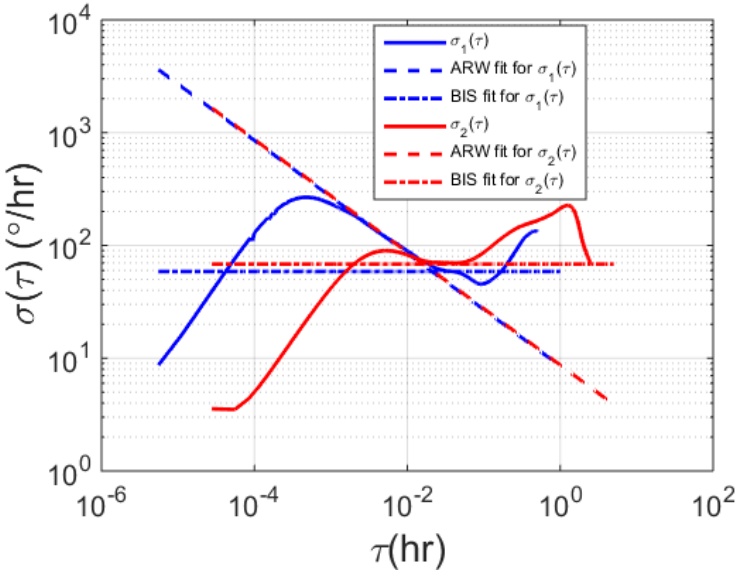

Figure 8.11. *$\sigma_1(\tau)$ and $\sigma_2(\tau)$ refer to the Allan deviation measurements with time constant of 300 ms and 3 s respectively; Allan deviation is valid only from τ = (1/ENBW) sec*

High value of bias instability suggests that 1/f flicker noise from electrical components to be the dominant noise source. Summary of all gyroscope measurements is given in Table 8.4.

Table 8.4: Summary of measurements

τ_{int} (ms)	ENBW (Hz)	SF (V/deg/sec)	ARW (deg/√hr)	BIS (deg/hr)	f_{sam} (Hz)
300	0.26	0.335	8.52	58.68	50
3	0.026	0.33	8.7	68.4	10

τ_{int} = Lock-in time constant; ENBW = Effective noise bandwidth for filter slope of 24 dB/oct; SF = scale factor; f_{sam} is the DAQ sampling rate; ENBW = (5/64τ_{int}) for a filter slope of 24 dB/oct;

8.9 Prospects for Full Integration and Packaging

Integration of active optical components along with the waveguide coil will help us realize a chip scale version of IOG. While broadband sources are the preferred optical sources for most of the commercial IFOGs because of their immunity to several noise sources of gyro such as coherent backscattering [100], use of a laser that is spectrally broadened with direct[112–115] or external[116,117] frequency/phase modulation has attracted considerable attention in the recent years. Because of their advantages such as smaller footprint, higher power efficiency, and higher wavelength stability (that translates to higher scale factor stability), a frequency modulated(FM) laser will be a more suitable candidate for a chip scale gyroscope. An integrated photonic chip with an optical source, two couplers, three photodiodes, and two phase modulators within an area of 4.5 mm^2 that can be used to realize a chip scale gyroscope was demonstrated by the authors, details of which can be found in [106].

Multi-chip photonic integration of the low loss waveguide coil and integrated front-end chip can be used to realize a chip scale IOG. The integrated front-end chip can be placed in a deep-

etch cavity on the waveguide coil chip, aligned and epoxied to realize a hybrid chip version of IOG as shown in Figure 8.12.

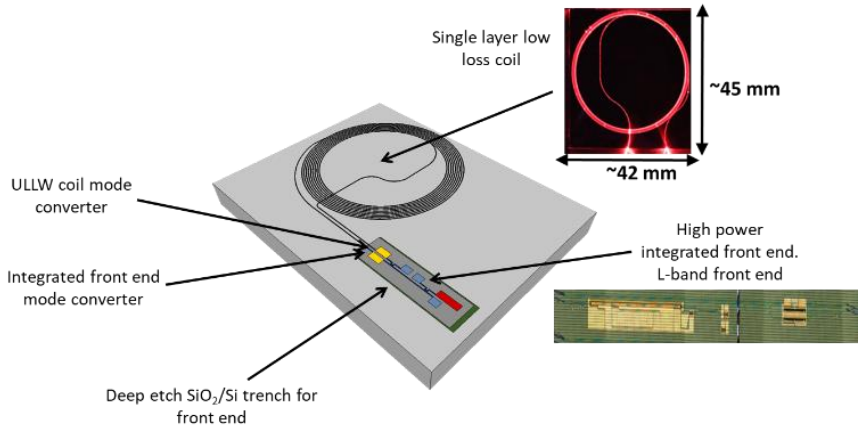

Figure 8.12. *Schematic of proposed fully multi-chip IOG with integrated front-end chip placed in a deep-etch SiO2/Si trench on the waveguide coil chip. Mode converters on both the chips help in realizing smaller coupling losses*

With customized tapers designed for both Si_3N_4 and Si waveguides as shown in Figure 8.13, the low loss waveguide coil can be coupled with the integrated front-end with minimal coupling losses.

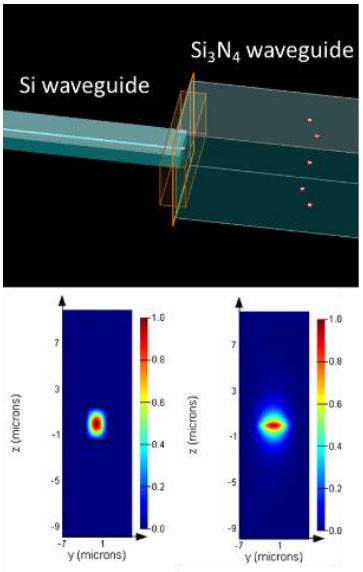

Si waveguide dimensions
200 nm x 269 nm

Si3N4 waveguide (WxH)	Power coupling (%)
7 um x 40 nm	64.88
2.8 um x 40 nm	61.73
2.8 um x 90 nm	92.3

Figure 8.13. *Example design of mode converters (using mode solutions in Lumerical[118]) between Si_3N_4 and Si waveguides showing the power coupling efficiency for different geometries of Si_3N_4 waveguide.*

A fully integrated waveguide coil-based gyroscope can be realized using vertical coupling between Si_3N_4 and Si waveguide layers. Such coupling can be used to integrate Si_3N_4 waveguide coil with the integrated front-end. Coupling losses of (0.4 ± 0.2) dB per transition between silicon and ULLW layers have been demonstrated in [119] that would provide a solution to alleviate the high fiber to waveguide coupling loss through seamless chip scale integration of all IOG components (III-V/Si actives with ULL Si_3N_4 coils) and realize a fully integrated waveguide coil based interferometric optical gyroscope as shown in Figure 8.14. The phase modulator is operated in push-pull configuration using two electrodes (yellow) to reduce driving voltage and jitter improving the power efficiency and performance of the sensor.

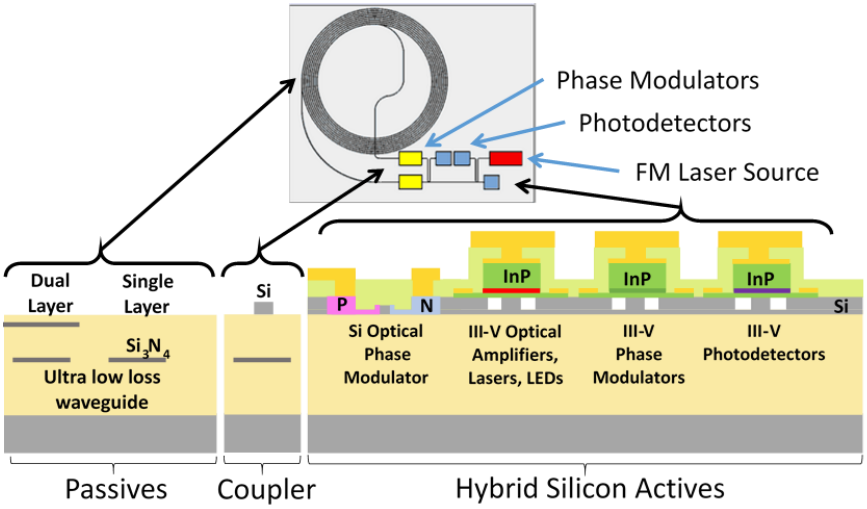

Figure 8.14. *Schematic of proposed fully integrated optical waveguide gyroscope with a ULLW coil in Si_3N_4 with heterogenous III/V-Si front-end*

8.10 Summary

This chapter presented an overview of integrated optical gyroscopes, compared two versions of optical gyroscopes: Brillouin laser gyroscope and interferometric optical gyroscope in terms of their achievable performance and scope for integration. The rotational sensitivity achievable by a Brillouin gyroscope using our laser has been estimated and the demonstrated results of 3

m waveguide coil based interferometric gyroscope have been reported. The measured gyroscope sensitivity of the waveguide coil IOG (ARW = 8.52 deg/√hr) was found to be in the same order as that of a commercial rate grade sensor. Reduction of flicker noise by using low noise electrical components and decrease in the total packaging loss to less than 1 dB (currently 12 dB) will greatly improve the performance of gyroscope and bridge the mismatch between values of measured and simulated sensitivity. We estimated that the ARW can be reduced to 0.52 deg/√hr for the current 3 m coil by decreasing the RIN of optical source from -128 dBc/Hz to -140 dBc/Hz. This suggests that use of a frequency/phase modulated laser source, because of its low RIN, can result in significantly better gyroscope performance. Simulations in [107,108] show that further improvements in waveguide losses and increase in the waveguide coil length (15 m) using a broadband source with 100 mW of optical power having a RIN of -128 dBc/Hz will push the sensitivity down to that of a tactical grade sensor (ARW = 0.475 deg/√hr). Reduction in waveguide propagation loss enables realization of larger area coils that can further improve the performance of the sensor. The demonstrated results show that ultra-low loss waveguide coils offer a promising solution to realize a fully integrated waveguide optical gyroscope (IWOG) as shown in Figure 8.14 that is resilient to several noise factors such as errors related to optical non-linearities and polarization drift. Also, the realization of an optical gyroscope using our Brillouin laser will achieve significantly better rotation sensitivity with some more improvements to reduce the flicker frequency noise components contributing to the beat note noise.

Chapter 9: Summary and Future Work

9.1 Abstract

This chapter summarizes the thesis and presents the directions for future work employing the high performance on-chip laser demonstrated here. Four example system-on-chip applications are studied and mechanisms for integral linewidth reduction are briefly discussed.

9.2 Thesis Summary

This thesis reported the first waveguide-integrated sub-Hz fundamental linewidth Brillouin laser. Comprised of an integrated ring-bus Si_3N_4 waveguide resonator, this laser combines low-optical losses, a large mode volume, and a broad Brillouin gain bandwidth to produce highly-coherent cascaded-order laser emission. The details of waveguide fabrication, theoretical and experimental results of Brillouin gain spectrum in silicon nitride waveguides are presented. The resonator designed and fabricated based on the experimental Brillouin gain spectrum results demonstrated the highest loaded Q ever reported for an all-waveguide microresonator with deposited cladding. Observation of Brillouin lasing with threshold as low as ~10 mW and laser cascading up to 10 Stokes orders, with a small amount of four-wave mixing has been reported. The cascaded laser power dynamics have been analyzed to show excellent agreement with theory. The long resonator length and single polarization operation made possible by this unique waveguide platform, as well as the relatively broad gain bandwidth, minimize the need for dispersion engineering and enable high intra-cavity intensities. Consequently, narrow-linewidth Brillouin lasing can be achieved over a broad range of pump wavelengths.

By performing absolute frequency noise measurements of the first Stokes order for pump powers varying from sub-threshold to second Stokes order threshold, we determined the

fundamental linewidth of the first Stokes order to be ~0.7 Hz for pump powers close to second Stokes order threshold. In addition, the beat note-electrical spectra and optical frequency noise measurements demonstrate evolution from spontaneous to stimulated emission and output linewidth narrowing as the pump optical power is increased.

We reported the results of a low phase noise Ku band photonic microwave oscillator utilizing our Brillouin laser. By photo-mixing the first and third Stokes tones of the cascaded Brillouin laser, a 21.8 GHz photonic RF oscillator with phase noise as low as -84 dBc/Hz at 10 kHz has been reported. Combining the beat note phase noise with the relative optical powers of the Stokes orders and the cascaded Brillouin laser theory[19], the fundamental linewidth of the first Stokes order has been predicted to be around 0.7 Hz.

The achievable performance of an integrated optical gyroscope based on our Brillouin laser has been reported and a comparative study of the Brillouin laser gyroscope and interferometric optical gyroscopes has been presented. The demonstrated results of a 3 m waveguide coil based interferometric optical gyroscope have been reported to show rate grade performance with sensitivity of 8.52 deg/√hr and bias drift of 58.6 deg/hr.

9.3 Potential Future Work

9.3.1 Integral Linewidth Reduction

Looking forward, several design strategies are available to further improve the linewidth and noise performance of this laser. The linewidth improvement techniques can be broadly classified in to passive optical methods or active optoelectronic approaches.

Passive Optical Approaches for Linewidth Engineering: The resonator design and the waveguide cross-section geometry can be engineered to either limit the number of cascading

Stokes orders or to broaden the Brillouin gain spectral width further. The fundamental linewidth of mth Stokes order is given by Eq. (6.1) as

$$\Delta\nu_m = \frac{1}{4\pi N_m}\left[\gamma_m\left(N_m^{th} + n_{m-1}^{th} + 1\right) + 2\mu' N_{m+1}\left(n_m^{th} + n_{m-1}^{th} + 1\right)\right] \quad (9.1)$$

To minimize $\Delta\nu_m$, a low γ_m (high Q) and a high N_m are required. The resonator Q can be engineered by altering the waveguide and resonator design[120] and implementing new processes to further lower waveguide loss. Increase of quality factor can be achieved through reduction in optical propagation loss by improvements in fabrication process to reduce the sidewall scattering loss using an optimized anneal or deposition recipes. The scattering losses may be further reduced by engineering the waveguide cross-section to have thinner cores and larger widths that prevents interaction of mode with side-wall and dilutes the mode in the vertical direction. To minimize the fundamental linewidth, the power coupling coefficient, achievable propagation loss, and emitted Stokes power can be optimized to maximize the output power of Stokes order while retaining a high resonator build up factor.

In addition to design and processing adjustments just described, the laser dynamics (maximizing N_m) can be further engineered by manipulating the frequency response of the resonator as well as the Brillouin gain. Example techniques to manipulate the frequency response are shown in Figure 9.1. A schematic of SBS laser resonator with 3 cascaded Stokes orders is shown in Figure 9.1(a). The number of cascaded orders supported by the laser resonator can be limited by ensuring frequency selective coupling of power into resonator modes. The illustration of the SBS laser resonator spectrum that support modes at pump and S1 while selectively suppressing the mode at S2 shown in Figure 9.1(b). Due to the absence of support for S2, the number of build-up of S1 power continues even when pump power is

increased beyond S2 threshold leading to a decrease of S1 fundamental linewidth. Two approaches to achieve frequency selective coupling of resonator modes, using an intra-cavity grating and a frequency-selective coupler are schematically illustrated in Figure 9.1(c, d).

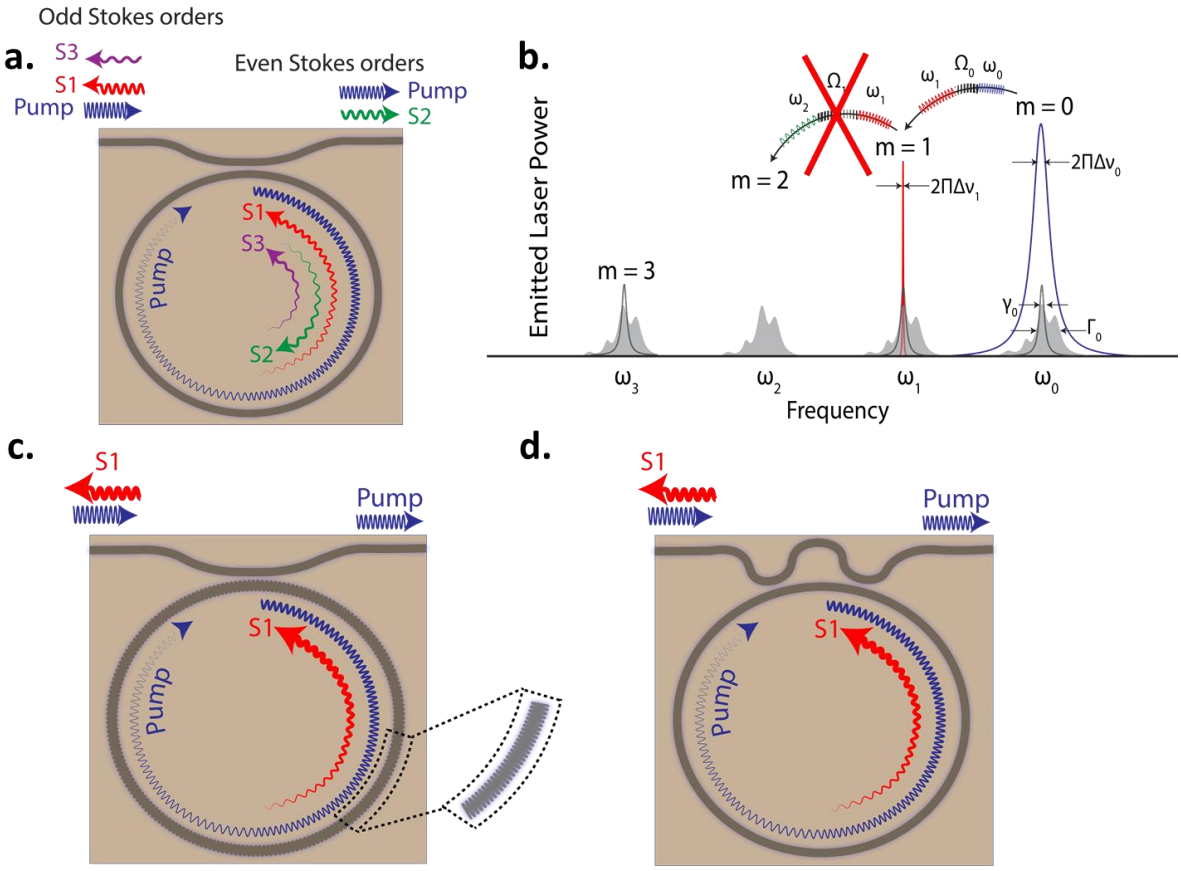

Figure 9.1. Linewidth improvement by limiting number of cascading Stokes orders: *(a) Schematic of Si_3N_4 SBS laser resonator showing cascading up to 3 Stokes orders (b) Spectral illustration of approach of engineering resonator spectral modes to limit the transfer of Stokes power. Absence of a mode supported by the resonator at frequency of 2nd Stokes order will limit the number of cascaded Stokes orders to one. (c,d) Example configurations to engineer resonator modes at Stokes frequencies by using (c)grating inside the resonator or (d) frequency-sensitive ring-bus coupler*

In addition, further broadening of Brillouin gain bandwidth[121] can enhance the linewidth performance through engineering of waveguide-cross section geometry. Decreasing the waveguide core thickness dilutes the optical mode, as shown in Figure 9.2, leading to a reduction of effective Brillouin gain coefficient and broadening of Brillouin gain bandwidth. The larger mode volume will support a larger volume of photons and shorter phonon lifetime,

leading to improved suppression of transfer of phase noise from pump to Stokes. The increase in optical mode area will also lead to an improvement in the flicker noise performance of the system by reducing the impact of intra-cavity thermo-refractive fluctuations on integral linewidth.

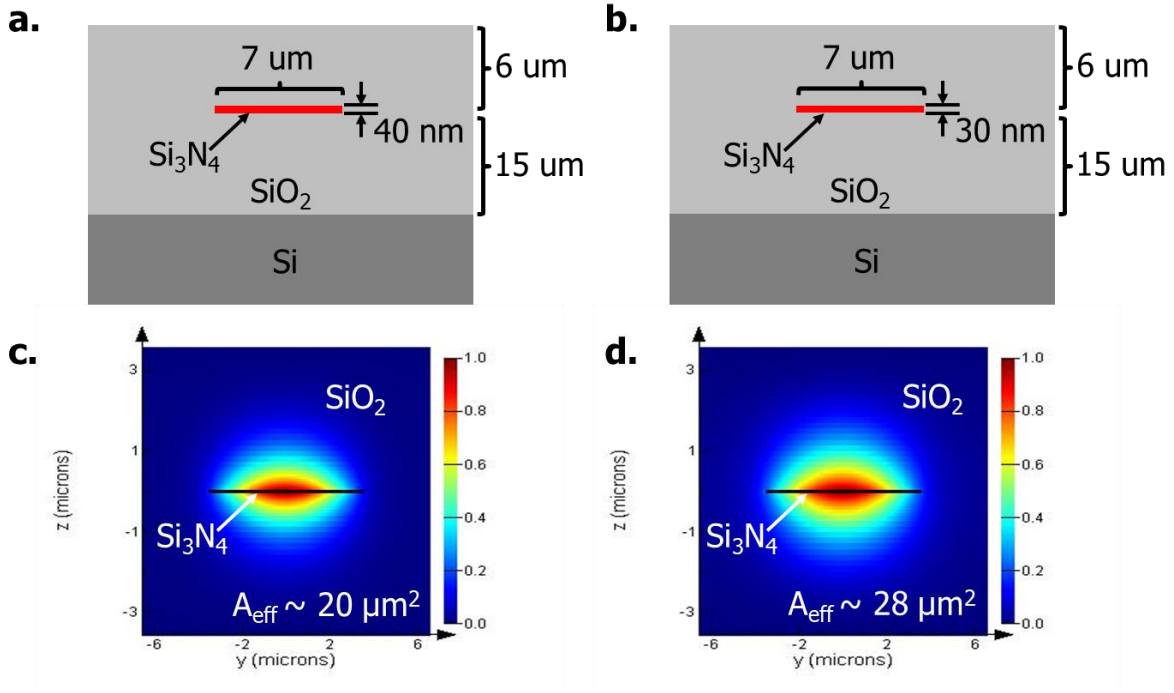

Figure 9.2. Linewidth improvement by increase of optical mode area by varying waveguide geometry: *Cross-section and simulated fundamental optical modes of (a,c) 40 nm thick x 7 um wide waveguide and (b,d) 30 nm thick x 7 um wide waveguide, showing nearly a 40 % increase in effective optical mode area for a 10 nm decrease in core thickness. Thinner cores result in a higher optical mode area leading to a decreased peak Brillouin gain and a larger Brillouin gain bandwidth, thereby improving the linewidth performance of the SBS laser.*

Depending on the application requirements, it might also be important to realize a trade-off between the Brillouin laser threshold, slope efficiency, and fundamental linewidth or phase noise. For a given optical propagation loss, increase of Brillouin gain through improved acoustic confinement can also be utilized for power-efficient Brillouin lasing. Two approaches to improve the acoustic confinement[122,123] of the waveguide cross-section are shown in Figure 9.3. While these approaches are more vulnerable to pump phase noise transfer from pump,

decreased Stokes threshold can improve the power efficiency of the laser system to realize low-power cascaded Brillouin laser frequency combs.

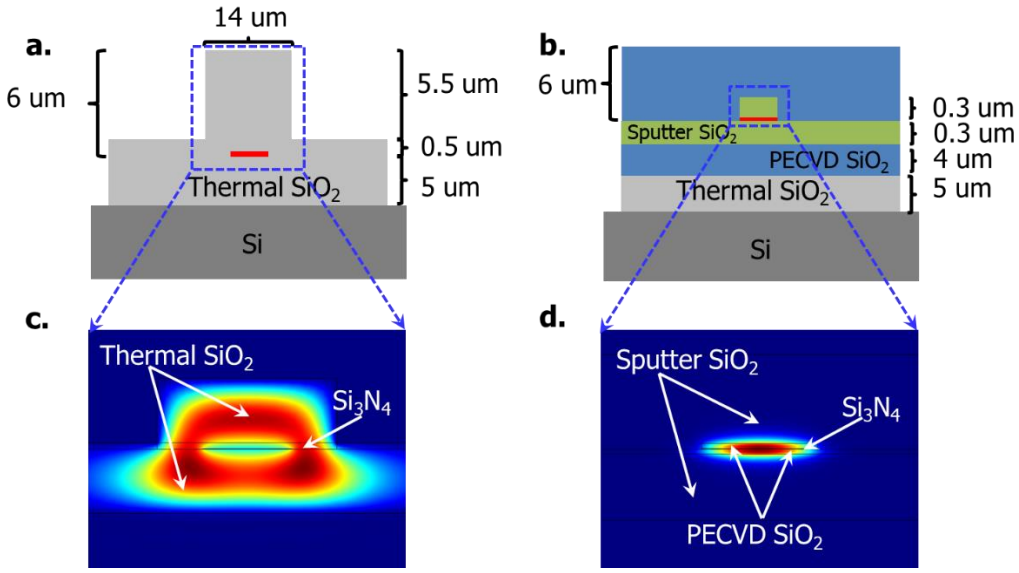

Figure 9.3. Techniques to improve acoustic confinement for low-power Brillouin lasers: *(a,c) Cross-section and simulated fundamental acoustic modes of rib waveguide structure (b,d) Cross-section and simulated fundamental acoustic modes of waveguide structure using two different oxide claddings to confine the acoustic mode.*

By adopting these strategies, we foresee that resonators with loaded Qs more than several hundred million and engineered Brillouin emission will enable unprecedented high coherence integrated lasers and will be transformative for many applications including coherent communications, photonic microwave oscillators, positional and navigation sensors and atomic clocks.

Active Optoelectronic Feedback Control for Integral Linewidth Narrowing: Lowering the integral linewidth of the current resonator from the current value of ~3 kHz requires addressing the high frequency deviations at lower frequency offsets. The high frequency deviations of the S1 at frequency offsets < 1 kHz are primarily attributed to the thermo-refractive and thermo-elastic noise contributions from the resonator[85].

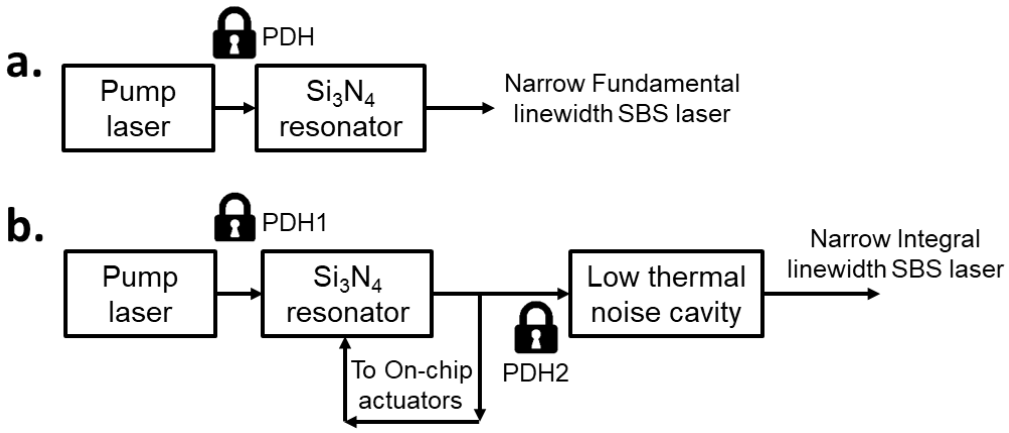

Figure 9.4. Opto-electronic feedback control techniques for integral linewidth narrowing: *(a) Block diagram of pump laser locked to Si_3N_4 SBS resonator resulting in narrow fundamental linewidth laser emission. (b) Dual cavity SBS laser with active feedback control using on-chip actuator elements and thermal noise reduction through locking to a low thermal noise external cavity.*

While the large optical mode area of our resonator (28 μm^2) aids in increasing the thermal response time of our resonator, locking to an external cavity such as a silica micro-rod or ULE FP cavity can further reduce in low frequency noise components can effectively suppress the flicker noise components resulting in large frequency deviations. Lowering these contributions can be done using active feedback mechanisms based on on-chip thermal or stress actuators to compensate for the slow changes in the refractive index or resonator length variations.

In addition to these sources there are technical noise sources introduced by the PDH locker and other electronics, cavity optomechanical noise, pump amplitude to Brillouin phase noise conversion, stimulated Brillouin induced RIN, and other Gaussian noise sources that contribute to the integral linewidth as well as low frequency sources that lead to long term drift. These low frequency noise components, below several hundred kHz, can be lowered to the quantum floor using external coupled micro-cavity reference techniques[34], and by integrating low, mid and high frequency thermal and stress actuators[38] in the resonator cavity

itself, as illustrated in Figure 1.3(a). The demonstrated ability to integrate control actuators in this waveguide platform is key in achieving performance normally associated with benchtop Brillouin lasers that employ intra-cavity feedback and control.

The foundry-compatible platform and fabrication of this laser make it possible to create high-performance light sources with reduced size, cost, and power consumption. This compatibility allows this chip-scale laser to be combined with a wide variety of Si_3N_4 and silicon photonic waveguide based integrated active and passive components, enabling a range of future high-coherence applications on chip. Moreover, the large transparency window, from 405 nm - 2350 nm, of the Si_3N_4 platform paves way for narrow linewidth, wafer-scalable Brillouin lasers operable over a broad range of wavebands.

Low phase noise SBS lasers using high phase noise pumps: The Si_3N_4 platform leads the way to low cost, tunable highly coherent Brillouin lasers pumped by on-chip, low coherence, heterogeneous III-V/silicon[50] and Hybrid III-V/Si_3N_4[23] lasers. Brillouin laser linewidths are limited by spontaneous scattering unlike traditional semiconductor lasers whose linewidth is limited by spontaneous emission. As discussed in section 6.2.1, the linewidth contribution due to transfer of phase noise from pump to Stokes tone, $\Delta\nu_{S1}^{tr}$ can be estimated using work of Debut et. al[18] as

$$\Delta\nu_{S1}^{tr} = \frac{\Delta\nu_{Pump}}{K^2} \qquad (9.2)$$

$$K = \left(1 + \frac{\gamma_A}{\Gamma_c}\right) \qquad (9.3)$$

where $\Delta\nu_{Pump}$ is the pump linewidth, $\Delta\nu_{S1}^{tr}$ is the linewidth of first Stokes order due to transfer of phase noise from pump, γ_A is acoustic damping rate, K is the pump linewidth reduction factor, Γ_c is the optical cavity decay rate, and $\Delta\nu_B$ is the Brillouin gain bandwidth.

Using $\Delta\nu_B$ = 153 MHz, Γ_c = 2π x 6.79 x 10^6 /sec, the linewidth of a commercial DFB laser (assuming $\Delta\nu_{Pump}$~ 10 kHz) can be reduced by a factor of K^2~554 to ~18 Hz. The linewidth contribution from pump phase diffusion $\Delta\nu_{S1}^{tr}$ increases for pump lasers with larger phase noise and must be taken in to account when $\frac{\Delta\nu_{S1}^{tr}}{\Delta\nu_m} \approx 1$, where $\Delta\nu_m$ is the fundamental linewidth predominantly determined by the thermal quanta of phonons. Reduction of resonator propagation losses will significantly decrease this contribution. For a low loss laser resonator with Γ_c = 2π x 1 x 10^6 /sec, the suppression factor can be as high as 23700, resulting in $\Delta\nu_{S1}^{tr}$ of ~0.42 Hz.

The properties of our Brillouin laser make it an ideal source to act as a pump for microresonator based Kerr frequency combs, as the comb frequency noise is limited by pump laser noise. Si_3N_4 frequency combs pumped with this Brillouin laser will lead to improved multi-channel WDM compact sources for coherent terabit communications. The spectral purity of this sub-Hz fundamental linewidth laser can be used to generate low phase noise microwave signals directly from multiple Stokes orders or by driving a comb generator. Operation in the visible and near-IR spectrum with narrow linewidth promises compact coherent sources for spectroscopy and atomic clocks. This integration platform is directly compatible with previously demonstrated chip-scale photonic components leading to higher complexity circuits with sub-Hz lasers, and wafer-scale foundry CMOS compatible processes, opening the door to a wide range of applications.

Initial results of photonic RF oscillator, like the one shown in Figure 1.3(e) have already been reported earlier in this thesis. Integration of on-chip laser, detector, feedback control mechanisms, and optical filters can enable true system-on-chip versions of these applications. The waveguide platform Additionally, this sub-Hz fundamental linewidth laser

serves as an ideal integrated pump for WDM frequency comb generators[21]. These features, coupled with the low loss of Si_3N_4 waveguides[42] across the 405 nm – 2350 nm wavelength range[36], provide a well-defined path to systems-on-chip integration for a wide range of future applications.

9.4 Conclusion

In conclusion, this thesis described the theory, design, fabrication process, measurement and characterization, and applications of first monolithically integrated silicon nitride waveguide Brillouin laser. The demonstrated work and results combined with the versatility and advantages of this platform can surely open doors to exciting possibilities of photonic devices and applications in the areas of coherent communications, sensing, metrology, spectroscopy, and quantum information.